UNIVERSITÉ GRENOBLE ALPES

THÈSE

Pour obtenir le grade de

DOCTEUR DE L'UNIVERSITÉ GRENOBLE ALPES

Spécialité : **Physique/Physique Théorique**

Arrêté ministériel : 7 août 2006

Présentée par

Samuel Hanot

Thèse dirigée par **Sandrine Lyonnard** et
codirigée par **Stefano Mossa** et **Timothy Ziman**

préparée au sein du **Groupe théorie de L'Institut Laue-Langevin**
dans l'**École Doctorale de physique**

L'eau confinée dans des matériaux nanostructurés

Thèse soutenue publiquement le **23 novembre 2015**,
devant le jury composé de :

Prof. Jean-Louis BARRAT
Université Joseph Fourier, Grenoble, Président
Prof. Marco SAITTA
Université Pierre et Marie Curie, Paris, Rapporteur
Prof. Ralf EVERAERS
Ecole Normale Supérieure, Lyon, Rapporteur
Dr. Alessandro BARDUCCI
Ecole Polytechnique Fédérale de Lausanne, Suisse, Membre
Dr. Sandrine LYONNARD
CEA Grenoble, Directeur de thèse
Dr. Stefano MOSSA
CEA Grenoble, Co-directeur de thèse

Acknowledgements

I would like to thank my supervisors Sandrine Lyonnard, Stefano Mossa, and Timothy Ziman. Sandrine, thank you for your precious help, your encouragements, and your enthusiasm with this work. Stefano, thank you for your continuous support and for trusting me more than I trust myself, your contribution to this work is invaluable. Tim, thank you for the discussions, excellent advice, and your always positive attitude.

I would also like to thank Marco Saitta and Ralf Everaers for refereeing this work, as well as the other members of the committee: Jean-Louis Barrat, Alessandro Barducci and Dominique Bicout.

All the members of the theory group have contributed to this work by always being friendly and supportive.

It was not always obvious that I was going to be a scientist, and I would like to thank Michel Albertini and Giuseppe Foffi for their positive influence during high school and university respectively.

Finally, I would like to thank Solène, as well as all my family and friends for their patience and understanding. Now you know where all this time has gone.

Contents

Introduction

Water is everywhere and is essential to many processes in fields as diverse as biology, geoscience, energy and environmental science and technology. However, it is often found hidden in tiny cells, pores, or channels. For instance, water in living cells is the medium in which most biological events take place. Filters where water is driven through carbon nanotubes are being developed, with applications in waste water decontamination, water desalinisation plants, and other industrial processes. Hydraulic fracturing, a technique developed in the mining industry, consists in injecting pressurised water into porous ground in order to form cracks through which hydrocarbons can be extracted. Water is also essential to the function of electrochemical devices for new technologies for energy applications such as fuel cells, in which it is confined in a polymer membrane that separates the electrodes of the device.

In confinement, the usual "bulk" features of water are modified by the limited available space and the interactions of individual molecules with the confining material. In which way does confinement influence how water molecules coordinate among each other? How to describe the motion of water molecules when in confinement? Is water transported according to the same mechanisms, or is a new approach necessary? What happens to small elements dissolved in water under confinement? Elucidating the properties of water in such confined states is critical and general understanding can only be achieved through models. One one side, models that describe the structure and the transport properties of the samples are needed to interpret experimental data. On the other side, simulations rely on a basic model of the molecules and their interactions to provide a solution to the physical equations.

Water confined in model hard materials such as carbon nanotubes and glasses has been extensively studied, both experimentally and numerically. In biology, numerous models have been developed to study a specific biomolecule or biomacromolecule, and its interaction with water. However, we found that there exist no general numerical model to study water confined in soft materials.

In this thesis, we present a model of explicit water molecules confined in soft self-assembled environments. We have tackled the question of the influence of water on

the nanostructure of ionic surfactant assemblies, and that of the interplay between the nanostructure and the transport properties. Ionic surfactants are amphiphilic molecules that consist of a chain of highly hydrophobic units (the tail), terminated by a charged, highly hydrophilic unit (the head). The strong amphiphilic character of these molecules results in extremely neat phase separation when in the presence of water. The essence of our model is to include the minimal amount of parameters to allow the detailed study of the transport properties and of the nanostructure on the time-scale of the nanosecond. This versatile model is able to self-assemble to a wide variety of confining geometries, such as lamellar, cylindrical, and micellar arrangements, which can be precisely adjusted by varying the amount of water in the samples. This model can also be adapted to study more complex materials, and in particular we have extended it to study polymers.

This document is organised in two parts. In part I, we give a short overview of the materials that helped us in this thesis work and we consider a necessary background for the reader. We start in chapter 1 with a concise reminder of key concepts of statistical mechanics, in particular applications of the central limit theorem to random walks and diffusive processes. In chapter 2, we review the literature on the properties of water, from those in the bulk case to those in confining environments of different nature. We also discuss the properties of excess protons in water, in the bulk and in confinement. The aim of chapter 3 is to give an introduction to the domain of ionomers, with emphasis on their application as fuel cell membrane materials. We close part I by exploring the literature on ionic surfactants, and stressing in particular their role as model materials to understand ionomers.

Part II contains the bulk of our scientific contribution. We begin with chapter 4 by explaining the different choices we had to make to successfully build a versatile model of ionic surfactants: from the water model to our coarse-graining strategy for the surfactant molecules themselves, along with the simulation procedure we used to generate our samples. In chapter 5, we present the result of our analysis of the structural properties of the samples. Chapter 6 contains a detailed discussion of the dynamical features and transport properties of our model. As perspective, an investigation of the extension of our model to polymers is presented in chapter 7. Here, we explain how to build a model for polymers based on our model of surfactants, and we investigate the nature of the transport processes in hydrated polymers. We also discuss preliminary results on the structure properties of polymers doped with surfactants.

Finally, in chapter 8 we draw the general conclusions of this work.

2

Part I

Background

Chapter 1

Diffusion and anomalous diffusion

As we saw in the introduction, in this thesis we will be studying the transport properties of water molecules at the nanoscale. It is easy to imagine that we will have to deal with large numbers of water molecules, and therefore it is useful to use the tools of statistical physics to analyse their motion. The theory of diffusion describes the average motion of an ensemble of particles that exchange momentum so frequently that their motion appears as random. For example, it can be used to describe the probability distribution of the position of fluid molecules, or small molecules in suspension in a fluid. In this chapter, we give a short overview of the background necessary to comfortably address diffusive processes. This matter is covered in almost every statistical physics textbook, therefore we will not go into the details.

We will start by recalling the definition of a random walk as well as the Central Limit Theorem. Next, we will see how diffusion arises as a natural result of this theorem applied to random walks. We will then use the example of scaling laws in polymers to show how it is sometimes necessary to break the Central Limit Theorem to obtain the correct physical result. Finally, a similar reasoning will lead us to anomalous diffusion, where the randomness of collisions between diffusive particles break one or more hypothesis of the Central Limit Theorem.

1.1   Random Walks

Random walks are mathematical series of the form $\vec{r}_n = \sum_{i=1}^{n} \vec{v}_i$, where the individual terms $\vec{v}_i$ are chosen at random, hence their name. Each individual term can be viewed as one step, and the sum of consecutive steps constitutes a walk. In figure 1.1 we show a sample random walk in two dimensions. They are invaluable
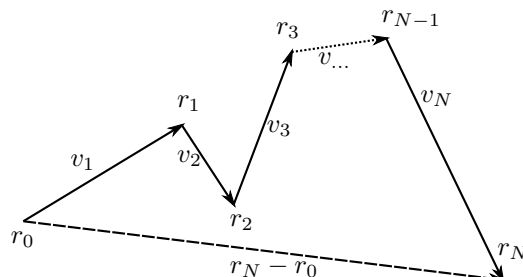
Figure 1.1: Random walk represented as the sum of vectors v_i connecting the different intermediate positions r_i.

tools for statistical physics, and can be used to describe complex phenomena. In this chapter, we will see how random walks can model the diffusion of fluid particles and the scaling of the size of polymers with the number of monomers, but a smart person can also use such random walks to better understand how insanely complex systems such as stock markets work. In this chapter we want to present a few examples, as the concepts introduced here will be central to our discussion of transport in disordered media. The most important mathematical tool in this chapter is the central limit theorem (CLT), which may be expressed as [1]:

Central Limit Theorem: Let $\{v_i\}_{i=1}^N$ be a sequence of N independent and identically distributed random variables, with expected value μ and variance σ^2. Then for all finite $r_{\min}, r_{\max}$ the sum $r = \sum_i v_i$ obeys:

$$\lim_{N \to \infty} P\left(r_{\min} \leq \frac{r - \mu N}{\sigma \sqrt{N}} \leq r_{\max}\right) = \int_{r_{\min}}^{r_{\max}} \frac{1}{2\pi} e^{-r^2/2} \mathrm{d}r, \qquad (1.1)$$

that is, the probability distribution function of the sum of independent and identically distributed random variables of finite variance is Gaussian in the range $[r_{\min}, r_{\max}]$. A direct consequence of this theorem for the random walks is that if the steps of the random walk satisfy the hypothesis of the CLT, then the distribution probability of r tends to a Gaussian for large N.

We will see here how this theorem applies in several physical systems, and more importantly how one has to go beyond the CLT to explain some phenomena.

1.2 Diffusion

A straightforward application of the central limit theorem is the description of the motion of particles with seemingly random motions, referred to as diffusive motion. Consider a Brownian particle: observation shows that at regular intervals

the particle's velocity changes in a random manner. The position of the particle can then be described as a random walk $\vec{r}(t_n) = \vec{r}_n = \sum_{i=1}^{n} \vec{v}_i$, with the Maxwell-Boltzmann probability distribution of each component of the velocity $\vec{v}$ (here we write the distribution for the x direction):

$$f(v_x) = \sqrt{\frac{m}{2\pi kT}} \, e^{-\frac{mv_x^2}{2kT}}, \tag{1.2}$$

which mean is $\langle v \rangle = 2\sqrt{\frac{2KT}{\pi m}}$ and which variance is $\langle v^2 \rangle = \frac{dKT}{2m}$, where d is the dimensionality, m is the mass of the particle, and k is Boltzmann's constant. The mean squared displacement (MSD, equation 1.3) is commonly used to described diffusive processes. Given N trajectories, the MSD describes the average squared displacement as a function of time.

$$\langle r^2(t) \rangle = \frac{1}{N} \sum_{i=1}^{N} |\vec{r}_i(t) - \vec{r}_i(0)|^2 \tag{1.3}$$

All the hypothesis of the central limit theorem are fulfilled, and therefore we have the following expression for the mean squared displacement:

$$\langle r_n^2 \rangle = n \langle v^2 \rangle, \tag{1.4}$$

where $\langle \cdot \rangle$ denotes the average over several sample trajectories. We will refer to such $r_n \sim \sqrt{n}$ behaviour as *Fickian*, or *diffusive* throughout the rest of the manuscript.

The diffusion coefficient D from Fick's law of diffusion can be linked to the above diffusion equation in the following manner:

$$\langle r_n^2 \rangle = n \langle v^2 \rangle = 2dDt_n. \tag{1.5}$$

Equation 1.5 is Einstein's relation for the diffusion. Obviously, in a simulation this equation can be used to compute the diffusion coefficient of atoms from their mean squared displacement.

We will see in chapter 2.3 that confined water sometimes exhibits a non-diffusive mean squared displacement. This behaviour cannot be modelled with a standard random walk due to the CLT. In the next sections, we will show how an example of random walk with well chosen steps can escape the CLT, and how this affects our description of the transport in such systems.

1.3 Polymers

Polymers are molecules that are made of a repetition of an individual unit, the monomer. Each monomer in the chain is linked to the previous and to the next

monomer by a chemical bond, which imposes a certain distance Δ between two consecutive monomers. If a polymer is hydrophobic and is immersed in water, it is energetically favourable for it to form a roughly spherical object, as this allows it to minimise the surface area that is in contact with water. One may be interested in computing the average size of this sphere, and in particular the dependence of the radius of the sphere on the number of monomers N in the polymer. This problem is discussed most elegantly in de Gennes' book, *Scaling Concepts in Polymer Physics* [2], and we give the main arguments here. One approach may be to write the position of each monomer as a function of all the previous ones:

$$\vec{r}_n = \vec{r}_{n-1} + \vec{v}_n, \tag{1.6}$$

where $\vec{r}_n$ is the position of monomer n, and $\vec{v}_n$ is the vector connecting monomers $n-1$ and n. Here, $|\vec{v}_n| = \Delta$. Therefore the average end-to-end distance (the equivalent of the mean squared displacement) is written as

$$\langle \vec{r}_n^2 \rangle = \sum_{ij} \langle \vec{v}_i \cdot \vec{v}_j \rangle. \tag{1.7}$$

If the position of two neighbouring monomers is assumed to be independent ($\langle \vec{v}_i \vec{v}_j \rangle = \delta_{ij} \langle \vec{v}^2 \rangle$) and identically distributed, the central limit theorem quickly leads to

$$\langle \vec{r}_n^2 \rangle \sim n \langle \vec{v}^2 \rangle. \tag{1.8}$$

We therefore find that the end-to-end distance of this model polymer scales as the square-root of the number of monomers, $\sqrt{\langle \vec{r}_n^2 \rangle} \sim n^\nu$, with $\nu = 1/2$.

Remark how the above $\vec{r}_n^2 \sim n$ behaviour originates from the CLT. However, in the case of real polymers one finds experimentally that the end-to-end distance of the polymer scales as $\nu \approx 3/5, 3/4, 1$ in 3,2, and 1 dimensions respectively. Thus, a necessary condition for this model polymer to be correct is that it features $\vec{v}_i$ that break the hypothesis of the CLT. In the case of polymers, this problem is solved by introducing the notion of excluded volume: to each monomer is attributed a volume in which other monomers cannot enter. This behaviour can be modelled in a particular type of random walk, called Self-Avoiding walk. In this type of walk, one requires that $|\vec{r}_i - \vec{r}_j| \geq \Delta$ for all $i \neq j$. This allows the introduction of long-ranged monomer-monomer interaction, *i.e.* that is effective even between monomers that are separated by many others. As a result, the $\vec{v}_i$ are not independent, which breaks the CLT and results in the proper exponent for the scaling law.

In this section, we saw how it is sometimes necessary to break the CLT to properly model stochastic processes. We will now see how breaking the CLT affects diffusive processes.

1.4 Anomalous diffusion

Anomalous diffusion may occur in a random walk when the steps v_i do break the hypothesis of the central limit theorem. In the case of the diffusion, the hypothesis of the Central Limit Theorem are the following:

1. the particles may be considered independent,

2. there exists a time scale at which individual displacements are independent, and

3. the displacements have a finite expectation value and variance.

Obviously, in the case of diffusion a Self Avoiding Walk makes little sense, but there are other examples which lead to non-linear mean-squared displacement. Here we give a few examples taken from two excellent reviews that deal with anomalous diffusion [3, 4].

In the case of Continuous Time Random Walks (CTRWs) the time interval between two jumps is random. In the literature, this time is often referred to as waiting time, or trapping time. If the distribution of trapping times exhibits an infinite average, as is the case for power law distributions $P(x) \sim x^{-\nu}$ with exponent $\nu \in [1:2]$, then the second criteria for diffusion (see above) is not satisfied: there is no characteristic waiting time between displacements. In this case, this leads to a mean squared displacement of the form $\langle \vec{r}^2 \rangle \sim t^{\nu-1}$. This type of behaviour is referred to as *subdiffusion*, because the mean squared displacement scales as a power law of time with exponent $\nu - 1 < 1$.

Fractional Brownian Motion (FBM) introduces correlations between successive displacements, that decays as a power-law of the time-difference between two displacements: $< \vec{v}_i \cdot \vec{v}_j > \sim |i - j|^{\alpha-2}$. This leads to a mean squared displacement of the form $\langle r^2 \rangle \sim t^{\alpha}$, and therefore for $0 < \alpha < 1$ we recover the subdiffusive behaviour.

If subdiffusion is observed, one can differentiate between CTRW and FBM by checking the ergodicity of the random walk. This can be achieved by computing the time averaged mean squared displacement

$$\text{TAMSD}(n) = \langle (r_{i,n+n_0} - r_{i,n_0})^2 \rangle_{i,n_0}. \tag{1.9}$$

One can show that CTRW as presented here is non-ergodic, while FBM is ergodic. If $\text{TAMSD}(n) \neq \text{MSD}(n)$, then the system is non-ergodic, and therefore one has to differentiate between *ensemble averaged* and *time averaged* quantities. This

means that additional precautions might have to be taken when analysing data from experimental samples or numerical simulations exhibiting anomalous diffusion.

In the context of subdiffusion, the fluctuation-dissipation Einstein relation between the mean-squared displacement and the diffusion coefficient does not hold in the usual form. We can however define a time and length-scale dependent generalised effective diffusion coefficient, D_{eff}, from the local slope of the mean-squared displacement as [5],

$$\partial_t \langle r^2(t) \rangle = \frac{\alpha}{t} \langle r^2(t) \rangle = 6 D_{\text{eff}}. \tag{1.10}$$

In this chapter, we have re-introduced the basic mathematical tools used to model some stochastic processes. We showed how diffusion and anomalous diffusion can be obtained from the application or the breaking of the Central Limit Theorem. As we saw in the introduction, our goal is to study these transport processes in the cases of water and protons in confinement. We will see that the behaviour of water and protons is non trivial, and is not yet fully understood. It is therefore useful to start by studying the simpler case of bulk water, and progressively increasing the complexity of the problem by adding excess protons and finally confinement. In the following, we will review the literature related to the properties of water in bulk and under confinement, as well as those of excess protons, and we will see how confined water and ions may exhibit anomalous diffusion.

Chapter 2

Structure and dynamics of water and protons

Many molecular processes rely on the peculiar properties of water. Perhaps the most obvious examples are found in biology, where objects as diverse as proteins, nucleic acids, and membranes are surrounded by water and whose properties are linked to those of water [6, 7, 8]. But biology is not the only domain where the properties of water play a crucial role. For instance, understanding the behaviour of water in porous geological materials is key to the extraction of oil and natural gas (see for example [9] for a non technical description of the extraction processes), and porous clay-based materials are used to decontaminate water [10]. Most important for this work, the interest of amphiphilic ionomers lies in their excellent ability to conduct protons, a property that stems from their interaction with water. Because they feature both hydrophilic and hydrophobic domains, these materials are able to form well defined nanometric channels in which protons are transported [11]. In this chapter we review some work drawn from the literature pertaining to water, with a particular emphasis on simulation. We start by considering the properties of water in bulk, then we focus on the properties of excess protons in bulk water. We then review the effect of confinement on water and hydrated ions. In the next chapter, we will revisit the confined state in the case of water adsorbed in ionomers and similar materials.

2.1 Bulk water

The properties of water are well documented. In particular, the phase diagram (see figure 2.1) of water is extremely rich, and has received tremendous attention [12, 13]. This is a seemingly bottomless topic, and regions of the phase diagrams are still being discovered [15]. Compared to other common liquids, water is highly anoma-
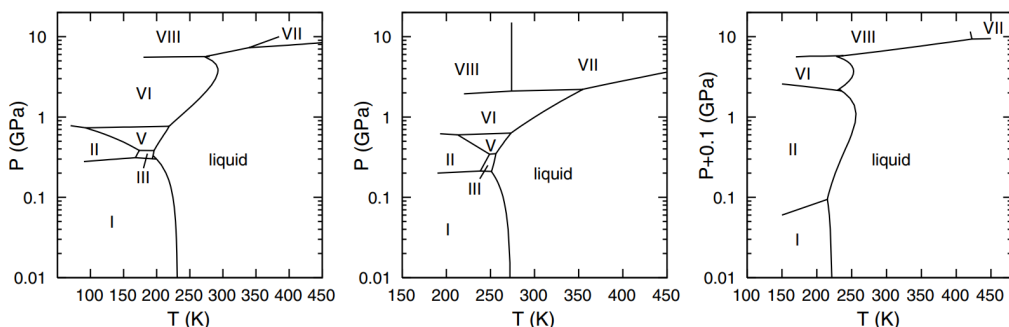
Figure 2.1: The phase diagram of water from experiment (centre) and computer simulations of TIP4P (left) and SPC/E (right) water models. Adapted from [14].
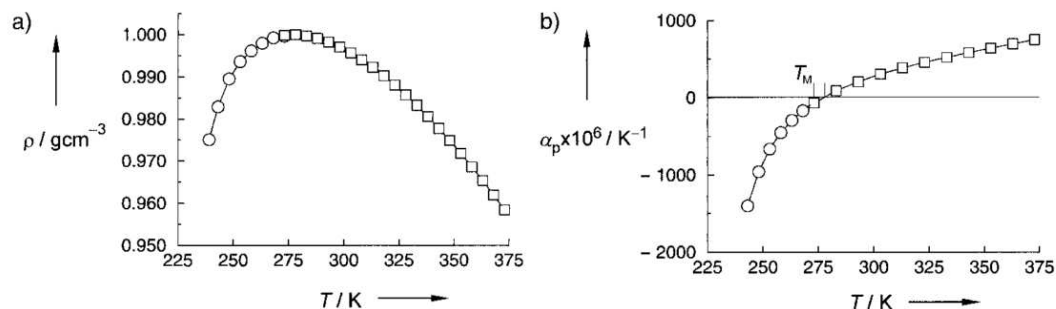

Figure 2.2: **Structural anomalies of water.** Temperature dependence of the density (a), and volume expansion coefficient (b) of water. Adapted from [16].

lous. For instance, water is one of few liquids (along with liquid SiO_2) to exhibit a maximum in the dependence of density on temperature, and the specific volume of liquid water is lower than that of ice (see figure 2.2) [16]. Similar observations have been made in molecular dynamics simulations of water (for instance, [17]). The dynamical properties of water also differ from the expected behaviour of liquids: up to 200 MPa the diffusion coefficient increases, and the usual (decreasing) variation is recovered at higher pressures (figure 2.3 (a)). Moreover, the variation of the viscosity of water significantly deviates from the usual T^{-1} behaviour (figure 2.3 (b)).

These anomalous properties are driven by the size and the dipole moment at the individual level, and by the ability to be polarised and to form hydrogen bonds at the collective level [18, 19]. These properties can be probed by a wide range of experiments, such as absorption of infrared light [20], Raman scattering [21] and neutron scattering [22]. In particular neutrons are an ideal probe of the structure
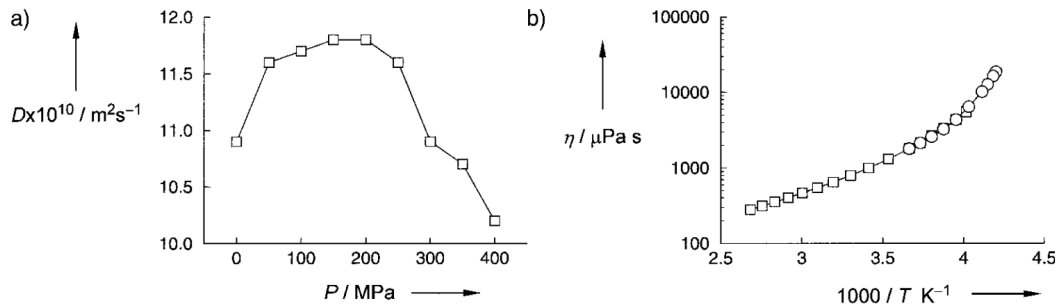
Figure 2.3: **Dynamical anomalies of water.** Pressure dependence of the diffusion coefficient (a), and temperature dependence of the viscosity (b) of water. Adapted from [16].
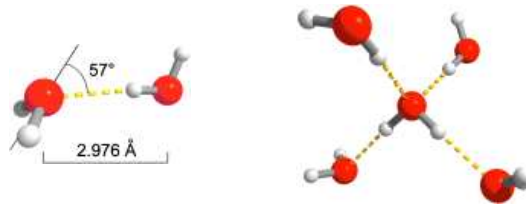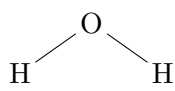
Figure 2.4: Left: hydrogen bond between two water molecules. Right: the tetrahedral structure of liquid water. Adapted from [16]

and dynamics of water due to its high proton content. The ability to deuterate water offers even richer opportunities [23].

Numerical techniques have also been very successful in refining the molecular models and in unravelling the details of the structure and of the dynamics liquid water. Perhaps one of the most powerful approach is the Car-Parrinello method for coupling molecular dynamics with density functional theory [24]. This technique uses on one side molecular dynamics to solve the equations of motion of nuclei, and on the other side density functional theory to compute the electron density from which the potential energy surface and the inter-atomic forces are derived. This technique successfully predicts the structure of liquid water, both in terms of radial distribution functions, simulated X-ray scattering intensities, hydrogen bond angles and statistics [25].

In terms of local structure, the consensus is that liquid water molecules have on average four nearest neighbour, and four hydrogen bonds [26]. It is interesting to note however that the exact definition of hydrogen bond is still debated, and can affect the interpretation of experiments. For example, a certain interpretation of X-ray absorption experiments based on slightly different geometrical and energetic

13

	SPC [29]	SPC/E [30]	TIP3P [28]
r_{OH} [Å]	1	1	0.9572
$\widehat{\mathrm{HOH}}$ [°]	109.47	109.47	104.52
q_{O} [e]	-0.82	-0.8476	-0.834
q_{H} [e]	$+0.41$	$+0.4238$	$+0.417$
σ_{OO} [Å]	3.166	3.166	3.15066
ϵ_{OO} [kcal/mol]	0.1554	0.1554	0.1521

Table 2.1: Three point water models have three interaction sites on a triangle. In the table, we summarise the values of each parameter for the SPC [29],SPC/E [30], and TIP3P [28] models.

criteria suggest that water molecules would only form two hydrogen bonds [27]. This interpretation is however very controversial (see [26] and references therein). While the Car-Parrinello technique is very powerful, its computational cost is often prohibitive, and therefore alternative approaches have been developed, purely within the molecular dynamics framework.

One of the approaches to numerical simulations of water is the effective pair potential approach. Several such models have been developed, that represent water as ensemble of Coulombic and van der Waals interaction sites: TIP3P [28], SPC [29] and SPC/E [30] are some commonly used models. These models consist of three interaction sites per particles, that interact *via* Lennard-Jones (LJ) and Coulombic potentials (see table 2.1) They feature slight differences in the values of the parameters of their interaction potentials, that lead to differences in the macroscopic observables such as the density, potential energy and diffusion coefficient [31]. In the framework of these effective potentials, it is possible to empirically derive geometrical criteria for the formation of hydrogen bonds [32, 33], and such effective potential models have been implemented to study the hydrogen bond network and its relaxation [18, 19, 34].

Hydrogen bonding is responsible of the peculiar transport properties of water. In simple words, how is a water molecule able to move while embedded in a relatively strong network of bonds? This issue is of particular importance when studying transport on the time scale of the lifetime of the bonds (of the order of 100 fs [35]), as it is the case for instance in time of flight neutron scattering [36]). Neutron scattering experiments on water showed that the dynamics of water can be decomposed in two contributions: rotational diffusion, which accounts for the reorientation of water molecules, and translational diffusion, where the orientation of the water molecule is kept constant but it position changes. These two motions are coupled at ambient temperature, but at low temperature one can assume that
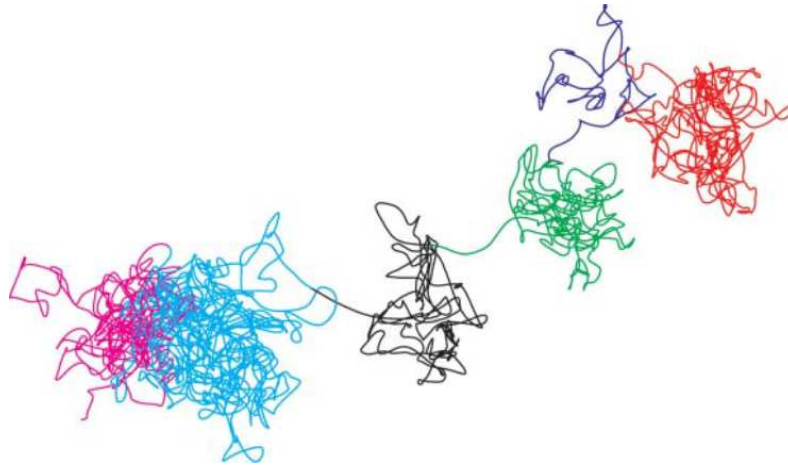
Figure 2.5: A 75 ps trajectory of a water molecule, computed by molecular dynamics. The trajectory consists of basins (colour-coded), between which the water molecule jumps. Adapted from reference [37].

they are independent. Based on scattering experiments supported by molecular dynamics simulations, it is now understood that translational diffusion of water exhibits two distinct regimes: at the picosecond scale molecules diffuse within basins which size is roughly one Ångström, and after several picoseconds they jump to a neighbouring basin (see figure 2.5) [37]. This mechanism is well described by a continuous time random walk: the trapping time of the walk corresponds to the motion of water in basins, and water is allowed to jump instantaneously from basin to basin.

The fact that the motion of water molecules is well described by a continuous time random walk is particularly interesting: we saw in the previous chapter that this type of walk can lead to sub-diffusive transport. In section 2.3, we will see that confining water modifies the nature of transport, and that in particular sub-diffusion is often observed. But before that, we want to give a brief overview of the behaviour of excess protons in water, as this will be one of the focal points of our model.

15

Figure 2.6: **a-c:**Illustration of the Grotthuss mechanism. Charge transfer takes place via an interchange of chemical and hydrogen bonds. Adapted from [38]. **d:** vehicular transport of a proton on a H_3O^+ ion.

2.2 Excess protons in bulk water

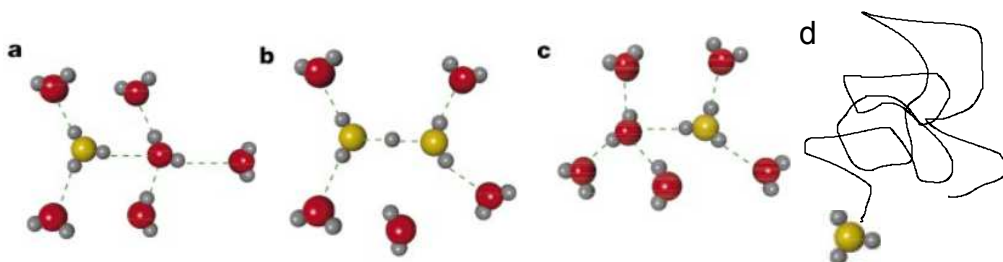Protons are not free in water, they bind to a water molecule and form the so-called hydronium ion, H_3O^+, as well as larger cations involving multiple water molecules. Perhaps surprisingly, the properties of these ions are not similar to those of cations of similar mass and charge (K^+ for instance), and in particular the mobility of hydronium is substantially higher [38]. This is not explained by the classical description of vehicular transport, where the transport of the charge is controlled by the transport of the mass. To solve this problem Grotthuss imagined a different transport mechanism where ions would continuously break and form bonds with water molecules, effectively transporting the charge from water molecule to water molecule [39]. The validity of this concept was later demonstrated in *ab initio* simulations: excess protons in water form Eigen ($H_9O_4^+$) and Zundel ($H_5O_2^+$) defects in the hydrogen bond network. Fluctuations induce rearrangements of the network around these defects and protons can be re-localised on a different water molecule [40]. This type of charge transport is called *structural diffusion* and is shown in figure 2.6.

While *ab initio* simulations have been instrumental in clarifying the mechanism of transport of the proton, they are exceedingly demanding computationally for large scale simulation purposes. Alternative routes to the inclusion of proton hopping in a simulation have been developed, where an empirical description replaces the accurate but expensive computation of the potential energy surface. Probabilistic approaches combine classical molecular dynamics with geometrical criteria to compute the probability of the proton jump [41]. Empirical valence bond techniques [42] are proper quantum mechanical techniques that can describe chemical reactions while being lighter than *ab initio*, but require more prior knowledge on the potential energy surface. This approach has been applied with some success to the case of the transport of the excess proton in water [43].

2.3 Water and protons in confinement

As we have seen above, water exhibits a wide range of peculiar features, most of them originating from the network of hydrogen bonds. However so far we focused only on the case of bulk water, while in many materials water is confined in nanometer scale pores or channels. What is the influence of confinement on the properties of water? How is the complex mechanism of structural diffusion of protons affected by the confinement? In this section, we review selected work that tackle this issue. We will address the effect of confinement size as well as the nature of the confining matrix on the structural and dynamical properties of water.

2.3.1 Apolar interfaces

Apolar molecules are known to be poorly soluble in water: this is the classic problem of mixing water with oil. The physical origin of this "hydrophobic" effect is once again the hydrogen bond network of liquid water: as the bound state is of lower energy than the free state, introducing an unbound defect in the network is unfavourable. Therefore, mixing water with apolar molecules results in a phase separation between the aqueous phase and the apolar phase, and the most favourable configuration is the one with the lowest contact area between the two phases. While this may seem intuitive, the quantitative theory of these effects was only derived recently [44, 45]. Apolar confinement occurs when such phase separation results in nanometric scale aqueous domains, as is the case in proteins [46], reverse micelles [47], and carbon nanotubes [48].

Carbon nanotubes offer a well defined and adjustable playground for the study of water confined in matrices of various nature: it is possible to functionalise carbon nanotubes with molecules of desired properties, for instance with fluorine [49], or sulfonic acids [50]. Water structure in a carbon nanotube has been studied by molecular dynamics [51, 52] and by neutron scattering [52]. When the confinement is increased by reducing the diameter of the nanotube, the average number of hydrogen bond decreases due to the lack of available neighbour with which to bind. When the diameter of the tube is increased above 3 to 4 Å, this reduction in the number of bonds in only observed in the interfacial layer, the value in the centre of the tube being unaffected in comparison to that in the bulk. In the highly confined case, the structure of water in the tube is that of a single file conformation, with the hydrogen bond parallel to the tube axis. For larger diameters, the arrangement of water can be a central single file surrounded by concentric layers of molecules [52], helix-like [53], or ring-like structures [50].

The dynamics of water in carbon nanotubes differ significantly from that in the bulk, yet it also depends on the fluctuations in the hydrogen bond network. Molecular dynamics simulations [48, 52] and inelastic neutron scattering [52] revealed

17
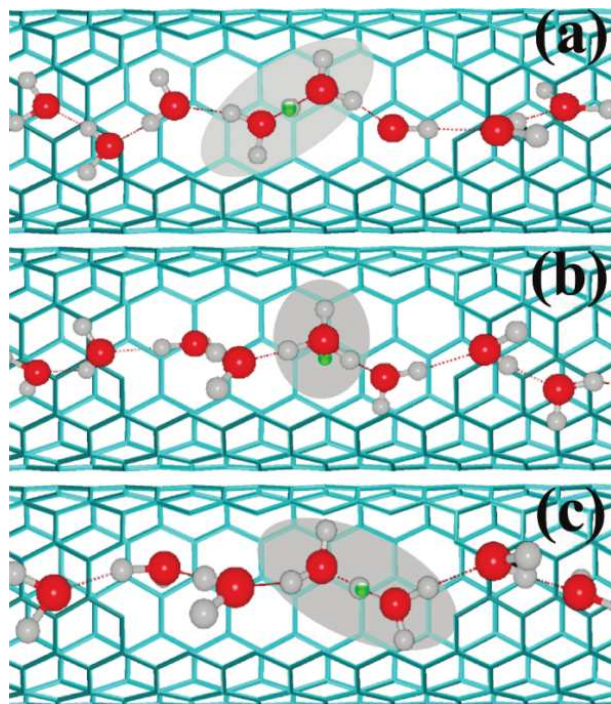
Figure 2.7: Snapshots illustrating the transfer of an excess proton in one-dimensional water chain confined in a (6,6) CNT. a) Zundel, b) Eigen, and c) Zundel ions are shown highlighted in grey. Adapted from reference [58].

that water flows through the carbon nanotube in bursts that are synchronised with the rearrangements of the hydrogen bond network of the central single file. Similar properties are observed in the aquaporin family of proteins, which transport water through a hydrophobic channel with great efficiency [46]. In any case, the lack of hydrogen bonding of water absorbed in these apolar confining matrices results in faster transport than that predicted by a simple Poiseuille flow model [46, 54, 55, 56].

Molecular dynamics simulations of proton transport in carbon nanotubes showed that protons move across the single file of water molecules about 40 times faster than in the bulk [57]. This high mobility is due to the unidimensional character of the hydrogen bond network in the single file configuration of water in the carbon nanotube, and the mechanism of structural transport is slightly different than that of protons in bulk water: protons hop from one water molecule to the next via a Zundel-$H_7O_3^+$-Zundel, instead of Eigen-Zundel-Eigen [58].

As we have seen in this short overview of water in apolar confinement, the properties of confined liquid water are fundamentally different from those of bulk

water, and precise treatment of all the details of transport and structure of water and protonated complexes is prohibitively expensive to implement in a large scale simulation. We will now shortly review the case of polar confinement.

2.3.2 Polar interfaces

Water in polar confinement has been studied in model hydrophilic plates [59], porous Vycor glass [60, 61], reverse micelles [62], and in biological systems such as lipid membranes [63, 64, 65] and proteins [66, 67, 68, 69, 7, 70]. Hydrophilic confinement contrasts with the case of hydrophobic confinement, in that the water molecules form tight structural bonds with the matrix, sometimes disrupting the water-water network of hydrogen bonds. This was observed in Vycor glass [61], and in biological systems [64, 66, 67, 68, 69]. The most extensive literature concerning the properties of water confined in soft materials in found in the field of biology, where knowledge of the behaviour of water at the interface of a protein or in regions neighbouring a biological membrane is key to determining the structure and dynamics, and therefore the function, of such systems.

It is generally understood that the dynamics of water around biological objects differs substantially from the bulk properties [7]. In particular, transport is known to be non-diffusive due in part to the trapping of water molecules in the interfacial layer [63], and simulation study revealed sub-linear mean square displacements [68, 64]. Several attempts have been made at explaining sub-diffusion in the context of proteins and membranes [68, 65, 71]. The usual approach is to assume that the motion of water molecules cannot be described by a standard Brownian random walk, but rather one has to assume another stochastic model for the transport, as we have seen in chapter 1. One can distinguish three main stochastic models which can give rise to sub-diffusive transport: fractional Brownian motion, continuous time random walk, and diffusion on a fractal lattice. These models of sub diffusion are reviewed in [3]. The idea behind these models is to introduce a random walk in which the displacement of the walker do not satisfy the hypothesis of the central limit theorem. As a result, the probability distribution of the position of the walker is non Gaussian, implying non-linear mean squared displacements at long times.

Detailed analysis of the molecular dynamics trajectories of water molecules in the vicinity of a lipid membrane reveal two key aspects[64, 65] (figure 2.8). First, the distribution of trapping times of water at the interface is a power law, and the exponent of this power law depends on the temperature. This is reminiscent of transport on a random energy landscape, and is known to give rise to sub-diffusion in a way that is reminiscent of continuous time random walks. Second, the motion of the heads of the lipids can be modelled by a fractional Brownian walk [72], and some properties of this type of walk is observed in the motion of water in the vicinity of the interface.
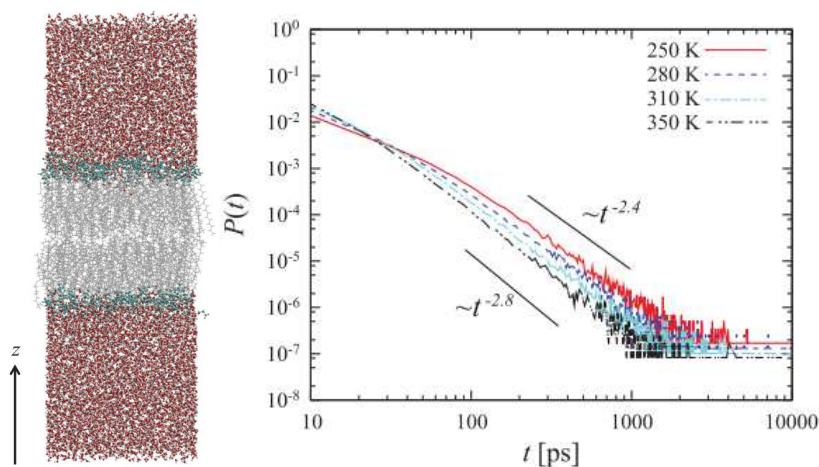
19

Figure 2.8: Trapping of water molecules in the vicinity of a lipid bilayer (left). The distribution of trapping times of water molecules at the interface exhibits power law behaviour (right). Adapted from [64].

Similar insights can be gained by studying the properties of hydration water[1] in proteins [66, 67, 68, 69] (figure 2.9). In these systems, sub-diffusive transport of water molecules is also observed [67]. Moreover, computing the survival time correlation function[2] reveals that it deviates from an exponentially decaying function, which also constitutes a hint of a spread in the distribution of the residence times of water at the interface [68]. Similarly, analysing the rotational motions of the water molecules indicate a slowing down of the rotational dynamics in the vicinity of the protein, with the associated correlation function decaying according to a stretched exponential [68].

Overall, the understanding of the complex properties of water is made even more complex in confined environments. In particular, the structural and transport properties of water are influenced by the extension and the polarity of the confining matrices. These effects are also evident in the case of water confined in amphiphilic ionomers, where the size of the aqueous domains as well as the amphiphilicity and density of charge of the polymer have been shown to modify the transport properties of the absorbed water. In the next chapter, we review the literature related to

---

[1]The hydration water is water that sits in the first layers around the protein.

[2]The survival time correlation function describes the probability for a molecule at the interface to stay at the interface as a function of time. It is analogous to the decay laws for radioactive species.

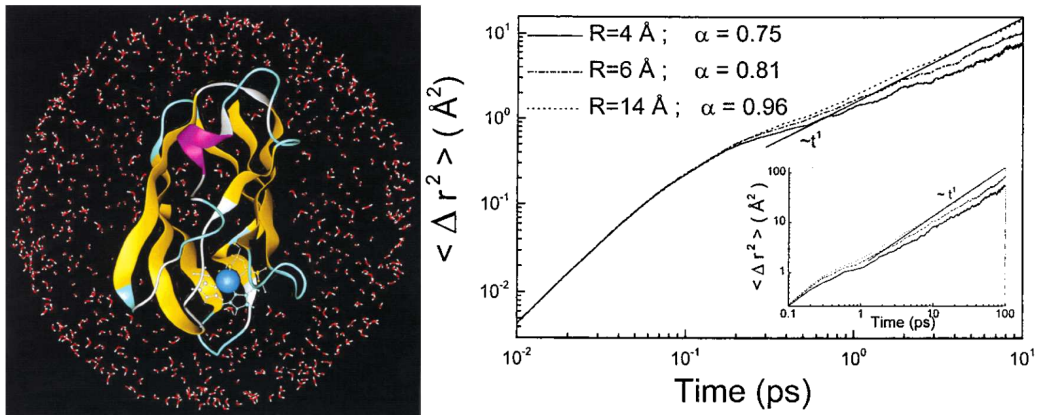Figure 2.9: Sub-diffusion has been observed in the hydration water that surrounds a plastocyanin proteins (left), leading to a sub-linear mean-squared displacement (right) The inset in the panel on the right shows the mean squared displacement from the same simulation from 0.1 to 100 ps. Adapted from [69].

hydrated amphiphilic ionomers, with a particular focus on the properties of water in these systems.

Chapter 3

Structure and dynamics of water and protons in ionomers

Ionomers are polymers that feature ionised side-chains bonded to a backbone. They are characterised by their *equivalent weight* (EW), defined as the mass of material per mole of charged group. Ionomers differ from polyelectrolytes in that their equivalent weight is typically much higher. These molecules are central to many applications, such as golf ball coatings, compatibilizing agents for the blending of polymers, packaging, membranes used for filtering of water, and for fuel cell applications [73].

In the case of fuel cells, ionomers membranes play the role of selectively separating the two electrodes. These membranes are impermeable to hydrogen and oxygen, and at the same time are good proton conductors. The performance of the membrane in terms of proton conduction is the key factor in fuel cell performance.

So far, best results have been achieved with materials of the class of perfluorosulfonic acids (PFSAs). These ionomers consist of fluorocarbon backbones and side chains, with sulfonic acid groups terminating the side chains (see figure 3.1). The backbone and most of the side-chains of these polymers is highly hydrophobic, while the end group is a strong acid which makes it hydrophilic and also gives it the ability to be ionised. Examples of such materials are the historical benchmark Nafion, and more modern competitors like Aquivion and 3M membranes. The differences between these molecules come from variations in side chain composition, length, and spacing along the backbone. In addition, the properties of these membranes depend on the industrial process employed to create the membrane.

Compared to other ionomers, these materials present the advantage of being composed of both hydrophilic and hydrophobic groups, and are as a result neatly phase separated when in contact with water (as is the case in an operating fuel cell). This phase separation leads to the formation of aqueous domains confined
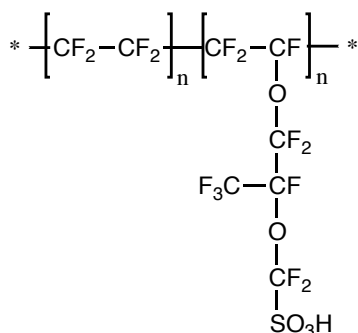
Figure 3.1: Structure of the Nafion polymer: on top, the Teflon backbone, from which the side chains branch at regular intervals. The equivalent weight can be adjusted by varying the spacing of the side-chains. For instance, 1100 g/eq Nafion has a side chains every 14 CF_2 backbone monomer. The dashed link between the SO_3^- and H^+ groups represents the ionisability of the side chain.

in polymeric nanostructures. These materials have been extensively studied both experimentally (by NMR, X-Ray and neutron scattering, FT-IR for example) and numerically by *ab initio*, all-atoms molecular dynamics, and mesoscale techniques. However many aspects remain unclear, and in particular the question of the interplay between the structural and transport properties are not fully understood.

There are multiple facets to this issue. The structure of these materials is complex, and is influenced by the nature of the side-chain, the water loading, the operating temperature, and even by external factors such as the fabrication process[1]. As we saw in the previous chapter, the mechanism of transport of protons in water is extremely complex, and is made even more complex by confinement. The nature of the confinement itself is part polar, part apolar, and the interface is also charged. In the next section, we review the state of the understanding of the structural properties of ionomers.

3.1 Structure of hydrated ionomers

As we have seen in the previous chapter, proton conduction can be vehicular or structural, and is highly influenced by the geometry and the nature (polar or apolar) of confinement. Therefore knowledge of the geometry of the volume available to water molecules is crucial. This is however an ongoing debate: while the structure of PFSA materials can be probed by X-rays [74, 75, 76, 11, 77] and neutrons [78, 79, 80], the experiments rely on models to extract physical quantities from the

---

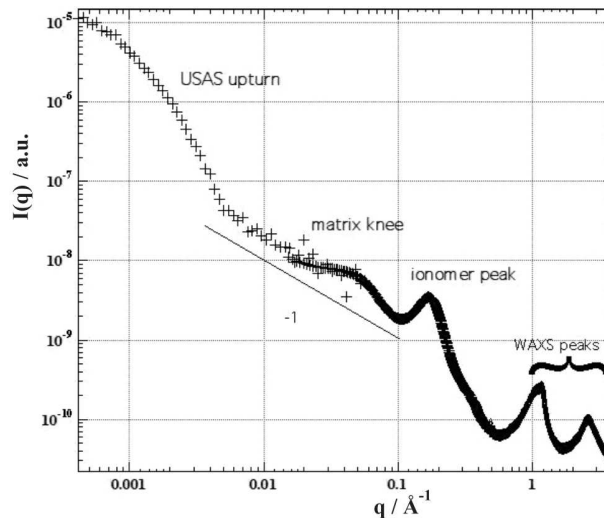[1]These materials are patented commercial products.

Figure 3.2: The static structure factor of Nafion, measured on a wide range of momentum transfers q [82]. The main features are discussed in the text.

data. Designing a robust model is highly non trivial, in particular because different models may result in the same spectra [11, 81], due to the loss of information on the phase and to Babinet's principle[2]. In addition, scattering techniques measure the static structure factor , which is an average quantity built from the position of all the atoms in the sample and averaged over all directions. It is therefore impossible to extract precise directional information on the local organisation of the atoms in the materials from scattering techniques. Moreover, precisely controlling all the experimental parameters that may influence the measurement, and in particular hydration and the fabrication process itself, is critical.

Before reviewing the model themselves, we provide an overview of the main features of a typical static structure factor of Nafion (reproduced from [82] in figure 3.2). The low q region (corresponding to distances larger than 100 nm) is characterised by a broad high intensity region, indicating long-range spatial correlations. A second broad bump in intensity is found at q-values corresponding to distances of the order of 10 nm, which is correlated with the amount of crystalline regions of the polymer matrix [11]. A well defined peak is found in the nanometer range, which originates from the nanostructuration of the polymeric and aqueous phases. This feature is characteristic of this class of materials, and is in general referred to as the *ionomer peak*. This peak is of particular importance in this work: its posi-

---

[2]Babinet's principle states that diffraction techniques are unable to differentiate between a mixture of material A in material B and a similar pattern but this time with materials A and B swapped.
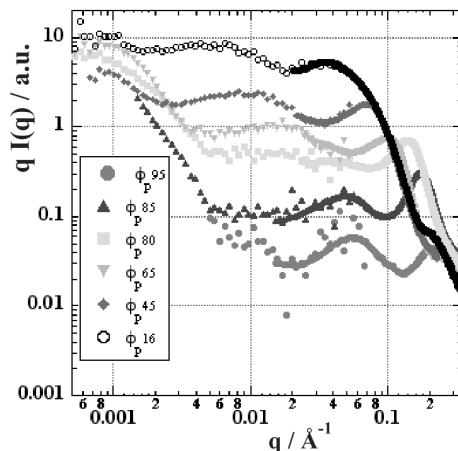
Figure 3.3: The static structure factor of Nafion, measured at multiple polymer volume fractions [82]. The overall shift to lower q-values with increased hydration is clearly visible.In the legend, Φ_P^X means that $X\%$ of the volume of the sample consists of polymer.

tion and width are related to the distribution of the size of the domains. Finally, other peaks are visible that tell us about the ordering of the system at the scale of the Ångström. They are attributed to correlations between adjacent polymers, and between adjacent monomers.

These features of the static structure factor are affected by the water content. In figure 3.3, we show the static structure factor of Nafion at different polymer volume fractions Φ_P. In general increasing the hydration shifts the matrix and ionomer peaks toward smaller q-values. This indicates that the distance between the features of the system increase with hydration, and their distribution becomes broader. A good structural model is one that is able to account for all the features of the static structure factor at all hydrations.

Several attempts have been made at modelling the structure of hydrated Nafion, and here we review the main contributions. The goal is to propose a mass distribution that generates the observed static structure factor. Gierke proposed an inverted micelles structure which at the time explained the main features of the X-ray spectra [74]. Since then, advances in scattering techniques allowed more precise measurements of the spectrum, which revealed additional features that cannot be explained by Gierke's model. A model of entangled fibrils made of elongated aggregates of polymers was later proposed as an improvement, based on simultaneous matching of X-ray and neutron scattering, AFM, and cryo-EM data [11]. The privileged hypothesis for the local structure of the aggregates was that of lamellar arrangement. An alternative structure of stacked cylindrical ionic nanochannels and

26

fluorocarbon crystallites was suggested after computing the X-ray spectra of several bidimensional arrangements [81]. This model features very wide aqueous channels, which was thought to explain the excellent conductivity of Nafion. However this model was later criticised for a number of shortcomings, most importantly for failing to account for variations in hydration [83, 84], and an alternative structure of lamellar arrangement was shown to better explain the swelling of the polymer in the low hydration regime [84]. We summarise the main structural models in figure 3.4.

Recently, the first high resolution electron tomography of the nanostructure of Nafion has been reported [85]. This is the first study that investigates the 3D internal structure of Nafion both in the dried and hydrated states. From the resulting images (see figure 3.5 for examples of 2D section and 3D reconstruction), it is clear that the nanostructure of Nafion is highly disordered.

Simulations are another tool to that has been used with some degree of success to study the structure of these materials. In figure 3.6, we show three examples of samples, simulated with different techniques. *Ab initio* electronic structure calculations have been performed to study the hydration state and the mechanical properties of one [89, 90], and two Nafion side chains connected with a fragment of polymer backbone [91, 86]. In the case of the single side chain the acid proton was found to dissociate at higher water content than expected given the super acidity of the sulfonic acid [90]. An important cooperative effect was revealed in the double side-chains case where the polymer backbone bends to bring the two head groups closer to surround water molecules [86]. In this "water bridge" conformation, the number of water molecules required to dissociate the protons is reduced: for instance, while five water molecules are not sufficient to dissociate two protons in the straight configuration, in the bridged conformation the two protons are dissociated [86]. In figure 3.6 (left), we show a structure optimised by *ab initio* simulation adapted from reference [86] where the bridge is observed. This particular example highlights the importance of collective effects in these complex systems. Anyway, these studies provided a first principles description of the hydration of the polymer as a function of water content, which confirmed the amphiphilic character of the side chains, with the head group being hydrophilic and the tail part being strongly hydrophobic. The water bridging of sulfonic groups was also observed in similar *ab initio* simulations of other ionomers [92], as well as in molecular dynamics simulations of Nafion [93, 94].

The structural properties at the nanometer scale can be studied by a wide variety of techniques, from Car-Parrinello [95] to mesoscale techniques [96, 88], via atomistic [97, 98, 99, 94, 83, 100, 95, 101] and coarse grained molecular dynamics [93, 102, 103, 104, 100, 105, 95]. In figure 3.6 (centre), we show a sample of hydrated Nafion polymer simulated by all atom molecular dynamics [87]. At this scale, the phase separation is visible, and the irregular character of the nanostruc-

27
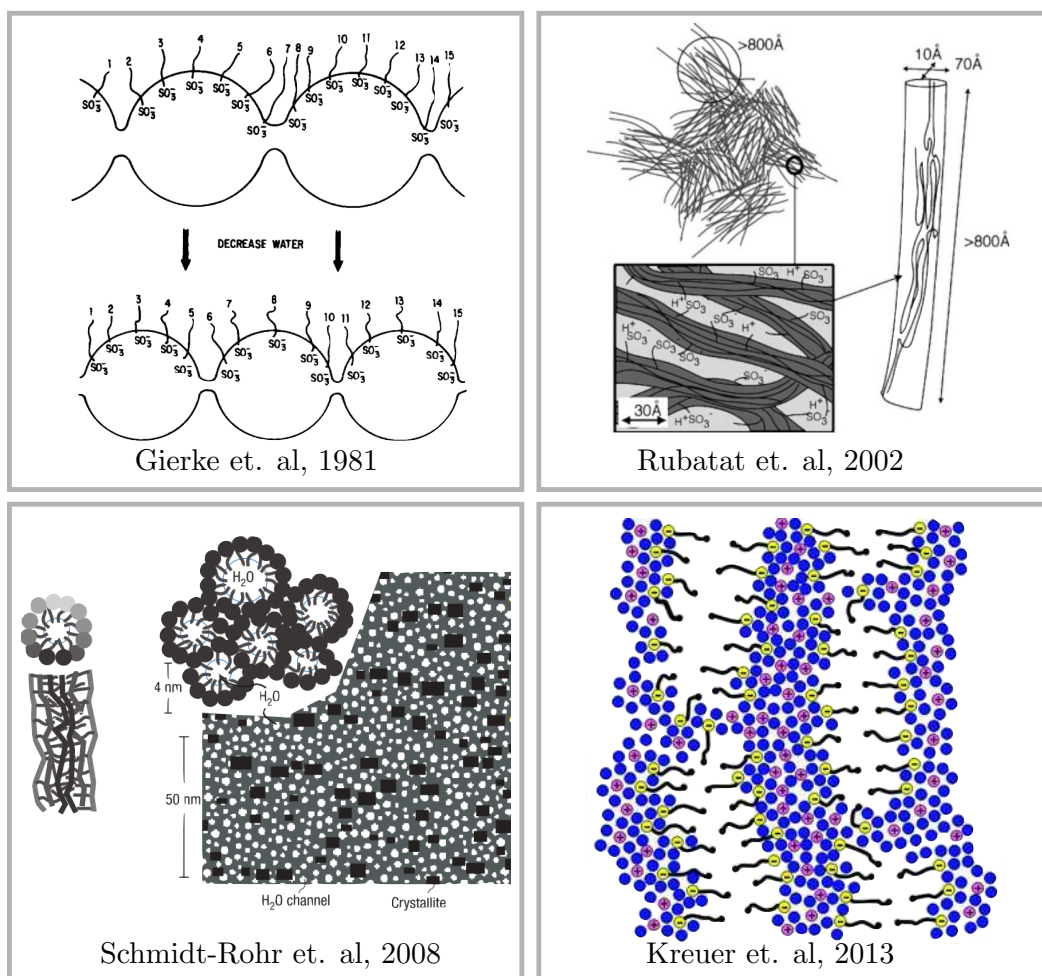
Figure 3.4: The main structural models of the nanostructure of Nafion: the inverted micelle model of Gierke (adapted from [74]), the fibrilar model of Rubatat (adapted from [82]), the model of cylindrical water channels (adapted from [81], and the model of locally lamellar aggregates (adapted from [84]).

ture is also apparent. In figure 3.6 (right), we show a sample of hydrated Nafion polymer simulated by the DPD mesoscale technique [88]. This technique allows the simulation of much larger samples (33 nm in this case), and the phase-separation between aqueous (blue) polymeric (red) domains is clearly visible. At this scale, no long-range order is apparent. The picture that emerges from the literature is that these materials form well defined interfaces between aqueous and polymeric regions, with irregular domain sizes and orientations. While overall the simulated
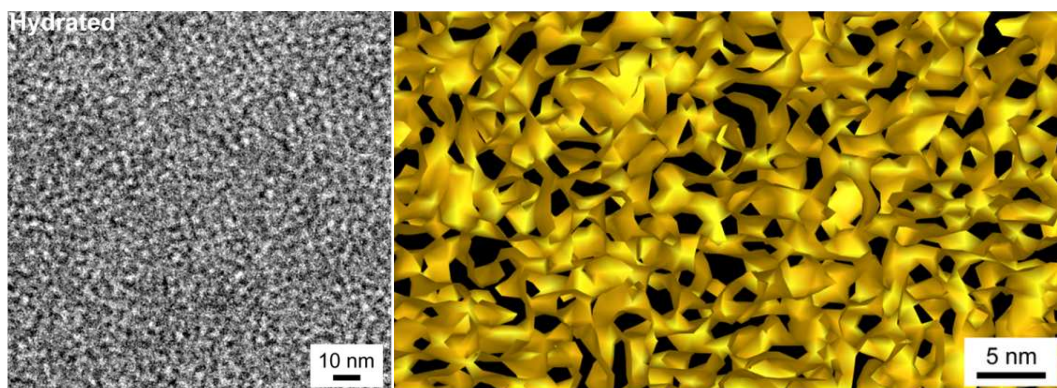
Figure 3.5: Left: cryo-EM image of an hydrated Nafion membrane. The phase separation and connectivity of domains is clearly visible. Right: cryo-EM tomographic reconstruction of the nanostructure of hydrated Nafion. The yellow volume corresponds to the hydrophilic domains. Adapted from [85].

structures invalidate the model of stacked cylindrical aqueous channels, they are too irregular to be considered consistent with the model of polymeric fibrils [88]. Moreover, the nanometer-scale structure is not dramatically influenced by the inclusion of the details of the electronic structure [95], and atomistic details seem to play only a secondary role for general features like the position of the ionomer and matrix peaks [96, 88]. While the self-assembled structures obtained from random initial configurations are anisotropic, applying an external force on the system leads to the persistent reorientation of both the backbone and of the side chains [103, 104, 105], and under very strong force to the formation of an hexagonal phase [104].

Overall, there is a general consensus on the idea that hydrated PFSA tend to form locally lamellar arrangements. It is also clear that the aqueous and polymeric domains are well separated, but that their size is rather irregular. Due to the intrinsically disordered nature of these materials, it is probably impossible to establish a definitive model of their structure.

3.2 Transport properties in hydrated ionomers

As we saw, the transport of protons is crucial to the function of fuel cells, and takes place in a relatively irregular network of aqueous domains delimited by a strongly hydrophilic interface. The transport properties of water and protons in hydrated PFSAs can be studied experimentally. An estimate of the diffusion coefficient of the protons can be obtained by measuring the conductivity of the sample. At

30 Å

5 Å

33 nm

33 nm
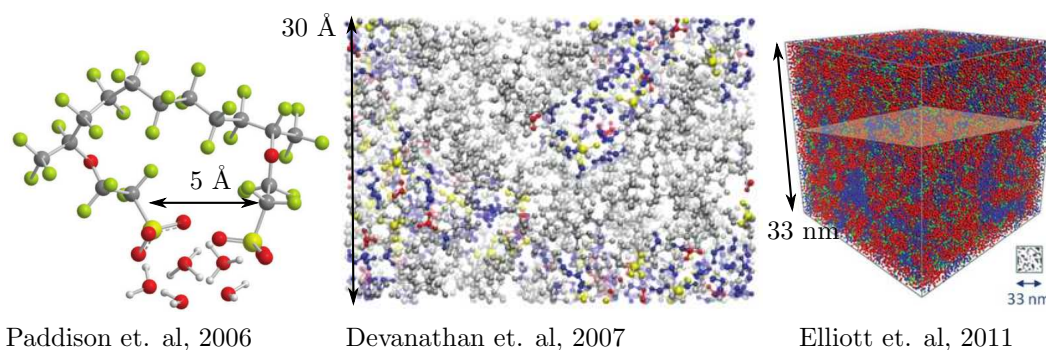
Paddison et. al, 2006   Devanathan et. al, 2007   Elliott et. al, 2011

Figure 3.6: Examples of simulation samples from the literature. Left: a structure optimised by *ab initio* simulation adapted from reference [86] where the bridge is observed. Centre: a sample of hydrated Nafion polymer simulated by all atom molecular dynamics. Water molecules, hydronium ions, sulfonate groups, fluoro-carbonate groups are shown in blue, red, yellow, and gray, respectively. Adapted from [87]. At this scale, the phase separation is visible, and the irregular character of the nanostructure is also apparent. Right: a sample of hydrated Nafion polymer simulated by the DPD mesoscale technique [88]. This technique allows the simulation of much larger samples (33 Å in this case), and the phase-separation between aqueous (blue) polymeric (red) domains is clearly visible. At this scale, no long-range order is apparent.

the micrometer scale, Pulsed Field Gradient Nuclear Magnetic Resonance (PFG-NMR) can be used to measure the self diffusion coefficient of water [106]. Quasi elastic neutron scattering is a powerful technique to study the motion of atoms on a wide range of time- and length-scales (of the order of 1 Å to 1 nm and 1 ps to 1 ns). It is well adapted to the study of water, and in particular to the study of water in PFSAs due to its high sensitivity to hydrogen, and high contrast between the protonated ionic domains and the unprotonated PFSA polymer matrix. The drawback of this approach is that the analysis of the experiment requires fitting a model of molecular motion to the dynamic structure factor. As a consequence, the conclusion drawn from the experiment completely depends on the model.

The typical approach to modelling transport in confinement is to start from the standard diffusion mechanism and to impose a boundary condition that appropriately reflects confinement [107]. One particularly successful approach in the case of confinement in irregular geometries is that of the transport in a Gaussian well. The displacement is drawn from a probability distribution of variance 2σ associated to the width of the well. From this hypothesis it is possible to derive expressions for the neutron scattering intensities that depend only on the characteristic confine-

ment size σ, and on the choice of a correlation function describing how a sample particle loses memory of its starting position [107]. The simplest correlation function is a decaying exponential with characteristic time τ. From the confinement size σ and the characteristic time τ, it is possible to compute an effective diffusion coefficient $D = \sigma^2/\tau$. Transport of protons in hydrated PFSAs can be modelled as a sum of two processes, each characterised by its own Gaussian confinement size and exponential correlation functions with different characteristic times [108]. These two processes can be associated to two populations of protons (see figure 3.7):

- the "fast" population is diffusive and grows linearly with the hydration. Its motion is composed of two processes: confined translational diffusion within domains of mean size 2σ corresponding to a few Ångstroms occurring on a time scale of roughly 10 ps; and long-range Fickian diffusion between neighbouring domains .

- the "slow" population is non-diffusive and consists of three protons per acid group independently of the hydration (figure 3.7 from reference [109]). The localised motions are interpreted as protons hopping from site to site and can be ascribed to a peculiar slow process involving protons strongly interacting with charged interfaces.

These two populations and their associated mechanisms are detailed in figure 3.7. Further studies on higher resolution spectrometers revealed that there are in fact at least three different regimes of proton motion, which were attributed to localised hopping of protons with a period of 100 ps, a fast (10 ps) diffusive motion on short distances (1Å), and Fickian diffusion a the nanoscale [110].

Numerical simulations provide a complementary approach to the study of transport in hydrated PFSAs. The mechanisms of hydration and transport of protons in perfluorosulfonic acid systems have been extensively studied in model structures by *ab initio* molecular dynamics simulations of crystalline perfluorosulfonic acid hydrates [111, 86, 112, 113], and carbon nanotubes decorated with sulfonic groups [50]. In these systems, hydration levels as low as one water molecule per acid group were demonstrated to be sufficient to dissociate the protons from the acid. The excess protons are most likely to form Eigen and Zundel ions. At very low hydration ($\lambda < 5$, *i.e.* less than five water molecules per acid group), the hydrogen bond network does not extend past the two or three nearest neighbours, and dissociated protons are essentially trapped by acid groups [112]. At $\lambda = 5$, the hydrogen bond network of water molecules is significantly more extended, and some molecules' hydration shells consist only of other water molecules. The excess proton was found to delocalise preferentially on these "hydrated" water molecules. However, long range transport of protons was not observed in these systems [113]. Another approach
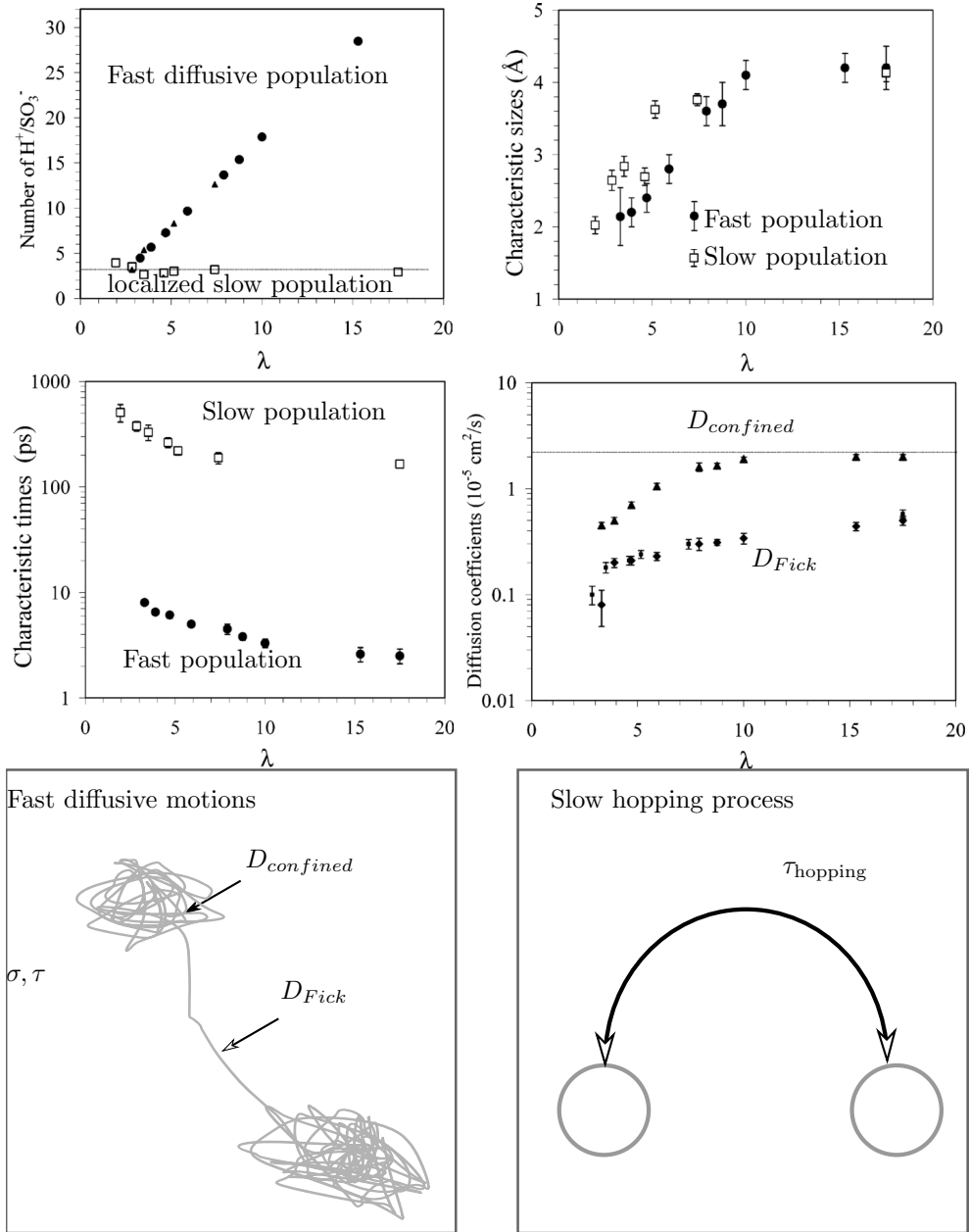
Figure 3.7: Parameters extracted from the data using the Gaussian model. Two populations of protons (top left), with their associated confinement sizes (top right), characteristic times (bottom left) and diffusion coefficients (bottom right), as obtained from the analysis of QENS data with the Gaussian model [108]. The motion of the fast diffusive population is a combination of motion confined in droplets of average extension 2σ on a time scale τ with long-range diffusive motions with diffusion coefficient D_{Fick} (see bottom left). From the size and time-scale of the confined motion, one can compute an effective diffusion coefficient $D_{confined}$. The motion of the slow population is attributed to a slow hopping process, on a characteristic length- and time-scales $\sigma_{hopping}$ and $\tau_{hopping}$ respectively.
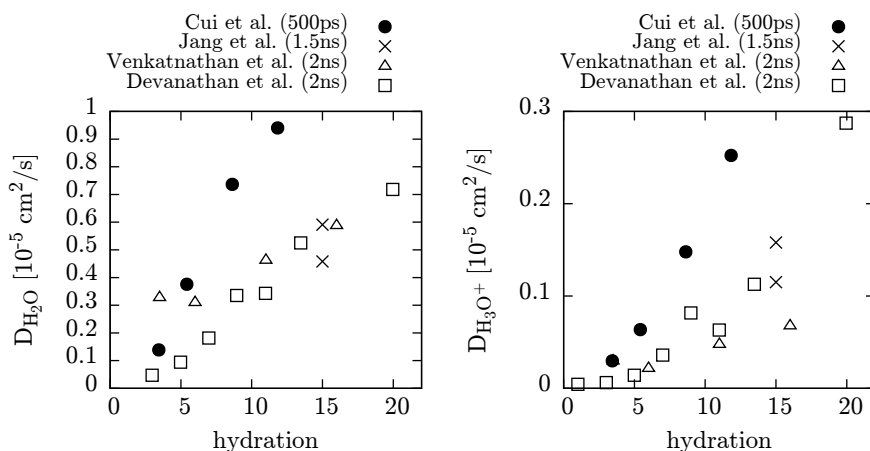
Figure 3.8: The diffusion coefficient of water (left) and hydronium ions (right), as measured by several studies [99, 87, 117, 118]. The time-scale at which these values was measured is reported in the legend.

to the mechanisms of dissociation of protons and to the hydrogen bond network in confined sulfonic environments consists in grafting sulfonic acid groups in carbon nanotubes of various diameter [50]. Varying the density of acid groups allows to fine-tune the respective strength of hydrophobic and hydrophilic interactions with respect to the confinement effects. Increasing the density of sulfonic acid groups increase the likelihood of protons dissociating as well as the connectivity of the hydrogen bond network. These *ab inito* studies provide key insights in the proton dissociation mechanisms, as well as criteria for the presence of hydrogen bonds, yet they lack the details of the flexibility of the real material.

Grotthuss shuttling has been observed in PFSAs in several independent studies [95, 114]. Contrary to the case of bulk water where the Grotthuss mechanism significantly enhances the mobility of protons, structural shuttling of protons in PFSAs was found to work against the vehicular transport, resulting in an overall slower transport [114].

Empirical valence bond model molecular dynamics was also used to study proton transport in model systems [115] as well as hydrated PFSAs [116]. While these techniques struggle to be quantitatively close to experimental results, they highlight the importance of hydration and of the motion of sulfonic acid groups for proton transport.

In figure 3.8, we have compiled the vehicular diffusion coefficients, as obtained in a few studies [99, 87, 117, 118]. The overall increase of the diffusion coefficient with hydration (as seen experimentally, figure 3.7) is captured by simulations. However,

while all these studies qualitatively agree on this feature, we remark large variations
from one study to another. To the best of our knowledge, these variations are too
large to be attributed to differences in the water models among studies. Vehicular
transport of protons (or other cations, for instance in [98]) is qualitatively similar
to that of water, with the vehicular diffusion coefficient of hydronium ions being
two to ten times smaller than that of water at the same hydration level (see refs.
[99, 87, 117, 118] and figure 3.8). This is sometimes attributed to size effects,
where hydronium ion move together with their first hydration layer [117], or to
the longer trapping times of hydronium complexes in the hydration shell of sulfonic
acid groups, due to electrostatic interactions [118].

At this point, two considerations are in order. First, it is perhaps surprising
that transport in simulations of PFSAs has always been reported as being Fickian,
especially in light of our discussion of the effect of confinement on transport in the
previous chapter. Indeed, all the ingredients for sub-diffusion seem to be present:
strong confinement and long trapping times of water and protons at the hydrophilic
interface. Interestingly we remark that in all these studies, diffusion coefficients
are obtained from linear fits of the mean squared displacements, but that no study
discusses the linear (or non-linear) character of the mean squared displacement in
time, especially at low hydration levels. Moreover, the presented mean squared dis-
placements span different time-scales in different simulations: while some studies
compute it on a 1.5 ns [99] or 2 ns [87, 118] interval, the other has considered a con-
siderably shorter time-scale of 500 ps [117]. It is interesting to note that the latter
study obtained significantly larger values of the diffusion coefficient. This depen-
dence of the diffusion coefficient on the time scale at which it is probed could also
be a sign of the possible sub-diffusive behaviour of water in these systems. Much
more careful measurements should be performed to assess the nature of the trans-
port process, as the difference between the diffusive and sub-diffusive interpretation
of data can lead to substantially different conclusions, as we will see at length in
chapter 6.

The second observation is that that studying any property of hydrated PFSAs
is significantly complicated by the irregularity of the structure of these materials.
In the next chapter, we review a complementary approach to those presented here
that aims at studying the structure and transport properties of water and ions
confined in materials of similar physico-chemical properties, but whose structure is
well defined and easier to control.

3.3   Ionic surfactants as model system

At the end of the previous section, we concluded that due to the intrinsically dis-
ordered nature of hydrated PFSAs polymers it is very hard to establish a clear

$$CF_3 \diagup \overset{CF_2}{} \diagdown CF_2 \diagup \overset{CF_2}{} \diagdown CF_2 \diagup \overset{CF_2}{} \diagdown CF_2 \diagup \overset{S^{+1.1}}{} \diagdown O_3^{-2.1}$$
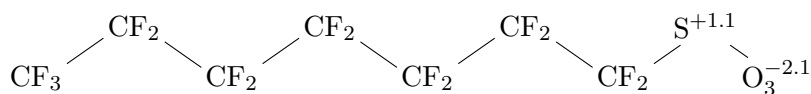
Figure 3.9: Chemical structure of the PFOS surfactant, an excellent model of soft confining matrix [110, 119].
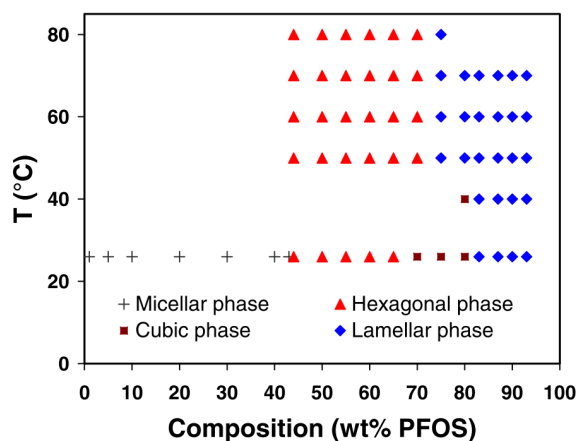
Figure 3.10: Phase diagram the PFOS surfactant, as determined experimentally [120].

relationship between structural and transport properties in these systems. For that reason, alternative approaches have been developed. For instance *ab initio* studies of crystalline perfluorosulfonic acid hydrates [111, 112, 113], and carbon nanotubes decorated with sulfonic groups [50] were reported, as reviewed in the previous section.

In this section, we introduce a different approach and the insight that can be gained in terms of structure-transport interplay. Perfluorosulfonic acid surfactants like the perfluorooctane sulfonic acid (PFOS, see figure 3.9) are chemically similar to PFSA polymers, yet they present the significant advantage over polymeric materials that they self-assemble in extremely neat phases [120]. In figure 3.10 we show the phase diagram of PFOS-water mixtures in various surfactant concentration and temperature conditions.

These molecule present the advantage of being super acidic, which ensures the dissociation of the acid group at hydrations as low as one water molecule per surfactant.[3] From a modelling point of view, this simplifies the treatment of the acid

---

[3]This dissociation of acid groups at ultra-low water contents has also been observed by infrared spectroscopy in the Nafion membrane [121].

group that can safely be assumed to be dissociated at any hydration level. We now review some of the work on the structure and transport properties of hydrated ionic surfactants.

3.3.1 Structure of hydrated ionic surfactants assemblies

As we just saw, the head of the surfactants is highly hydrophilic due to its strong acidity. Moreover the fluorocarbon tail is highly hydrophobic. These properties result in a strong amphiphilic character, which leads to extremely neat phase separation upon hydration. In comparison with ionomers, surfactants lack the polymer backbone. This removes mechanical constraints and therefore reduces the tortuosity and disorder of the self-assembled structures.

The structure of the resulting self-assembled system can be tuned by varying the degree of hydration: this allows for adjustable confinement sizes and geometries. These systems have been characterised experimentally, and have been shown to be an excellent choice of model systems [120, 110, 119]. The phase diagram of these systems has been characterised by X-ray scattering (see figure 3.10). In particular, the dynamics in hydrated PFSA membranes and surfactants are very similar in terms of confinement size and diffusion coefficients at the local and micrometer length scales [119].

A model approach was adopted for a molecular dynamics study of the side-chains of several PFSAs polymers in order to elucidate the effect of side chain geometries on the diffusion coefficient [101]. [4] Interestingly, seemingly drastic differences in the morphology of the surfactants induce only mild variations in the value of the diffusion coefficients.

While no other study has been reported that deals specifically with perfluorosulfonic acid surfactants, multiple simulations studies have been published on the simulation of surfactants, which we briefly review here. At this point it is interesting to note that only few studies have been published that deal with ionic surfactants, while a much larger body of work is available concerning the non-ionic surfactants. A wide array of techniques have been developed to study the self assembly of surfactants. The idea is to approach the correct potential energy surface at the considered temperature. One of the earliest attempts employed a Monte Carlo scheme to sample the configuration space on a lattice whose vertices can be occupied by either water, a surfactant head, or part of a surfactant tail [125, 122]. In figure 3.11 (a) we show example lamellar structures generated with this technique. Monte Carlo

---

[4]We note that Ref. [101] contains an extremely detailed all-atoms simulation study of the side chain pendants of three perfluorosulfonic acid polymer electrolyte membranes, characterised by different structures. Structural organisation was investigated in details, together with some transport properties, at different degrees of hydration. Interestingly, the Authors completely overlooked the possibility to comment on similarities with ionic surfactant phases.
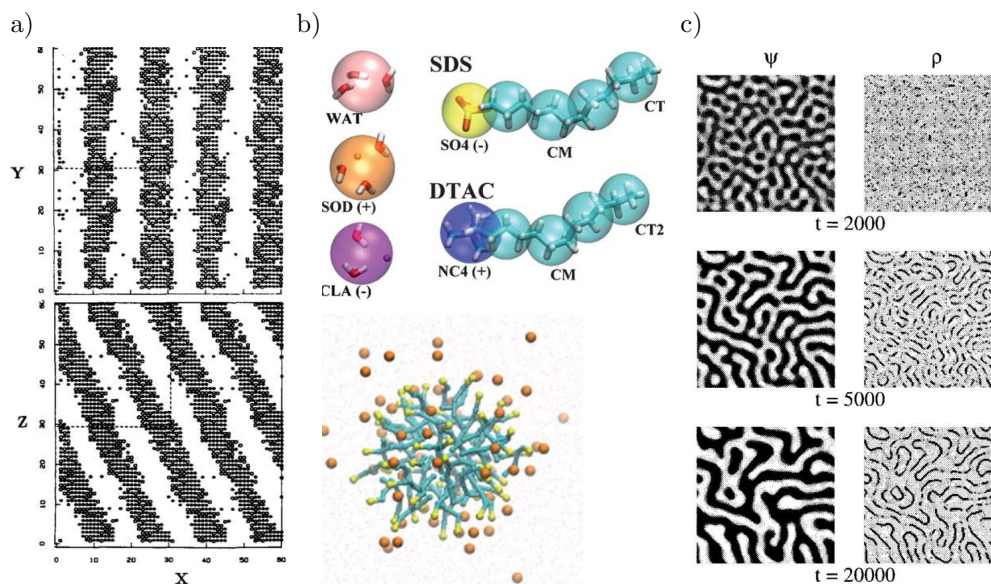
Figure 3.11: Different coarse-graining strategies from the literature. **a)** Space is discretised on a grid. Each node of the grid can be occupied by water (white), surfactant tail (full circle) or head (hollow circle). Sampling of the conformational space is achieved by Monte-Carlo. Adapted from [122]. **b)** Atoms are grouped together in a *united atoms* representation. Here, a water bead represents three water molecules, and ions are merged in larger beads along with two or three water molecules. The sampling is done by molecular dynamics. Adapted from [123]. **c)** Space is occupied by two scalar fields) ρ is the difference between the densities of water and oil and Φ is the density of surfactant. The equilibration is driven by the Landau-Ginzburg theory. Adapted from [124]

simulations can also be implemented in an off-lattice fashion. Such technique has been employed to study the formation of ionic surfactant micelles and the interaction between several micelles [126]. While this allows for very efficient convergence to the correct statistical ensemble, this technique provides no information on the dynamics of the system.

Molecular dynamics simulations can be used to generate coherent trajectories, and have been employed to study the self-assembly of surfactant-oil-water systems [127], surfactant in an implicit Langevin fluid [128], aqueous solutions of non-ionic [129] and ionic surfactants [130, 131, 123], and mixtures of oppositely charged ionic surfactants [132]. In figure 3.11, we show the coarse-graining scheme employed in reference [123]. This study is characteristic of all coarse-grained studies on surfactants because water and ions are also coarse grained. Fluid "beads" represent three

water molecules or three water molecules and one ion. It is clear that such study lacks the resolution to discuss the transport of water and ions in details. Most of those studies deal with the micelisation of the surfactants at high water content, but some reported results on the whole phase diagram [122, 129] and the work of [131] and [133] focus on the dynamics of water in reverse surfactant micelles. Some special cases have been considered, for instance the presence of a Langmuir mono-layer or carbon nanotubes [123]. These studies demonstrated that a satisfactory phase diagram can be obtained from extremely simple models that completely omit all chemical details (for instance [125, 122]), and that both the translational and rotational dynamics of the fluid in these assemblies is always slower than in the bulk (for instance [131] and [133]).

Mesoscale approaches are also well suited to the study of mixtures of surfactants. One such approach is based on the Landau-Ginzburg theory [134], whose principle is to minimise the free energy functional as a function of the local difference of concentration between the different species in the mixture. It has for example been used to study the structure and dynamics of water-oil-surfactant mixtures [124, 135]. In figure 3.11 we show some samples that have been generated using this technique. Again, such extreme coarse-graining leads to correct predictions of the phase diagram, however in these cases it is not possible to measure dynamical properties. Other approaches are possible which involve the coarse graining of the fluid, such as Lattice-Boltzmann [136], Multiparticle Collision Dynamics [137], or Dissipative Particle Dynamics [138, 139, 140].

3.3.2   Positioning our work with respect to the literature

As can be seen from this non-exhaustive, yet representative review, most studies adopt the point of view of the surfactants, and while they successfully describe the phase diagram in various conditions, they do not provide details on the structural or transport properties of the fluid. Moreover, most of the efforts are directed toward the structure of specific regions of the phase diagram, and few study deal with the dynamic properties of the assembled systems [131, 62]. In most cases, such detail is not even accessible as the degrees of freedom of the fluid are integrated out by the coarse-graining process. Therefore, while PFSA membranes and surfactants have been abundantly studied, we are convinced that there is room for a new physics-based model that reproduces the important features of the ionic surfactants and allows detailed study of the properties of water confined in the surfactant aggregates.

Part II

Results and discussion

Chapter 4

The model

Our idea is to couple a minimalist coarse-grained model of surfactants with a well behaved atomistic model of water. The interest of this approach is multifaceted: on one hand it allows us to study the particular case of perfluorinated surfactants; on the other hand it is also a generic playground to tackle the problem of water confined in soft environments, of varying degrees of confinement. Additionally, it is also possible to graft such surfactants on a polymer backbone, therefore forming a model of PFSA. In short, we developed a unified framework to study water in model soft environments, and in PFSA membranes as well as model surfactants phases. In the following part of this chapter, we introduce our implementation of such a model, as well as the advances in the understanding of these systems.

4.1   Molecular Dynamics

The basic idea of Molecular Dynamics (MD) is incredibly simple: to solve Newton's equations of motion for a set of interacting particles. In figure 4.1, we give a schematic overview of the MD technique. The user has to define the model of the system. This involves choosing the type of interactions (force-field), and the associated properties of the particles and topological details of the molecules. On the figure, the modelling aspect is highlighted in blue. The user also has to specify the statistical ensemble. For example, one may chose to consider constant temperature, pressure and particle number (NPT ensemble), or constant energy, volume and particle number (NVE ensemble). On the figure, the aspect related to the choice of the conditions of the simulation is highlighted in green. Given such parameters, simulation packages such as LAMMPS are able to iteratively solve the equations of motion to produce a trajectory of the system.

Each atom or coarse grained unit is represented by a Lennard-Jones bead, to which is associated a position and a velocity. The output of the simulation is a set
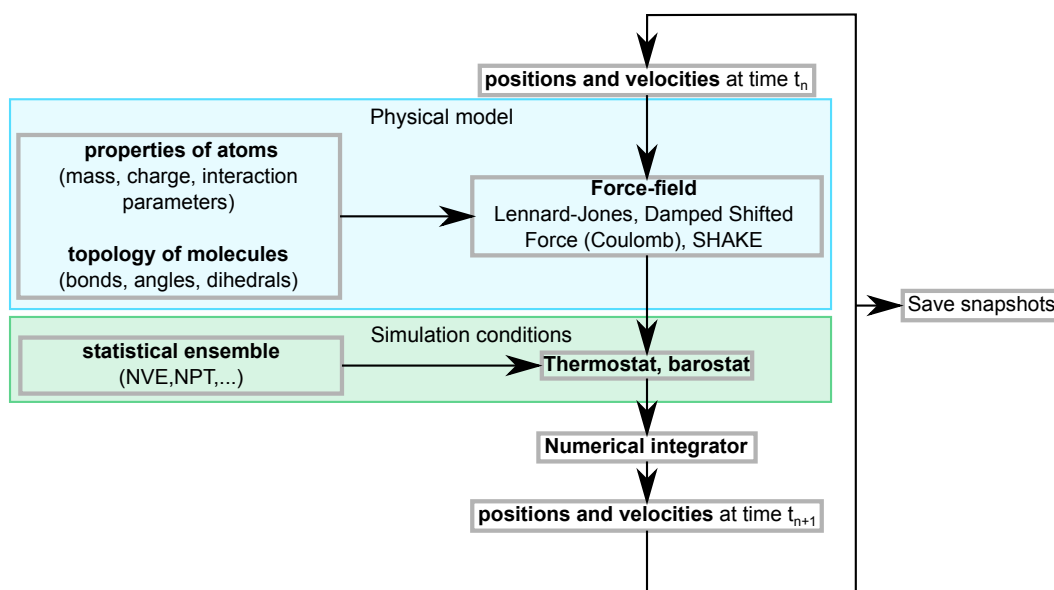
Figure 4.1: Schematic representation of the molecular dynamics technique. The user has to define the model of the system. This involves choosing the type of interactions (force-field), and the associated properties of the particles and topological details of the molecules. Here, the modelling aspect is highlighted in blue. The user also has to specify the statistical ensemble. For example, one may chose to consider constant temperature, pressure and particle number (NPT ensemble), or constant energy, volume and particle number (NVE ensemble). Here, the aspect related to the choice of the conditions of the simulation is highlighted in green. Given such parameters, simulation packages such as LAMMPS are able to iterative solve the equations of motion to produce a trajectory of the system.

of snapshots that contain the values of the position and velocity of each atom in the system, at various points in time on the trajectory.

In the case of molecules, bonds are modelled by harmonic restraints. The forces acting on each particle are defined in the so-called *force-field*, and is used by the numerical integrator to solve the equations of motion.

In the case of water and hydronium molecules, the characteristic frequency of the harmonic restrains is very high, therefore integrating the equation of motion for such systems would require very small time steps. Instead, the geometry of these molecules is enforced by the SHAKE algorithm, a Lagrangian technique that was developed to perform simulations of molecules with high frequency bond vibrations using a large time step [141].

4.1.1 The issue of long-ranged interactions

Given the potentially large number of interaction sites in our simulation, computing the forces exerted on each site in an exact manner is prohibitively expensive. Several approaches to increasing the efficiency can be implemented, and here we describe ours. The classic reasoning in software optimisation is that one should pick the low hanging fruits first, and then work his way up in the tree. In the case of molecular dynamics, pairwise interactions are the larger effect, because if treated exactly by computing all the terms they scale as $O(N^2)$, where N is the number of interaction sites. Interactions that are short ranged, like Lennard-Jones for instance, can safely be truncated. However, longer ranged r^{-1} interactions, like the electrostatic forces should be treated a bit more carefully, as simply truncating them could lead to potentially large errors on the final value of the potential and of the force [142]. This problem arises when the charge contained in the cutoff sphere is non-zero. Several techniques have been developed to remedy this problem.

Particle mesh techniques make use of the efficient implementation of the discrete Fourier transform to solve the Poisson equation for the interaction potential *via* the convolution theorem [143]. The complexity of the computation is then reduced to $O(N \log N)$, where N is now the number of cells used to discretise the space. In addition, this technique automatically takes into account the interaction of the simulation box with its periodic images.

Alternative truncation techniques have since been developed, for instance the Wolf shifted force and potential methods [144] or the damped shifted force (DSF) [145], that work by truncating the force such that the resulting force is continuous, even at the cutoff distance, and restore the neutrality of the cutoff sphere. This class of technique has been proven to be robust [145], and in particular it was recently shown that the properties of water are well captured [146]. While these truncation techniques have been shown to give wrong density profiles in confinement when a short cutoff is used [147], using a cutoff distance of 9Å and larger yields excellent agreement with particle mesh calculations even in confinement, as shown in [148].

We therefore decided to use the shifted force method of computing the electrostatic interaction and a 12 Å cutoff (equation 4.2), which is achieved in LAMMPS by using the `dsf` pair potential (equation 4.1) with a damping constant set to zero.

$$F_{\text{DSF}}(r) = q_i q_j \left[\left(\frac{\text{erfc}(\alpha r)}{r^2} + \frac{2\alpha}{\sqrt{\pi}} \frac{\exp(-\alpha^2 r^2)}{r} \right) \right.$$
$$\left. - \left(\frac{\text{erfc}(\alpha R_c)}{R_c^2} + \frac{2\alpha}{\sqrt{\pi}} \frac{\exp(-\alpha^2 R_c^2)}{R_c} \right) \right] \theta(r - R_c), \qquad (4.1)$$

$$F_{\text{DSF0}}(r) = q_i q_j \left(\frac{1}{r^2} - \frac{1}{R_c^2} \right) \theta(r - R_c^2), \qquad (4.2)$$

Where q_β is the charge of bead β, α is the damping constant (set to zero in the DSF0 force field), R_c is the cutoff and θ is the Heaviside function.

As can be seen, while the underlying principle of molecular dynamics is very simple, the implementation is not trivial, especially if efficiency is critical. For this reason, we use LAMMPS, one of the major open implementations of Molecular Dynamics [149]. This tool makes setting up the simulation components (force field, integrator, thermostat and barostat, etc...) trivially easy.

This allows us to dedicate most of our efforts to setting up the simulation in a way that is physically correct, which as we will see is not always obvious. For that reason, it is worth taking some time to simulate a simple system of bulk water. We duplicated LAMMPS's code for the dsf potential and hard coded the damping constant to zero (which simplifies equation 4.1 to equation 4.2), which resulted in a $1.6\times$ speedup in simple bulk water systems compared to the original implementation.

4.2   Water and hydronium models

As we have seen in chapter 2, developing a model of water is highly non trivial, and is beyond the scope of this thesis. Multiple models are available [28, 29, 30], and their properties are well known, both in the bulk and in various types of confinements. While the numerical values of the interesting observables may differ [31], all these models are able to access physical quantities that are relevant for us: they feature realistic water structure (both in terms of pair correlation functions and in terms of hydrogen bond statistics), polarisability, and their transport properties are reasonably realistic. We chose to use the SPC/E model of water [30]. This water model has been demonstrated to provide realistic results in the bulk at ambient conditions [31, 37] and in the supercooled region of the phase diagram [150, 14, 37], as well as in confinement [151, 148, 152, 153, 154]. We expect that choosing a different model would not have yielded significant differences, and that we would have been able to reach the same conclusions.

In the following we detail our implementation of the SPC/E model of water. The topology and interactions are as in reference [30]. The SPC/E molecule consists of three interaction sites which correspond to the oxygen (O) and hydrogen (H) atoms. The distance between the O and H atoms is set to $r_{\mathrm{OH}} = 1$Å, and the $\widehat{\mathrm{HOH}}$ angle is set to $109.47°$. Each interaction site carries an electric charge, and the O sites interact via a 6–12 Lennard-Jones potential of strength $\epsilon_{\mathrm{OO}} = 0.1554$kcal/mol and characteristic distance $\sigma_{\mathrm{OO}} = 3.166$Å. Hydronium ions can be modelled in a similar way, and we chose the model of Kusaka et. al [155]. The parameters of the models are summarised in table 4.1.

We checked that the pair correlation function, mean squared displacement and

	Water	Hydronium
r_{OH} [Å]	1	0.973
$\widehat{\mathrm{HOH}}$ [°]	109.47	111.6
q_{O} [e]	-0.8476	-0.248
q_{H} [e]	$+0.4238$	0.416
m_{O} [g/mol]	15.9994	15.9994
m_{H} [g/mol]	1.008	1.008
σ_{OO} [Å]	3.1655	2.9
ϵ_{OO} [kcal/mol]	0.1554	0.2740

Table 4.1: Summary of the values of each parameter of the models of water molecules and hydronium. For comparison, other models of water are shown in table 2.1
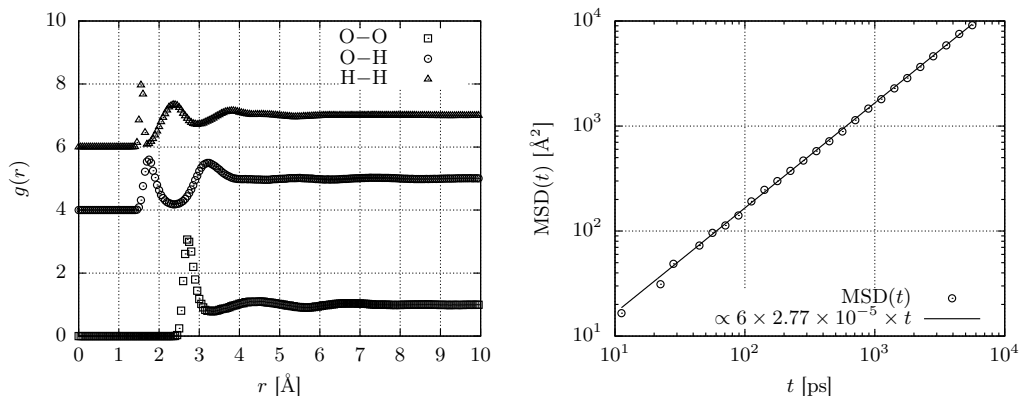
Figure 4.2: Left: Pair correlation functions measured at 300 K/1 Atm on our test simulation of SPC/E water using the DSF Coulombic interaction with our hard-coded setting of the damping parameter to zero. The O–H and H–H datasets have been shifted by 4 and 6 respectively for clarity. Right: Mean square displacement measured on a 10 ns production run on the same water model in the same conditions. The continuous line represent a least square fit of the MSD with the Einstein relation for the diffusion coefficient. We obtain a value of $D = 2.77 \cdot 10^{-5}\,\mathrm{cm^2/\,s}$, in good agreement with published results [31].

diffusion coefficient of a test system of 1000 water molecules at 300 K and 1 Atm are realistic. The results are shown in figure 4.2, and are in good agreement with the literature, for instance [31]. We have also computed that on average, water molecules form 3.64 hydrogen bonds with their neighbours, which is well within published values [32, 33].

4.3   Surfactant model

In this section we detail the main features of the model for the surfactants we have developed. This model has been published in [156]. We have devised the simplest model that allows us to study the surfactant solution at the relevant length scales, grasping both the details of the nano-structure of water domains (1-15 Å) and the macroscopic ordering of surfactant aggregates (20-100 Å). We provide a united atom description of the molecule, where the details of structure and chemical composition of the surfactant molecules are integrated out, while uniquely keeping the crucial molecular features driving the physics of the system. Our model is a modified version of the model of the side chain of Nafion published in [103, 105]. This is essentially a simplified version of the side chain presented in [157], with the electric charge of the hydrophobic tail being set to zero. This simplification was shown not to affect the structure of the self-assembled polymer [105].

Without going into the details of the chemical structure, an ionic surfactants solution can be seen as a three-components mixture: the surfactant macro-molecules (Su), the polar solvent (water, W), and the solvated (counter-)ions (hydronium, H). The physics of the material is controlled by the interplay of two quantities: *i)* the energy of the interfaces formed between the amphiphilic aggregates and the fluid phase, and *ii)* the electrostatic interactions among the charged hydrophilic heads and the solvated cations. The idea of this model is to represent, with a minimum of interactions sites, the essential attribute of the real system: the amphiphilic behaviour, with the polar head and the hydrophobic tail, and the charge as well as the polarity of the head. The topology of our model is shown in figure 4.3: the surfactant
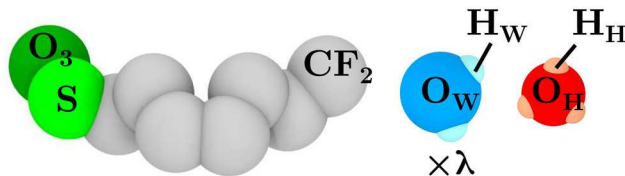

Figure 4.3: Schematic representation of the model of surfactants that we studied. Each bead is a coarse grained version of the units visible in figure 3.9

Atom type	Mass [g·mol^{-1}]	Charge [e]	Neutron scattering length b_α [fm]
CF$_2$	50.0	0	17.954
S	32.0	1.1	2.847
O$_3$	48.0	-2.1	17.409
O$_W$	15.99940	-0.8476	5.803
H$_W$	1.0080	0.4238	-3.7390
O$_H$	15.99940	-0.2480	5.803
H$_H$	1.0080	0.4160	-3.7390

Table 4.2: Mass and charge of each atom type in our model. The neutron scattering lengths are used as weighing factors in the computation of the neutron static structure factor. The 'W' and 'H' subscripts correspond to atoms pertaining to water and hydronium, respectively.

consists of a chain of hydrophobic CF$_2$ beads, terminated by a polar S$^{+1,1}$O$^{-2,1}$ group. The charges on the head group ensure polarity with a realistic value of the dipole [103], and the tail is made hydrophobic by truncating the Lennard-Jones interaction between the tail beads and the fluid beads at the minimum, keeping only the short range repulsive part. Following experimental evidence [109], we assume that the excess protons form hydronium complexes, which we implement according to the model presented in section 4.2 and reference [155].

Beads pertaining to different molecules, or located in the same molecule and separated by more than three bonds, interact with the sum of Lennard Jones (LJ) and Coulombic interactions. The water molecules are represented by the SPC/E model [30], see section 4.2.

Starting from the model described in [105], we tuned the relative weights of these two terms, to stabilise the attended phases at different water contents. To this end, we performed a large number of simulations at a wide range of hydration, where we successively adjusted the strength of the interactions until we obtained a phase diagram that is close to the experimental one. We give the details of the optimised model in tables 4.2, 4.3, and 4.4. We remark the extremely strong amphiphilic character of the surfactant molecules: the depth of the potential for both the hydrophilic (S- and O$_3$-O$_{W,H}$) and hydrophobic (CF$_2$-O$_{W,H}$) interactions is more than twice that of the O$_W$-O$_W$ potential.

4.3.1 Simulation details

The protocol for the simulation of surfactant-water mixtures is mostly similar to that for simulations of bulk water (section 4.1). However, there are a few differences which we discuss here. We initialised the different systems by placing

α	β	$\epsilon_{\alpha\beta}$ [kcal/mol]	$\sigma_{\alpha\beta}$ [Å]	$r_{c,\alpha,\beta}$ [Å]
CF_2	CF_2	0.20	3.93	11.79
CF_2	S	0.05	3.93	11.79
CF_2	O_3	0.05	3.93	11.79
CF_2	$O_{W,H}$	0.40	3.93	4.41
S	S	0.15	3.93	11.79
S	O_3	0.15	3.93	11.79
S	$O_{W,H}$	0.40	3.93	11.79
O_3	O_3	0.15	3.93	11.79
O_3	$O_{W,H}$	0.40	3.93	11.79
O_W	O_W	0.1554	3.1655	9.50
O_H	O_H	0.2740	2.9	8.70
$H_{W,H}$	*	0.0	0.0	0.00

Table 4.3: Lennard-Jones interaction parameters for all atom types in the model. '*' denotes all possible atoms and subscripts. Interactions not specified in this table are deduced using the arithmetic mixing rule [149]: $\epsilon_{ij} = \sqrt{\epsilon_i \epsilon_j}$, and $\sigma_{ij} = (\sigma_i + \sigma_j)/2$.

all molecules in the simulation box, with random positions of the centres of mass and orientations. This allows to avoid introducing any initial preferred order, subsequently letting the system self-organise in the most stable configuration, simply based on the interplay among the interaction forces. Initial overlaps were removed by shortly integrating the equations of motion in the NVE ensemble, with the constraint that the displacement of each atom at each time step could not exceed 1 Å. Next, we coupled the box to a $P = 1$ atm Berendsen barostat [158] and thermostat, slowly cooling the system from an initial temperature of 350 K to the target temperature $T = 300$ K. In figure 4.4, we show an example of the time-evolution of a system during a five nanoseconds equilibration run. This clearly demonstrates the progressive ordering of the phases toward a well defined lamellar structure. The time step used for the numerical integration of the equation of motions, in this final part of thermalisation and for production runs, was $\delta t = 1$ fs. Extremely extended thermalisation runs followed, generated according to the NPT ensemble via Nosé-Hoover schemes [158], to allow self-assembly in completely relaxed stable structures. In the case of the lamellar phases at low hydration levels, the studied time scales were so extended that we observed a peculiar form of the 'flying ice cube' issue (see figure 4.5 and reference [159]). In this case, the energy of high frequency modes was transferred to the centres of mass of two sub-systems, formed by the absorbed fluid and the surfactant domains, respectively. Next, due to the conservation of *total* momentum, the two subsystems moved ballistically in oppo-

| Molecule | Bonds: $k_B(r - r_0)^2$ | | |
	k_B [kcal/mole/Å^2]	r_0 [Å]	
Su	350.0	1.540	
W	450.0	1.0	
H	450.0	0.973	
	Angles: $k_A(\theta - \theta_0)^2$		
	k_A [kcal/mole/degree^2]	θ_0 [degree]	
Su	60.0	110.0	
W	55.0	109.47	
H	55.0	111.6	
	Dihedrals: $k_D[1 + d\cos(n\phi)]$		
	k_D [kcal/mole/degree^2]	d	n
Su	3.1	-1	3

Table 4.4: Parameters for the intramolecular potential.

site directions, parallel to the planes of the lamellae. We used several techniques to cure this issue: periodically re-sampling the velocities of all atoms from the adequate Maxwell-Boltzmann distribution, and increasing the time-constant of the Nose-Hoover schemes for the cases when re-sampling the velocities is inconvenient (anytime we measured a time-dependant quantity). Following the thermalisation step, we performed the production runs, dumping complete system configurations (snapshots) at regular time intervals for subsequent analysis.

In the next chapter, we present our results on the structural properties of the resulting self-assembled configurations.
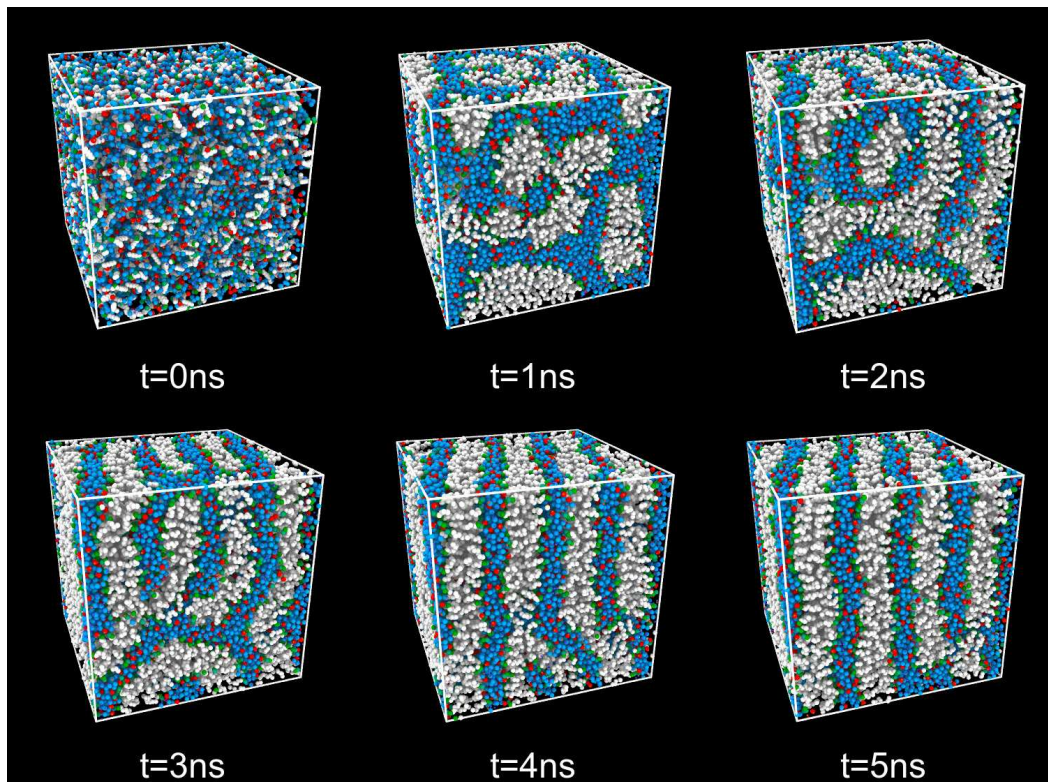
Figure 4.4: Time-evolution of a sample system ($\lambda = 4$) during the equilibration procedure. This figure illustrates the progressive ordering of phases with time.
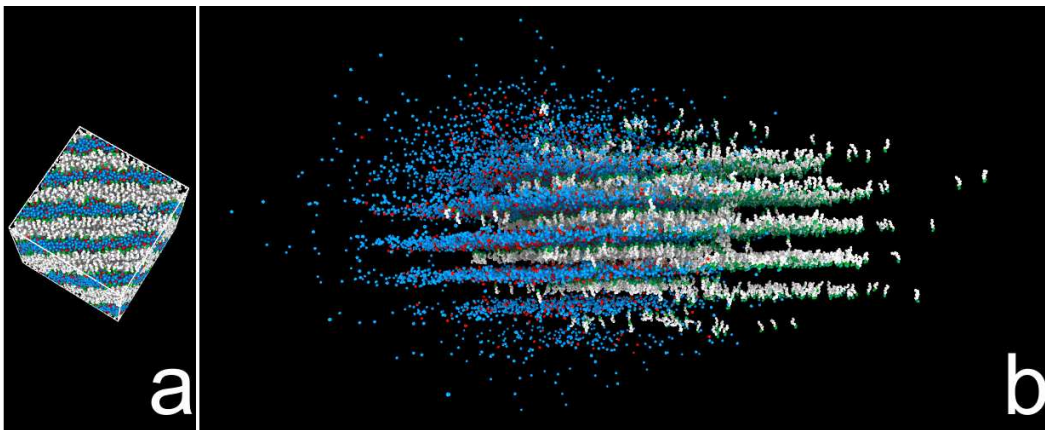
Figure 4.5: The subtle variation of the flying ice cube that we encountered in our biphasic system is hidden when observed using the periodic boundary conditions (a), but is obvious when removing the periodic boundary condition (b): the aqueous phase and the surfactant phase move ballistically in opposite directions, parallel to the planes of the lamellae.

Chapter 5

Structure properties of ionic surfactant-water mixtures

In this section, we discuss the structural properties of the self-assembled nano-structures that we obtained following the method in the previous sections. In the following, we characterise the phase diagram and quantitatively study the structure of the system in terms of diffraction patterns and static structure factors, both total and partial, as determined in neutron scattering experiments. Next, we describe the spatial arrangements of the separated phases in terms of the sizes of the ionic domains and quantify the wetting behaviour of the adsorbed fluid at the interface with the surfactants. This implies an investigation of the structure of the first coordination shell of the confined water molecules, and a study of the water coordination number at different distances from the boundaries of the ionic domains.

We stress here that the structures produced are the result of a very efficient *unbiased* self-assembly, starting from completely disordered system configurations. Note that the mobility of the surfactant macro-molecules lifts the need for an additional average over multiple realisations of the confining matrix. We verified in a few cases, however, that equivalent results are found when preparing the system in different initial conditions. The initial seed of the final phase formed quite quickly, on time-scales of the order of a few nanoseconds, followed by a slow relaxation to locally optimise mechanical stress. The phase diagram of our model conforms to that of concentrated amphiphile solutions discussed in many textbooks [160]. In figure 5.1 we show typical snapshots of the system at decreasing hydration levels. Starting from the highly hydrated systems ($\lambda \geq 16$), we found a micellar solution, with aggregates of different sizes and elongations, concentrating the hydrophobic beads at the centre and exposing the sulfonate groups to water. By increasing surfactants concentration ($12 < \lambda < 16$) repulsion between aggregates becomes
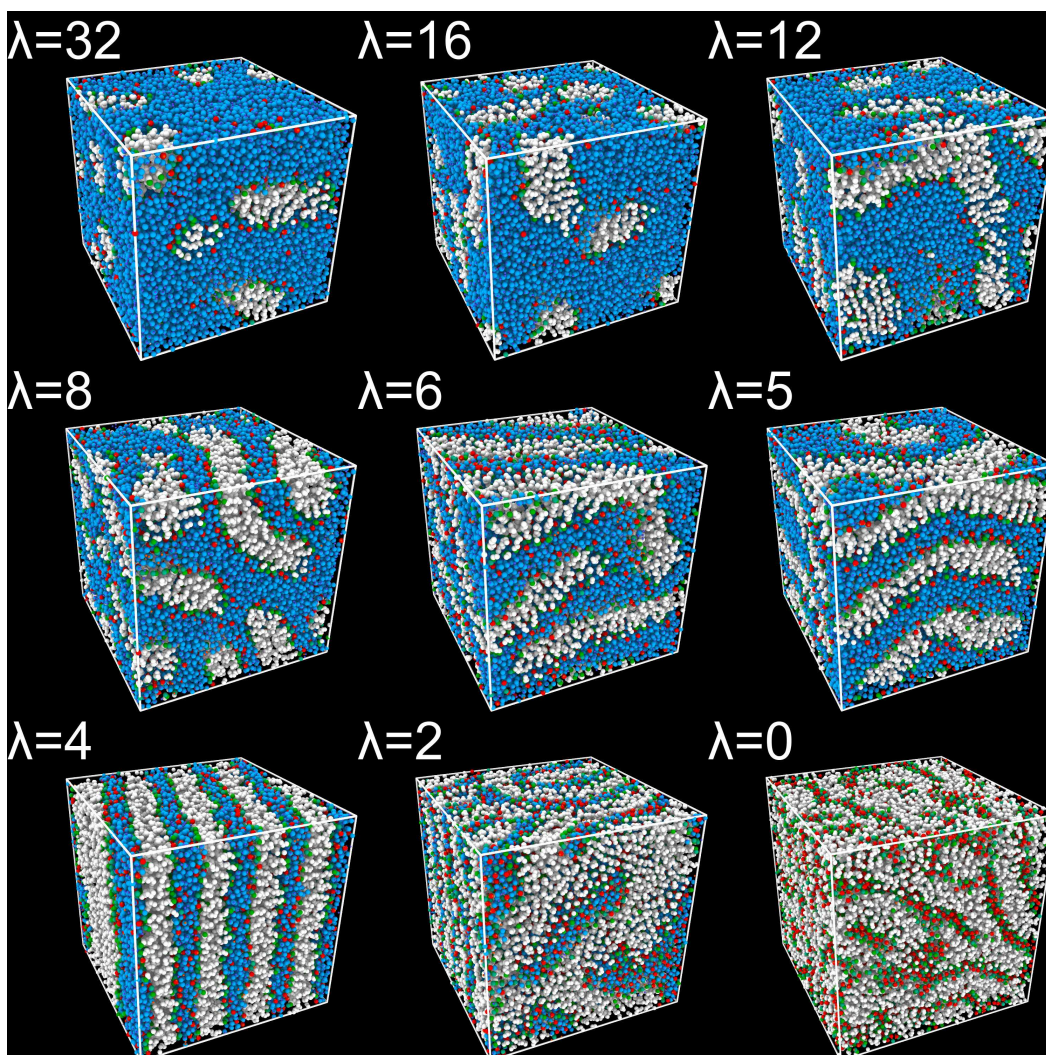
Figure 5.1: Snapshots generated from simulation data for decreasing water contents. The different features of the phase diagram are clearly visible and are discussed in the text.

significant, and micelles start to show an increasingly elongated character. This is due to the fact that, at high density, cylinders pack in space more efficiently than spheres. This process controls the transition for $8 \leq \lambda \leq 12$ to a cylindrical structure with some degree of closed-packed order, although it does not express as a fully developed hexagonal phase. In the intermediate range, $6 \leq \lambda < 8$, cylindrical aggregates merge and start to transform in flat bilayers. Eventually, for $\lambda \leq 4$,

surfactants arrange in extremely well-ordered lamellar phases, spanning the entire simulation box, with increasingly thin ionic channels intercalating the lamellae (see discussion below). In the case $\lambda = 0$, notwithstanding the absence of water, the presence of the hydronium complexes is sufficient to drive phase separation with a local disordered lamellar structure. Altogether, these data demonstrated that our model is able to grasp the overall phase behaviour of sulfonated ionic surfactants [120], in a wide range of hydration conditions. In all cases a sharp phase separation was evident, with the charged sulfonic heads decorating the interface between the adsorbed fluid and the hydrophobic sections of the surfactants. Hydroniums condensate at the charged interface at the lowest values of λ, while a significant fraction is solvated by water, far from the interfaces at high hydration.

5.1 Static structure factors

The above qualitative description of the phase diagram based on visual inspection can be completed by characterising the system organisation via the static structure factor, $S(q)$. Here, q is scattering vector in reciprocal space. In our simulations, we can calculate the neutron scattering structure factor directly at the microscopic level by

$$S(k) = \left\langle \frac{N}{\sum_\alpha N_\alpha b_\alpha^2} \sum_\alpha \sum_\beta b_\alpha b_\beta S_{\alpha\beta}(\vec{k}) \right\rangle_{|\vec{k}|=k}, \qquad (5.1)$$

where b_α is the coherent neutron scattering length for species α (see table 4.2). Because of the finite size of our simulation box, we consider only the wave vectors of the form $\vec{q} = \left(n_x \frac{2\pi}{L_x}, n_y \frac{2\pi}{L_y}, n_z \frac{2\pi}{L_z}\right), n_{x,y,z} \in \mathbb{N}$, with $L_{x,y,z}$ being the dimensions of the simulation cell in each direction. In the case of united-atoms beads, α is the sum of the scattering lengths of its components. $\langle \cdot \rangle_{|\vec{q}|=q}$ is the spherical average over wave vectors of modulus q. The partial static structure factors involving species α and β are defined as

$$
\begin{aligned}
S_{\alpha\beta}(\vec{k}) &= \frac{(1 + \delta_{\alpha\beta})}{2N} \rho_\alpha(\vec{k}) \rho_\beta^*(\vec{k}), \qquad (5.2) \\
\rho_\alpha(\vec{k}) &= \sum_{l=1}^{N_\alpha} \exp\left(i\vec{k} \cdot \vec{r}_l\right),
\end{aligned}
$$

and $\vec{r}_l$ is the instantaneous vector position of bead l. In experiments space-averaged information only is accessible, in the form of diffraction diagrams, as those shown in figure 5.2. These represent as colour maps the total scattering intensity, projected on the $(q_x, q_y)-$plane of the detector. Angular integration of the $S(q_x, q_y, q_z)$ data, at constant $q = \sqrt{q_x^2 + q_y^2 + q_z^2}$, directly provides $S(q)$ of Eq. (5.1). Here, we

Figure 5.2: Neutron diffraction patterns calculated from the system units coordinates in different equilibrium phases, at several hydration levels. The intensity is visualised as a colour-map in the $(q_x, q_y)-$plane. In this representation we can observe the progressive ordering (apparition of higher order peaks), and orientation (intensity concentrates on the $q_y = 0$) as the hydration is decreased.

rotated the simulation boxes prior to computing the static structure factor, so as to align the x, y, z directions with the preferred orientations of the surfactants, which we obtained by performing the principal component analysis of the ensemble of the end-to-end vectors. We expect that as a result, the structure factor intensities will be maximal in the (q_x, q_y) plane.

Here we discuss the data presented in figure 5.2 For the most hydrated cases, $\lambda = 32$ and 16, we observe a spherically symmetric structure factor, indicating that no preferred orientational order is present in the system, as expected in the fully developed micellar phase. By decreasing the hydration, we observe the apparition of higher intensity regions close to the $q_y = 0$ line (see for example $\lambda = 12$), which indicates the ordering of nano-structure and the progressive definition of preferential orientations for the domains. The anisotropy of the diffraction pattern gradually increases as the hydration is decreased, and for hydrations lower than $\lambda = 8$ we observe the apparition of higher order Bragg peaks. At $\lambda = 4$, the order is maximal and we remark the presence of second and third Bragg peaks, well aligned on the $q_y = 0$ line, indicating a single preferential direction in the system. This is expected given the extremely neat ordering of the lamellar phase at this hydration (see snapshots in figure 5.1). As we decreased further the hydration ($\lambda = 2$ and 0), we still observed the higher order peaks, but we also remarked the definition of multiple preferred orientations, indicating that at these hydrations the structure is only locally lamellar, as can be seen on the corresponding simulation snapshots.

The total static structure factors, at all hydrations, are shown in figure 5.3. The main features of these curves are the first peak at low-q, whose position corresponds to the average distance between surfactant clusters, and the higher order peaks, at larger q, which carry information about the arrangement of surfactants and, therefore, of the phase symmetry. We observe that, as we increase the hydration, the position of the peaks shift toward smaller wave-vectors, indicating that the distance between the surfactant aggregates increases. This is the expected effect of swelling of the system when increasing water content. As seen in the 2D diagrams, the highest-symmetry phase is found for $\lambda = 4$, where the smectic order associated to the lamellar phase is maximum and three well-defined Bragg peaks appear.

Additional information comes from the partial structure factors, $S_{\alpha\beta}(q)$, shown in figure 5.3 (centre and right) for $\lambda = 4$ (centre) and 32 (right). These carry information on the spatial correlations between domains occupied by different species. We show as colour-maps all the independent indicated $S_{\alpha\beta}(q)$, with $\alpha \leq \beta$ and $\alpha, \beta = \mathrm{CF_2, S, O_3, O_W, H_W, O_H, H_H}$. There are 28 terms in total and we are obviously not interested in scrutinising all these data in details. We stress a few features, by visual inspection. First, for $\lambda = 4$, non-zero signal is concentrated at $q^* \simeq 0.23$ Å^{-1} in regions related to correlations of beads pertaining to surfactant or absorbed fluid domains, *separately*. There are no significant backbone/aqueous domains correlations contributing constructively to the total signal, and regions of highest intensity correspond to $\mathrm{CF_2}$-$\mathrm{CF_2}$, $\mathrm{O_W}$-$\mathrm{O_W}$, $\mathrm{O_W}$-$\mathrm{H_H}$ and $\mathrm{H_W}$-$\mathrm{H_W}$ correlations. In contrast, a certain degree of anti-correlation, producing negative values for $S_{\alpha\beta}(q)$ at the same q^*, is associated to interactions of the $\mathrm{CF_2}$ beads with absorbed water atoms. The intensity of the diffraction peak therefore mainly comes from independent contributions due to the confining matrix and the absorbed flu-
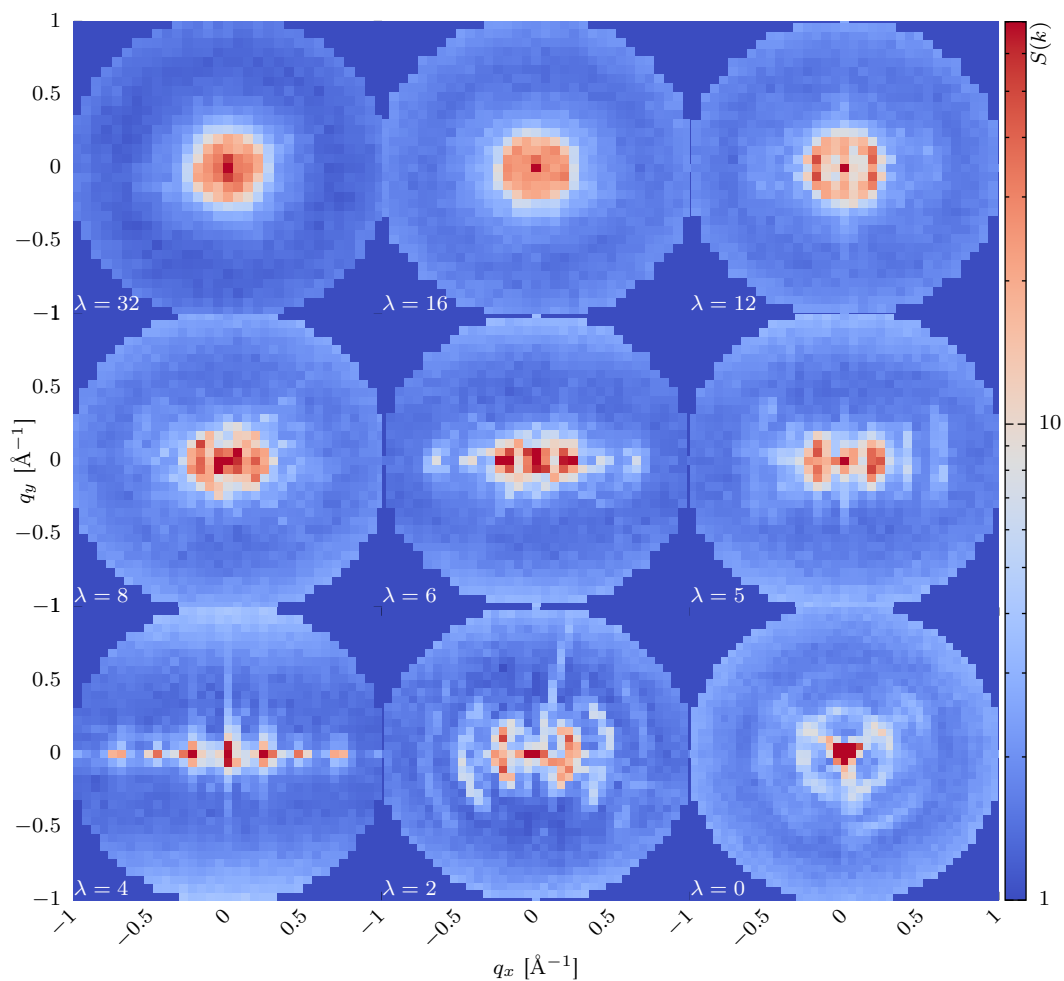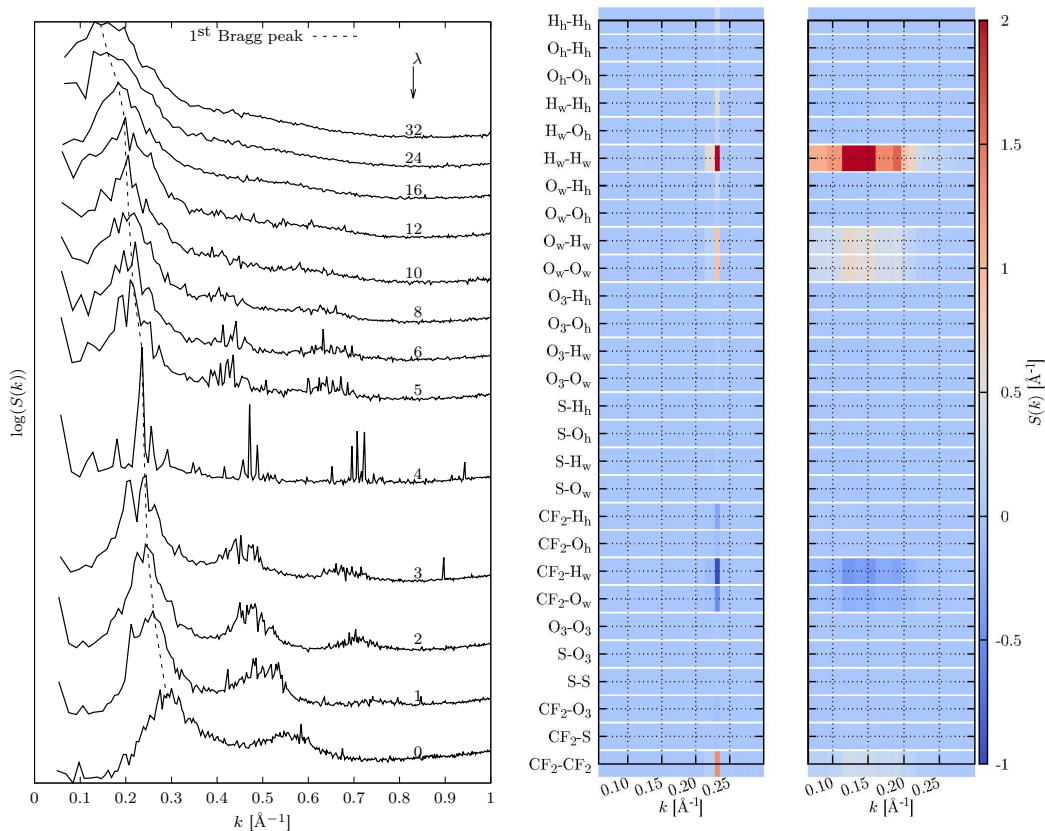
Figure 5.3: Left: Neutron diffraction patterns calculated from the system units coordinates in different equilibrium phases, at hydration levels decreasing from top to bottom. We shifted the curves for clarity. Each curve goes to 1 as $q \to \infty$. q_0, the position of the first Bragg peak is indicated by the dashed line. Right: Partial static structure factors, $S_{\alpha\beta}(q)$. We have considered all interacting pairs α, β with $\alpha \leq \beta$, for a total of 28 different contributions. We show the results for $\lambda = 4$ (left) and $\lambda = 32$ (right).

ids, with a (mild) destructive interference associated to the interfaces. The fact that the anti-correlated negative signal is also localised at q^* is not surprising, if we note that the associated length scale $l^* = 2\pi/q^* \simeq 27$Å is related to the repetition period of like-domains. This implies that starting from the surfactant (ionic) phase and moving of a distance l^*, a system's unit will never reach the ionic (surfactant) phase. In the case of $\lambda = 32$ (right) the situation is in general qualitatively similar, with the maximum intensity region shifted to lower values of q, and the total constructive signal being spread on a larger q−range, due to disorder. However,

$$l_1(\lambda) = l(\lambda) - 2l_s(\lambda)$$

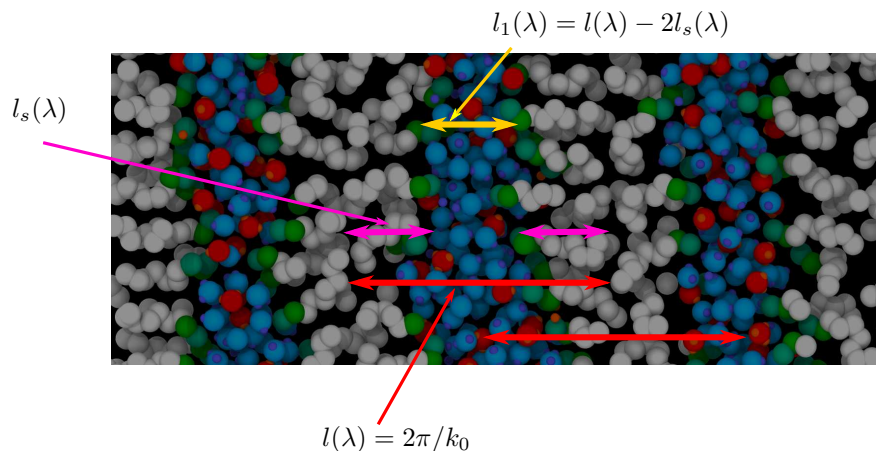$l_s(\lambda)$

$$l(\lambda) = 2\pi/k_0$$

Figure 5.4: The characteristic lengths in a slice of a $\lambda = 4$ lamellar structure: $l_1(\lambda)$ can be obtained from the length corresponding to the position of the first Bragg peak (q_0) and the average surfactant end-to-end distance, $l_s(\lambda)$.

the signal associated to both hydronium/hydronium and hydronium/water correlations and due to the ionic condensation at the interface at very low hydration is completely suppressed, following significant solvation of ions, as we will see below.

5.2 Confinement length scales

Interestingly, the above *global* spatially-averaged static structure factors provide precise information about *local* geometrical properties of the confining matrices. More precisely, we are now in the position to discuss the variation of the typical size of the ionic domains available for transport of the absorbed fluid, as a function of the hydration level.

From the position $q_0(\lambda)$ of the first-order Bragg peak (see figure 5.3 (left)), we can extract $l(\lambda) = 2\pi/q_0(\lambda)$, which is commonly associated to the average distance between the centres of mass of the hydrophobic aggregates. From these data we can build $l_1(\lambda) = l(\lambda) - 2l_s(\lambda)$, where l_s is the average end-to-end distance of the surfactants. Helped by inspection of the snapshot at $\lambda = 4$ of figure 5.4, it is easy to convince oneself that $l_1(\lambda)$ is an *indirect* measure of the size of the ionic channels. Our data are shown in figure 5.5 and quantify the swelling behaviour of the system. For $\lambda \leq 6$, l_1 increases linearly with λ, with a slope $\simeq 1$. This corresponds to the expected swelling in the lamellar phase (see, for instance, reference [119]), where the distance between surfactant domains increases affinely, following the volume increase of the intercalated fluid. At higher values of λ, a clear cross-over is visible,

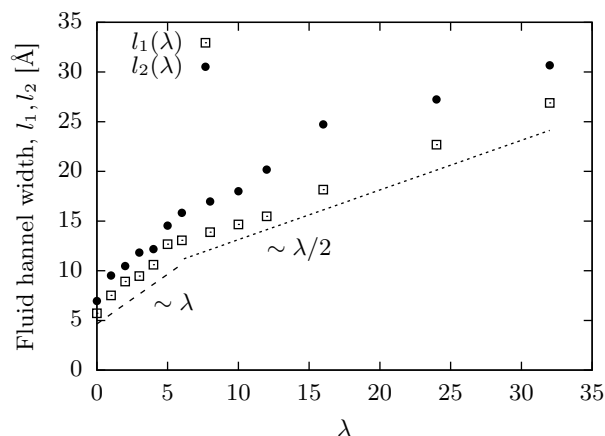Figure 5.5: λ-dependence of the size of ionic channels as calculated from the position of the first Bragg peak, l_1, in the static structure factors and from the direct determination of the aqueous domains extent, l_2, as discussed in the text. The dashed lines are guides for the eyes, of slope 1 and 0.5 at low and high hydration, respectively.

with l_1 that can be interpolated by a straight line of slope $\simeq 1/2$. Rationalising this behaviour is however difficult, due to the presence of interfaces of increasing curvature and sensible disorder in the distribution of the hydrophobic aggregates.

These data can be further strengthened by a *direct* independent measure of the width of the ionic channels, by computing the distribution of the distances of the fluid molecules (both water and hydronium) to the closest surfactant sulfonated head. From these distributions we have estimated the channels sizes, l_2, as the distance encompassing 99% of the fluid molecules. Our results are shown in figure 5.5. In figure 5.6, we present the ratio between the surface area of the interface and the volume of surfactant, together with the width of the fluid channel l_1. For $\lambda \leq 6$ we have $l_1 \simeq l_2$, as expected for highly symmetric phases. At higher values of λ, l_2 is always higher than, although of the same order of, l_1, providing an upper bound to the size of the ionic domains at each λ in the presence of disordered curved interfaces. Interestingly, the ratio between the surface area of the interface and the volume of surfactant follows a similar trend. This illustrates how the re-arrangement of the nanostructure with the increase of hydration increases the surface area of the interface between the surfactant and ionic domains.
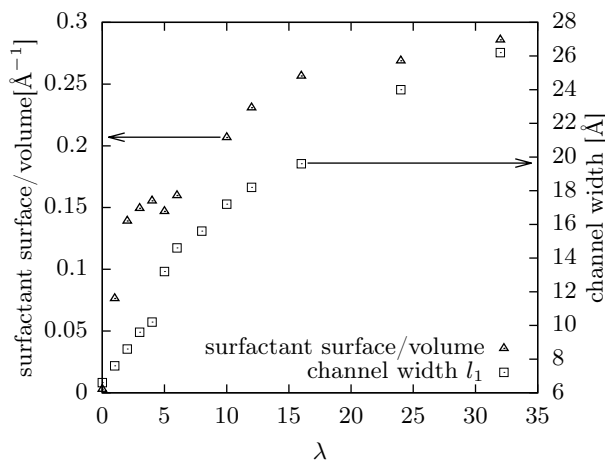
Figure 5.6: Variation with the water content, λ, of the average size of the self-assembled ionic channels and the extension of the generated hydrophobic/hydrophilic interfaces, normalised to the volume occupied by the surfactant macromolecules. Data for the confining size are similar to those reported in [156] and in the previous chapters, re-evaluated from the new system snapshots. The arrows indicate the axis relevant for each data set.

5.3   Interfaces and the absorbed fluid

Interfaces play a crucial role in the physics of our surfactants systems. In figure 5.7 we show local configurations of the interfaces generated at $\lambda = 1$ and 16, in the (pseudo) lamellar and micellar phases, respectively. The sketched segments indicate the relative orientations of selected adjacent surfactants, parallel (left) and at a non-zero angle (right) in the two cases. Obviously these conform to the charge distribution geometry at the interfaces, planar in one case and with a finite curvature radius in the other. We can expect the coordination features of both surfactants and fluid molecules, and therefore wetting properties at the interface, to be sensibly different in the two cases. We therefore first focus on the coordination properties of surfactants heads, in the coordination sphere indicated by the circles in figure 5.7.

   In figure 5.8 (left), we plot the average number of molecules of the different species comprised in the first coordination shell of the surfactant heads. This is defined as the sphere with radius $R_c = 4.3\,\text{Å}$, corresponding to the first minimum in the O_3-O_W pair radial distribution functions (not shown). These data show that, for $\lambda \leq 5$, the first coordination shell of the surfactant heads contains about 4.3 atoms pertaining to surfactant molecules. In the same hydration range, the number of fluid molecules in the first coordination shell increases from 3.1 to slightly less
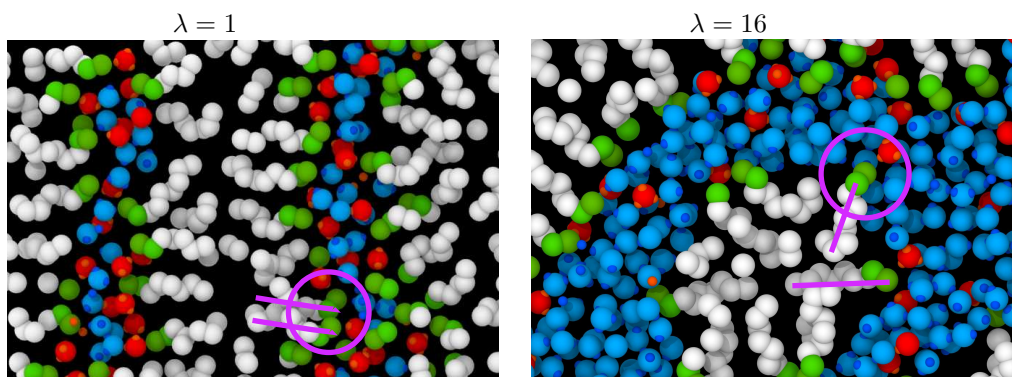
Figure 5.7: Details of typical generated interfaces with different curvature radius, together with a schematic representation of the hydration sphere (circles) used for our calculations and the mutual orientations of adjacent surfactants (lines). The snapshot on the left corresponds to $\lambda = 1$ (flat interface), to $\lambda = 16$ that on the right (curved interface).

than 5. It is interesting to note that there is no variation of this number between $\lambda = 4$ and $\lambda = 5$. More precisely, at $\lambda = 4$ the first coordination shell is saturated and added water molecules organise far from the interfaces, as we will see more in the details below.

For $\lambda \geq 5$, we observe that the number of surfactant molecules inside the first coordination shell decreases, while it increases for fluid molecules. This is the manifestation of the lamellar-to-cylindrical phase transition. By increasing λ, the system efficiently packs more fluid molecules at the hydrophilic interface, by increasing the tilt angle between adjacent surfactant and, as a consequence, the mutual distance of the sulfonic heads. The tilt angle between surfactants curves the exposed interface, giving rise to increasingly well defined cylindrical structures. At $\lambda = 16$, the number of both fluid and surfactant particles in the first coordination shell reach limiting values, which show very mild variation at higher degrees of hydration. This is a direct signature of the transition to the micellar phase, where spherical aggregates are dissolved in (bulk) water, with a total surface area of the interfaces almost independent of λ.

We can push further the analysis of the interfaces by counting the per/surfactant average number of water molecules (or hydronium ions) that are in the first coordination shell of their *nearest* hydrophilic head,

$$\mathcal{N}_{W(H)} = \frac{1}{N_s} \sum_{m \in W(H)} \left[1 - \theta(z_m - R_c) \right], \tag{5.3}$$

where z_m is the distance of molecule m to the nearest hydrophilic head. We note
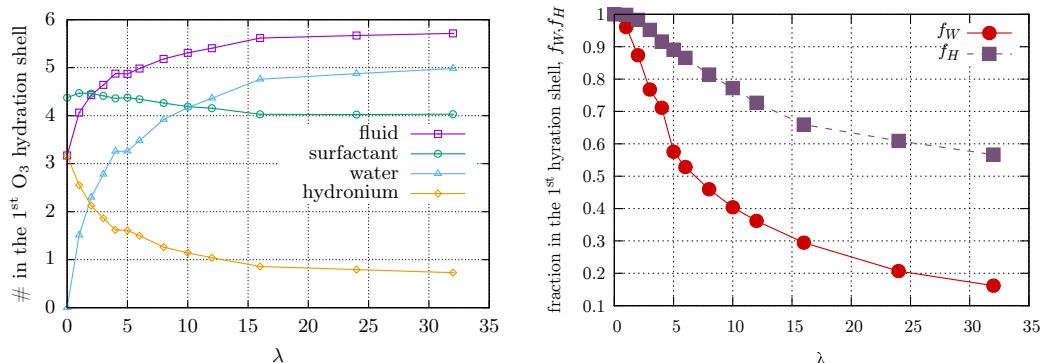
Figure 5.8: Left: $\lambda-$dependence of the average number of molecules of the indicated species localised into the first coordination shell of the O_3 bead of the surfactant heads. Right: $\lambda-$dependence of the average number of water molecules and hydronium complexes localised into the first coordination shell of the O_3 bead of the *closest* surfactant head. A detailed discussion of these data is included in the main text.

that this procedure eliminates the over-counting intrinsic to the above discussion, where the same fluid molecule could be considered as belonging to the the first coordination shell of multiple surfactant heads. Also, by construction $0 \leq \mathcal{N}_H \leq 1$ and $0 \leq \mathcal{N}_W \leq \lambda$. The quantities $f_H = \mathcal{N}_H$ and $f_W = \mathcal{N}_W/\lambda$ can therefore be interpreted as the fraction (over the total number) of hydronium ions and water molecules in direct contact with the interface. These data are included in figure 5.8 (right) and show a few interesting features.

At very low hydration ($\lambda = 1$), almost all water molecules and hydronium ions are condensed in contact with the nearest hydrophilic head, resulting in $f_{W(H)} \approx 1$. This is evidence of a phase where all fluid molecules are localised within the first coordination shell of their nearest surfactant heads, in very thin ionic layers intercalated between the surfactant planes. For $1 \leq \lambda \leq 4$ we observe an almost linear decrease of f_W, which however still keeps a quite high value ($\simeq 70\%$) at $\lambda = 4$. Indeed, in that hydration range half of the width of the fluid channel ($l_1(\lambda)$ in figure 5.5) is smaller than or comparable to the radius of the coordination shell, meaning that most part of the added water molecules will be placed at the interface. In the same range of λ, f_H only decreases by a mere 10%, indicating however that, notwithstanding the strong Coulombic interactions which keep hydronium ions strongly bound to the sulfonate groups, there is still the possibility for a water molecule to substitute a cation at the interface.

At $\lambda = 5$, where the lamellar order is still present, the fluid channels are no longer spanned by the coordination regions of facing surfactant heads, which are saturated,
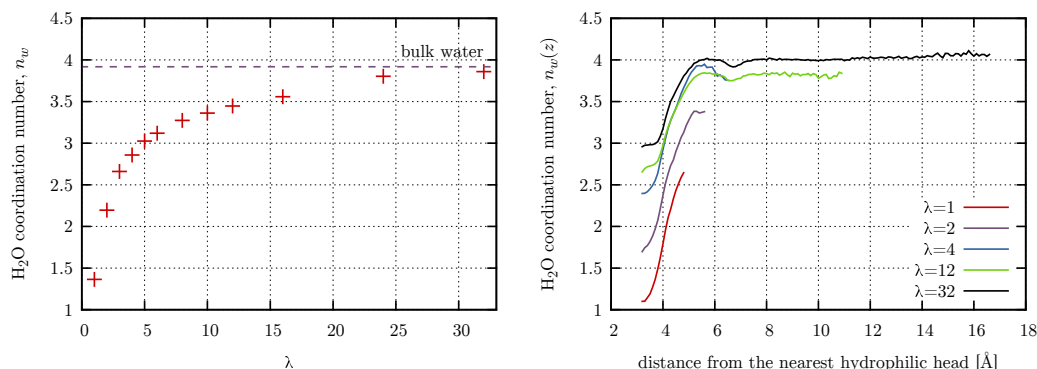
Figure 5.9: *Left:* $\lambda-$dependence of the average water-water coordination number, $n_W(\lambda)$. The dashed line indicates the values $\simeq 4$ for pure bulk water. *Right:* Space-dependent water-water coordination number, $n_W(z, \lambda)$, as a function of the distance, z, of the molecule from the closest hydrophilic head. We only show our results for the indicated values of λ, for clarity.

and additional fluid molecules are therefore placed outside the interfaces. For $\lambda > 5$, the sequence of phase transitions described before occurs, implying the progressive curvature of the interfaces. This effect increases the interfaces area available for fluid adsorption compared to that present in the lamellar phase and controls the reduction of f_W upon hydration, explaining the clear cross-over to a less-than-linear behaviour at high λ. Eventually, at very high hydration, only about 10% of the total amount of water molecules is still in contact with the interfaces, the vast majority having a prominent bulk-like character. This is at variance with the case of the hydronium ions, which even in very high hydration conditions substantially keep their interfacial character, with $\simeq 50\%$ of the entire population still bounded at the charged interfaces.

Note that the fraction of interfacial water and hydronium can also be considered as dynamical quantities. In chapter 6, we will revisit these quantities to study the residence times of water molecules and hydronium ions in the interfacial region.

We now clarify the effect of the above subtle interface/bulk character of water molecules in different regions of the ionic domains on the coordination properties of the absorbed fluid itself. We focus, in particular, on the water-water average coordination number and its variation at different distances from the interfaces. In figure 5.9 (Left) we plot the average coordination number of water molecules, $n_W(\lambda)$ at all considered hydration levels. The value for bulk water $\simeq 4$ is shown for reference. These data have been calculated with the usual technique of integrating the pair radial distribution function, $g_{O_W-O_W}(r)$, in the range $[0 : R_C]$, with $R_c =$

3.16 Å the position of its first minimum. At high hydration, we recover the value of bulk water $n_W \simeq 4$ (dashed line). By decreasing λ, n_W steadily decreases to $n_W \simeq 3$ at $\lambda = 6$, at the boundary with the lamellar phases. Next, due to the increasing extent of affine confinement, the observed decrease is much steeper, and n_W reaches a minimum value $\simeq 1.2$ at $\lambda = 1$. This is consistent with the general picture discussed above, where water molecules, hydronium ions and sulfonate groups are intercalated in the ionic channels, organising in almost mono-planar configurations.

Our simulations allow us to access even more detailed information, e.g., the space-dependent coordination number of water molecules, in different regions of the ionic channels. In figure 5.9 (right), we show the average coordination number of molecules at distance z from the closest sulfonate group, $n_W(z, \lambda)$. Obviously, $\int_0^{z_{max}} dz\, n_W(z, \lambda)\, \rho(z, \lambda) = n_W(\lambda)$, where $\rho(z, \lambda) = \sum_{i=1,N_W} \delta(z_i - z)/N_W$ is the number density of water molecules and z_i the distance of water molecule i from the closest surfactant head. These data show that, at all λ's, $n_w(z, \lambda)$ steadily increases from a highly suppressed value at $z_{min} \simeq 3$ Å in contact with the interface (z_{min} is mainly controlled by the value of $\sigma_{O_3 O_W}$, see table 4.3 in the previous section) to a maximum at the λ-dependent z_{max}, at the centre of the channels ($z_{max} \simeq l_2/2$, at all hydrations). The overall variation of $n_W(z, \lambda)$ with the distance depends on λ, decreasing from a factor of $\simeq 2.5$ at $\lambda = 1$ to $\simeq 1.3$ for $\lambda = 32$.

We conclude this discussion by observing that the details of the curve corresponding to the highest hydration level allow us to highlight the presence of three different regions inside the ionic domains, determining the most prominent character of the confined water molecules: *i) bulk-like* at large distances, $z \geq 8$ Å, in the centre of the ionic domains and far from any boundaries; *ii) intermediate*, corresponding to distances $z \simeq 6$ Å where the shallow spatial modulation of n_W is due to the well-known layering of water molecules; and *iii) interface-limited*, where the extent of nano-confinement is so high to completely destroy any resemblance of the hydrated environment with the one in the bulk phase.

5.4   Conclusions on the structure of our water/surfactant model

We have developed a coarse-grained model of ionic surfactants in solution, with explicit three-points SPC/E water molecules and four-points hydronium complexes as counterions. Extensive Molecular Dynamics simulations have been performed, over a wide range of water contents ranging from the almost dried condition, where counter-ions only are present, to the highly hydrated state where 32 water molecules per surfactant are loaded into the simulation box. We have observed very efficient system self-assembly at all hydration levels, solely driven by the forces generated by the chosen interaction potential, starting from disordered initial configurations with

no initial bias toward any phase symmetry. The generated phase behaviour has been demonstrated to nicely mimic that of sulfonated ionic surfactants, at ambient conditions, encompassing lamellar, cylindrical and micellar structural organisation. In all cases we have observed sharp charged interfaces separating the aqueous domains from the confining soft matrix, formed by the hydrophobic segments of the surfactants. Based on a very detailed analysis, the confinement sizes associated to the ionic domains have been found to increase with hydration, in the range $5 \div 25\,\text{Å}$. A transition between affine swelling and a more complex behaviour has been found at length scales of the order of $14\,\text{Å}$.

Neutron scattering static structure factors were also calculated, similar to those determined in experiments (see chapter 3). Neutron and X-rays scattering measurements on PFOSA molecules of size comparable to that of our model were reported recently [120, 119]. A nice agreement is found between our data and the experimental results, as the boundaries of the different phases (see figure 3.10), typical average inter-aggregate correlation distances and overall swelling behaviour are similar. Our model is therefore capable of realistically reproducing the PFOSA surfactant solution behaviour. This suggests that it can be used as an *in-silico* partner to the experimental study of a variety of surfactants. For instance, we could easily tune the surfactant length and generate different commercially available materials, as PFHSA (6 carbons) or PFBuSA (4 carbons) [161]. As we saw in section 3.3, the phase behaviour of these systems being quite universal, we expect limited variations compared to the present case, with the modified length of the surfactants probably controlling the hydration-level location of the different phase boundaries. Indeed, volume and surface of the hydrophobic clusters increase with the length of the molecules. This implies that longer surfactants require a higher number of fluid molecules to fully cover the larger surface area of the surfactant/water interface. We can therefore expect the cylinders/micelles transition to be shifted at higher values of λ for these shorter molecules.

In the same context, our model could also be valuably applied to generate and investigate polymeric systems, in particular perfluorosulfonic acid polymer electrolyte membranes. As we have seen in section 3.3, the quite ordered PFOSA surfactant phases were recently considered as a facilitated playground for clarifying microstructure and transport properties of nanoscopic phase-separated ionomers [120, 119]. In particular, the PFOSA molecule is very similar to the pendant side-chain of Nafion (see chapter 3), the most investigated of the PFSA polymer electrolyte membranes used as separators and proton conductors in low temperature proton-exchange membrane fuel cells and electrolysers. We so that for this reason hydrated sulfonated ionic surfactants have been proposed as model systems for the local organisation of ionomers, to quantify, among other issues, the effects of well-controlled confining geometries on proton mobility [119]. In chapter 7, we will see how this model of surfactants can be used to model the side chains of ionomers.

Based on these facts, we can conclude that with the present model we are in the position to unify in a single bottom/up computational framework the entire vast class of perfluorinated materials. Indeed, we have demonstrated here that our re-optimised force-field correctly encodes the phase behaviour and the most important structural features of a PFOSA system. Due to the similarities of the latter with the side chain of Nafion, we will (in chapter 7) employ this structure as the fundamental building-block to upscale our description to the entire ionomer, by grafting it to a strongly hydrophobic polymer backbone with tuned mechanical properties (*i.e.*, persistence length). This is of course in the same spirit of the original work of Ref. [103], but with the crucial difference that we can now count on a model with physically-sound behaviour at all length scales, ranging from local lamellar-like structures to long-range organisation of ionic and hydrophobic domains. We also note that our approach naturally provides all ingredients for generating a virtually infinite range of composite materials, obtained by doping the ionomer with elongated charged macro-molecules, including ionic liquids [162, 163]. Recently, the effect of doping ionomer membranes with ionic surfactants has been investigated [110]. We will also explore this possibility in chapter 7.

Of even greater general interest, our model can be seen as a powerful tool for generating efficient self-assembly of soft interfaces with a controlled degree of curvature to study water in various confining geometries (see chapter 2). Recent fundamental work [45, 164, 165] has focused on assembly driven by hydrophobic forces, even in the presence of hydrophilic units, as it is the case here. It has been shown that the properties of water molecules at the interface with extended molecular aggregates are certainly controlled by the nature of the interactions between water molecules and the aggregates, but a crucial role is played by the extent of the surface occupied by the aggregates itself. In particular, the associated curvature radius strongly affects the wetting features, or the hydrogen bonding formation. In the limiting case of purely hydrophobic aggregates of large available surface, water molecules at the interface even acquire a gas-like character, with a strongly suppressed interfacial density [164] and a number of formed hydrogen bonds significantly lower than that in the bulk [45]. The present case could appear quite different, with the presence of hydrophilic interactions between surfactant heads and water molecules, and the possibility to form additional hydrogen bonds with both the hydronium complexes condensed at the interfaces and the fully dissociated sulfonated groups. However, our data also point to non-trivial modifications of the character of water molecules in the presence of interfaces with different degrees of curvature. In particular, the degradation of both average and space-dependent (at different distances from the interfaces) coordination properties are expected to impact structure and life-times associated to the hydrogen bonds network and, in general, transport properties of the adsorbed fluid itself. We are convinced that our work provides a well-designed foothold to attack all these issues, which are of paramount importance in mod-

ern science, ranging from soft synthetic materials to systems of biological interest [69, 65].

In the following, we will tackle the issues of transport of water and hydronium ions in our self-assembled ionic surfactant phases.

Chapter 6

Transport properties in self-assembled hydrated ionic surfactants

As we saw in chapter 5, the nanostructure of hydrated surfactant assemblies is heavily influenced by the properties of the interface. In particular, we showed how the successive rearrangements allow the system to accommodate increasing numbers of water molecules in the interfacial region. In this chapter, we address the issue of transport in such systems, with a particular emphasis on the details of the behaviour of water and hydronium in the interfacial region. We will tackle the issue of the nature of transport of water and hydronium, and we will elucidate the role of the interface.

6.1 Simulation details

In order to assure an optimal thermalisation of the systems at all hydrations, we reinitialised the simulation boxes starting from the self-assembled configurations analysed in chapter 5 and in reference [156]. We considered 9 values of the hydration λ among the samples presented in chapter 5, ranging in the interval $[1, 32]$, which encompass all interesting regions of the phase diagram. A pure water system (bulk) trajectory was also generated, as a reference.

At each λ, we produced a trajectory spanning a total time $\tau_{\max} = 10$ ns, a dynamical window sufficiently extended to allow comfortable observation of the very slow dynamics in the most confined cases. The time step used for the numerical integration of the equations of motion is $\delta t = 1$ fs. We worked in the constant temperature and pressure (NPT) ensemble, with $T = 300$ K and $P = 1$ atm, with the characteristic time of both thermostat and barostat set to $\tau_{\mathrm{T}} = \tau_{\mathrm{P}} = 1$ ps. We

dumped complete systems configuration with a frequency of 10 ps, for subsequent analysis.

6.2   Characteristic time scales

In this section we describe our computer simulation data. Before going into the details of the dynamical properties of the systems, let us address the role of the mobility of the surfactant phase. To this end, we have determined the time at which the self intermediate scattering function $F(q,t)$ of surfactant, water, and hydronium molecules and ions reaches the value of e^{-1} (noted $\tau(e^{-1})$). The precise definition of the self intermediate scattering function is given in equation 6.2. The characteristic times $\tau(e^{-1})$ are excellent indicators of the average time scale on which transport on length scales corresponding to the associated q-value takes place. In figure 6.1 we present these time scales as a function of the wave number q at all λ. As can be seen, at high hydration this characteristic time scales as q^{-2}, which is characteristic of diffusive processes. As the hydration is decreased, this behaviour might change, however it is not our goal to quantify this change. What should strike the reader when studying this figure is the clear separation of time scales pertaining to water, ions, and surfactants. Indeed independently of hydration, the time scales pertaining to ions and surfactants are one order of magnitude slower than those of water and ions respectively. At low hydration, the characteristic time is even larger than the duration of the simulation. From this consideration on the separation of time scales, it should be obvious that the flexibility of the surfactant matrix will not affect the dynamics of the liquid in any significant manner because from the point of view of a water molecule, the matrix might as well be immobile. This allows to emphasise that the importance of using a soft matrix comes from its ability to self assemble.

In summary, because the time scales on which the dynamics of water, hydronium, and surfactants are clearly separated, the effect of the dynamics of the matrix on the dynamics of water is negligible. As a result, the dynamics in the aqueous phase are controlled by the extension of the interfaces and the confinement size, all of which can safely be considered static properties.

We have fully characterised the dynamics of water molecules adsorbed in the surfactants nano-phases at the different hydration levels, in terms of mean-squared displacements and intermediate scattering functions. We have next completed our analysis by probing well-designed correlation functions associated to the typical life-times of water molecules in the hydration layer, in contact with the confining hydrophobic matrix.

70
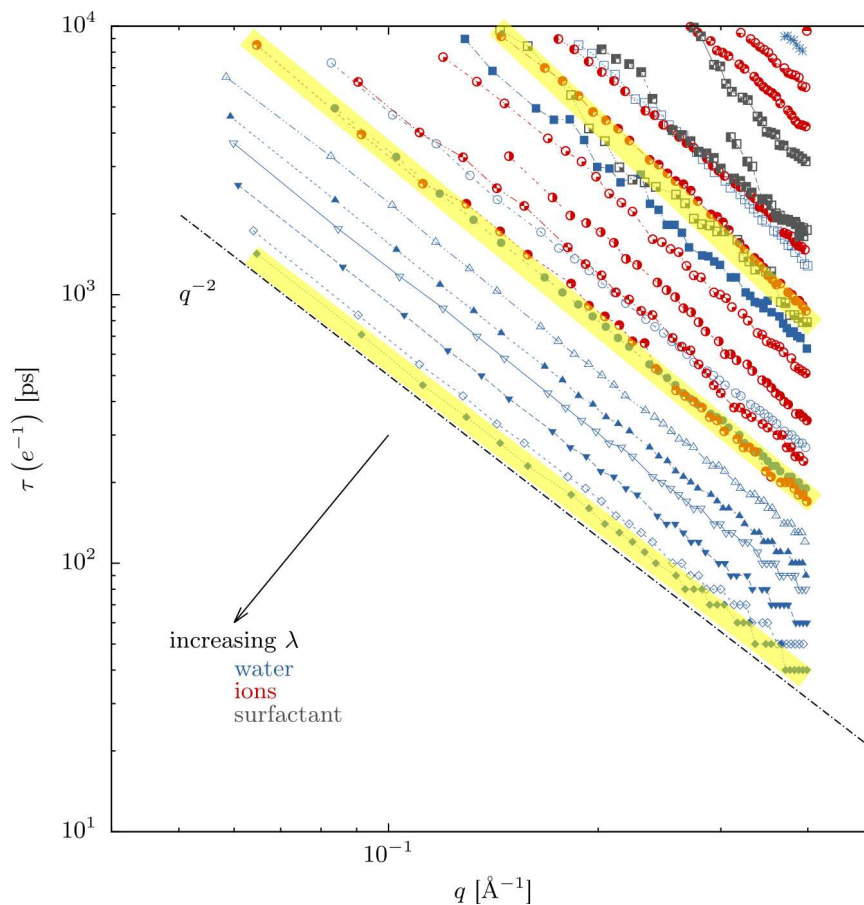
Figure 6.1: Characteristic time $\tau(e^{-1})$ at which the self intermediate scattering function $F(q,t)$ reaches the value of e^{-1}. The data pertaining to water, ions, and surfactants are shown in blue, red, and gray respectively. Connected data points correspond to a single sample at specific hydration. Shorter times correspond to higher hydration, as indicated by the arrow. We highlighted in yellow the data points belonging to the highest hydration level to emphasise the separation of time-scales.

6.3 Evidence of sub-diffusive behaviour

By using the produced system trajectories, we first computed the water molecules mean-squared displacement (MSD)

$$\langle r^2(t)\rangle = \frac{1}{N_w} \sum_{i=1}^{N_w} |\mathbf{r}_i(t) - \mathbf{r}_i(0)|^2 \, , \tag{6.1}$$

71

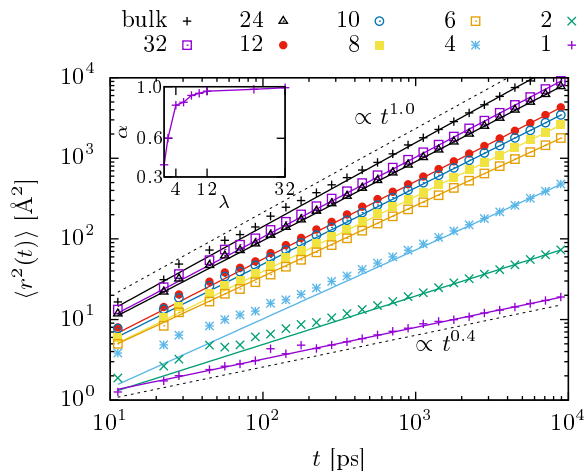Figure 6.2: *Main panel:* Mean-squared displacements $\langle r^2(t) \rangle$, calculated from the time-dependent coordinates of the water oxygen atoms. The solid lines are the power-law fits described in the main text, the dashed lines indicates the limiting Fickian (top) and highly sub-diffusive (bottom) limits, corresponding to $\alpha = 1$ and 0.4, respectively. *Inset:* λ-dependence of the exponent α, determined from $\langle r^2(t) \rangle \propto t^\alpha$.

where N_w is the number of water molecules, and $\mathbf{r}_i(t)$ is the position vector of the oxygen atom pertaining to molecule i at time t. In Fig. 6.2 (top) we show our data at the investigated various hydration levels (higher on top), together with the results for bulk water. We observe two interesting features: first, by decreasing the hydration, the mean-squared displacement at fixed time decreases, as generically expected due to an increasing crowding associated to the surfactant units. Second, and more intriguing, while the data-points for the bulk fall on a straight line of unitary slope (the linear dependence expected for water at ambient conditions), this slope progressively decreases with the hydration, indicating a power-law behaviour with an exponent less than one. This is characteristic of *sub-diffusion* [4].

To quantify this feature, we fit the MSD at long times to a power-law of the form $\langle r^2(t) \rangle \propto t^\alpha$, with $0 < \alpha = \alpha(\lambda) \leq 1$. We show the results of the fit as lines in Fig. 6.2, and the values of the exponent $\alpha(\lambda)$ in the inset of the same figure. We observe that α varies slowly from a value close to 1 at $\lambda = 32$, corresponding to the expected Fickian diffusion, to $\alpha \simeq 0.85$ at $\lambda = 5$, close to the boundary of the lamellar phase. This behaviour seems to correlate with the corresponding decrease of the surface are of the interface shown in figures 5.5 and 5.6. Next, α abruptly decreases to a value $\simeq 0.4$ at $\lambda = 2$, certainly controlled by the extreme confining sizes at almost constant available interface. Note that this value is even
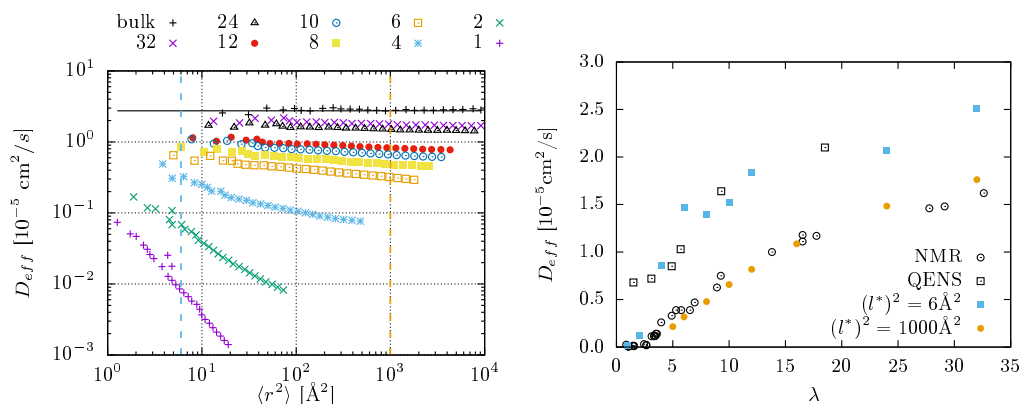
Figure 6.3: *Left:* The effective diffusion coefficient, D_{eff}, computed from Eq. (1.10), plotted parametrically against $\langle r^2(t)\rangle$. The solid black line is the result in the bulk for the considered water model, corresponding to $D \simeq 2.74 \times 10^{-5}$ cm^2/s. The dashed vertical lines, indicate the (squared) length scales $\simeq 6$ and $\simeq 1000$ Å^2 used to select the values of D_{eff} shown in the bottom panel, as discussed in the text. *Right:* The values for D_{eff} selected by the two verticals lines of the above panel are shown as closed symbols. We also show the diffusion coefficients obtained by PFG-NMR and QENS spectroscopy [119], which probe the dynamics on long and short length scales, respectively.

lower than $\alpha = 0.5$, corresponding to the case of single-file diffusion [166], where molecules are organised in uni-dimensional configurations, with a vanishing position swap probability for adjacent molecules. Altogether, these data demonstrate that our model allows to continuously tune the degree of sub-diffusion by varying the hydration level, interpolating between the extreme cases of Fickian and single-file-like diffusion.

As we saw in chapter 1, in this context, the fluctuation-dissipation Einstein relation between the mean-squared displacement and the diffusion coefficient does not hold, but we can define an effective diffusion coefficient D_{eff}. The effective diffusion coefficients and the corresponding $\langle r^2(t)\rangle$ are plotted parametrically in Fig. 6.3 (top). Consistently with the data of Fig. 6.2, the most diluted cases exhibit diffusion coefficients that are rather constant and close to the value of the bulk. In contrast, upon decreasing hydration, D_{eff} is strongly suppressed, with this effect becoming increasingly evident as the measured $\langle r^2 \rangle$ increases.

An important remark is in order at this point. The data shown in Fig. 6.3 (left) provide us with a unique rationalisation of the diffusion properties probed by different experimental spectroscopic techniques. We illustrate this point in Fig. 6.3 (right), where we compare our results with the values obtained by Pulsed-

Field Gradient Nuclear Magnetic Resonance (PFG-NMR) [167] and Quasi-Elastic
Neutron Scattering (QENS) experiments on gels of PFOSA surfactants [119]. We
recall that PFG-NMR (open circles) measures the self-diffusion of water on large
distances, of the order of the micrometer, with a typical time scale of a few millisec-
onds, while QENS (open squares) probes proton displacements of the order of a few
angstroms, on time scales ranging from one to typically a few hundreds picoseconds.

Following an uncommon protocol, we sample our data at fixed values of
$\langle r^2 \rangle = (l^*)^2$, compatible with the above length scales (vertical dashed lines in the
top panel of Fig. 6.3). Obviously, the micrometer range explored by PFG-NMR is
far beyond the limit of our simulations. We note however, that at least for the high-
est hydration levels, D_{eff} is almost length-scale independent for $\langle r^2(t) \rangle \geq 10^3$ Å^2.
This allows us to safely fix an observation threshold at $l^* \simeq 32$ Å. Similarly, we have
determined a short length-scale value of D_{eff} with $l^* \simeq 2.4$ Å, which is compatible
with the typical nano-scale distances probed by QENS. Interestingly, the simula-
tion points nicely reproduce the hydration dependence of both experimental data
sets, without resorting to any additional consideration about different dynamical
processes on different time scales. Our model therefore seems to provide not only an
adequate dynamical behaviour compared to the real system, but also a framework
to interpret experimental results, without needing any fitting procedure (beside the
determination of α). In the following we will demonstrate that it also is an efficient
tool to pinpoint the origin of the sub-diffusive behaviour described here.

6.4   Existence of two dynamical populations

Additional information on the dynamics of the water molecules is carried by the
(self-)intermediate scattering function,

$$F_s(q,t) = \frac{1}{N_w} \sum_{i=0}^{N_w} \left\langle e^{i\, \mathbf{q} \cdot (\mathbf{r}_i(t) - \mathbf{r}_i(0))} \right\rangle_{|\vec{q}|=q}, \tag{6.2}$$

where $\langle \rangle_{|\vec{q}|=q}$ is the spherical average over wave vectors of modulus q. A strong
connection exists in the bulk between the $F_s(q,t)$ and the diffusion coefficient.
We expect it to partially survive, even if in some modified form, in confinement
conditions. The Fourier transform of Eq. (6.2) is the dynamical structure factor,
$S(q,\omega)$, measured in the QENS experiments mentioned above. Here we focus on
the value $q^* = 0.7$ Å^{-1} [1]. We show our data at all the indicated values of λ in

---

[1]At this q-value the effect of confinement is clearly observed in the QENS spectra analysis.
More precisely, the Half Width at Half Maximum (HWHM) of the Lorentzian-shaped fitting line
starts to deviate from a classical random jump diffusion behaviour and enters into a plateau-like
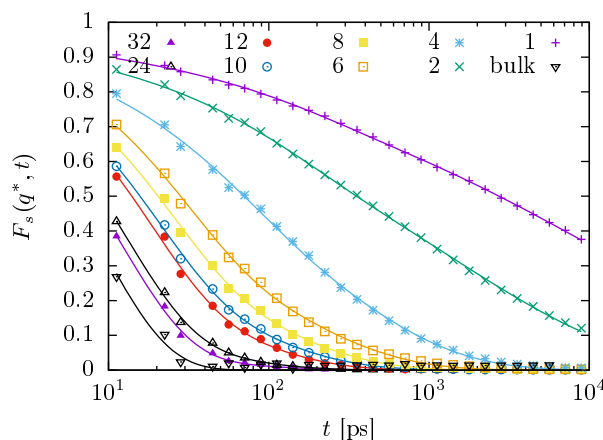regime, attributed to spatial restrictions

Figure 6.4: The self-intermediate scattering functions, $F_s(q^*, t)$, calculated from the oxygen atoms of the water molecules via Eq. (6.2) (symbols). These data correspond to $q^* = 0.7$ Å^{-1}, at the indicated values of λ. We also show as solid lines the best-fits to the data, according to Eq. (6.3). These results strongly support the hypothesis of the existence of two dynamical populations, as discussed in details in the main text.

Fig. 6.4, together with the reference case of the bulk. We observe that the decay of $F_s(q, t)$ becomes progressively slower as the hydration is decreased, and that the general shape of these functions is quite complex. In the following we quantify these observations.

The long-time behaviour of $F_s(q, t)$ for bulk molecular liquids is often represented as a stretched exponential of the form $\propto e^{-(t/\tau)^\beta}$. Here τ is the typical time scale associated to the observed relaxation, and $0 < \beta \leq 1$ is the stretching parameter. The case $\beta = 1$ corresponds to the simple exponential behaviour, $\beta < 1$ describes the case where non-trivial processes concur to the average relaxation of the correlation function. As one could expect from the extremely complex behaviour of $\langle r^2(t) \rangle$, this simple functional form alone is not able to accurately reproduce our data, especially at low λ where the degree of sub-diffusivity is higher.

The simplest alternative choice is to assume the existence of two molecular populations characterised by different dynamical properties, by analogy with the models developed for ionomers (chapter 3) [107, 109, 119]. In this quite crude representation, a subset of the total number of water molecules evolve diffusively, not very differently than those in bulk conditions, on a relatively fast time scale. The remaining part, in contrast, include all the complex effects coming from confinement in the surfactant phase, evolving on slower time scales. The precise features of the two populations should intuitively depend on the details of the confinement envi-

ronment and, ultimately, on λ. Given the additivity of Eq. (6.2), we can therefore consider the very simple model,

$$F_s(q,t) = f_{\text{SD}}\, e^{-\left(\frac{t}{\tau_{\text{SD}}}\right)^{\beta}} + (1 - f_{\text{SD}})\, e^{-\left(\frac{t}{\tau_{\text{D}}}\right)}, \qquad (6.3)$$

where a simple and a stretched exponentials encode the dynamics of the diffusive (D) and sub-diffusive (SD) water molecules, respectively [2]. Since this latter population is the slowest, we can expect $\tau_D < \langle \tau_{SD} \rangle$, where the average time scale associated with the sub-diffusive population is $\langle \tau_{SD} \rangle = (\tau_{SD}/\beta)\, \Gamma\left(1/\beta\right)$, with $\Gamma(x)$ the Gamma function. We can also obtain the fraction of diffusive molecules, as $f_D = (1 - f_{SD})$.

   We were able to obtain excellent fits to our data with this model, that we show as solid lines in Fig. 6.4. The obtained values of f_{SD} span the entire possible variation range, assuming a value of 0.05 at the highest λ and of 0.95 at the lowest available hydration level. This variation is followed by β-values ranging from 0.6 to 0.3. These observations point to an increasing modification of the dynamics compared to the bulk unconstrained case, and to a very probable connection between the sub-diffusive average character of the dynamics and the existence of molecular populations, characterised by heterogeneous dynamical properties. We postpone a much more elaborated discussion of the calculated values for both the time scales and f_{SD} to the following (see Fig. 6.8).

6.5   The interface as the source of sub-diffusion

The self-assembled confining environments considered here are characterised not only by variable size of the ionic domains available for transport (Fig. 5.6), but also by the variable topological features of the formed interfaces, which evolve from the almost perfect planar configurations of the lamellar phase, to configurations of increasing convexity in the cylindrical and micellar phases. It is natural to expect that beside the obvious role played by the extremely tight confining sizes at very low λ, these well-developed interfaces significantly perturb the dynamics of the adsorbed fluid molecules, participating to the generation of the observed sub-diffusion. More specifically, the surfactant sulfonic acid groups are hydrophilic and negatively charged, resulting in a strong attractive potential between the interface and fluid molecules within the range of these interactions. This leads to the hypothesis that the fluid molecules in the vicinity of the interface can be trapped at the interface, which reduces their possibility of diffusing at the normal rate. This constrain

---

[2]Note that for molecular liquids the functional form of Eq. (6.3) is sometimes used for fitting $F_s(q,t)$ in the entire time range, with the simple and stretched exponential well representing the short (caging) and long (structural relaxation) time behaviour, respectively. Here, these two terms are needed for convincingly reproducing the structural relaxation alone, for times $t \geq 10$ ps.

would next be transferred to successive fluid layers, with a strength reduced as the distance from the interface increases.

On this basis, we now focus on the dynamical properties of the fluid adsorbed at the interface *only*, by selecting the sub-set of fluid molecules comprised in the first hydration layer of the surfactant heads. We therefore define the binary presence function, $p(\mathbf{r})$, for a water molecule at position $\mathbf{r}$: $p(\mathbf{r}) = 1$ if it exists a charged surfactant head at $\mathbf{r}_0$, such that $|\mathbf{r}_0 - \mathbf{r}| \leq r_c$, and zero otherwise. In what follows we have fixed $r_c = 4$ Å. Applying this operator to the position of the oxygen atoms for every snapshot of our trajectory, we have obtained N_w series of N_s binary values, $\{p_{i,n}\}$. Here, N_s is the number of system snapshots, each corresponding to a simulation time $t_n = n\,\delta t$, with $n = 0, \ldots, N_s - 1$, and $i = 1, \ldots, N_w$.

From the lists $\{p_{i,n}\}$ we can in principle determine the probability distribution of the residence times at the interface of all molecules, by simply counting the number of non-zero segments of given length (for each i). This should allow us to define an average survival time at the interface. Unfortunately this is problematic, as it is clear from the data sets shown in Fig. 6.5 top, at the indicated values of λ. These distributions show significant power-law tails $\propto t^{-x}$ (solid lines in the main panel and points in the inset), with even $x < 2$ at the lowest hydrations ($\lambda \leq 2$) which hinders a consistent definition of average values, and $2 < x < 3$ for $2 < \lambda \leq 10$, which results in an undefined variance. This also implies that there is always a significant probability to observe life-times corresponding to the total time length of the simulation, making extremely hard adequate statistical sampling. This conclusion is verified from the data of Fig. 6.5 (bottom), where we plot the same probability distributions as above, with the additional constraint that the considered non-zero segments must include $\tau_{\max}$ [3]. Clearly, at low hydration values the most likely residence time of water molecules present at the interface at the end of the run is the duration of the run, as indicated by the arrows.

These observations are of particular interest, because long-tailed distributions of survival times are known to give rise to sub-diffusive random walks. This is the case, for instance, of the continuous-time random walk (CTRW, see chapter 1), where particles are allowed to move after having been arrested for a waiting time, t_w, drawn from a power-law distribution. Evidences of CTRW have been observed in simulations of water confined in lipid bi-layers [64, 65], among other cases.

The difficulties described above can be partially circumvented by determining the time scale associated to the variation of well-designed correlation functions. We first consider the correlation function of the survival times of water molecules laying

---

[3]Note that the two probability distributions must coincide in the infinite-time limit.
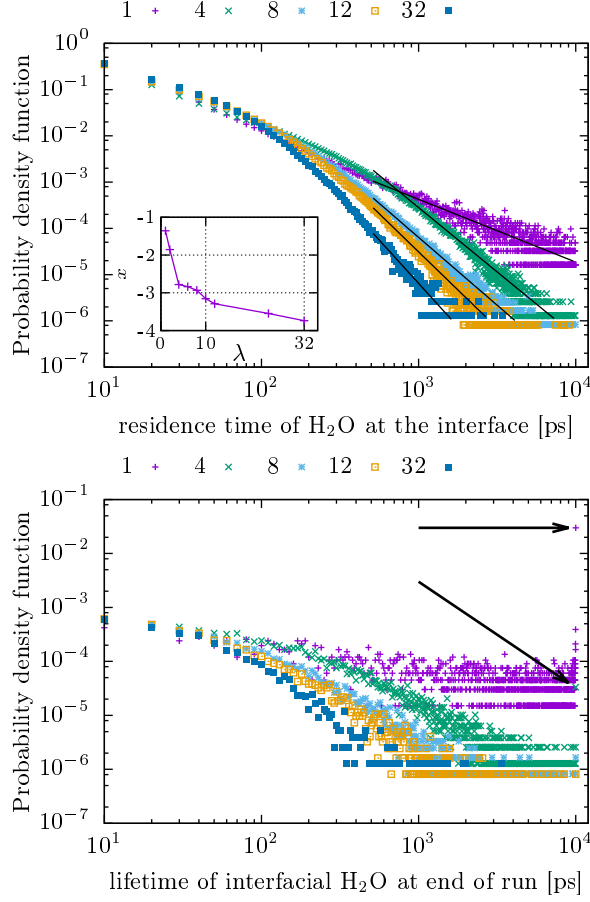
Figure 6.5: *Top:* Probability distributions of the residence times observed during the 10 ns simulation run. The long-time behaviour is reminiscent of a power-law, and in the inset we plot the exponent of power-law fits. *Bottom:* Distribution of the residence times of the water molecules present at the interface a the end of the simulation run. The black arrow points to the long-time bump in the distribution that is particularly visible at low hydration ($\lambda \leq 6$). For clarity, we show only the results for $\lambda = 1, 4, 8, 12$ and 32.

within the first hydration layer of the sulfonated groups as

$$C_1(t_n) = \frac{1}{1 - n/N_s} \frac{\left\langle \sum_{s=0}^{N_s-1-n}(1 - p_{i,n+s}) \prod_{m=s}^{n+s-1} p_{i,m} \right\rangle_i}{\left\langle \sum_{s=0}^{N_s-1} p_{i,s} \right\rangle_i}. \tag{6.4}$$

Here, $\langle \rangle_i$ is the average over all water molecules $i = 1, \ldots, N_w$, and $t_n = t_{n+s} - t_s$.

Note that the product at the numerator is non-zero only if particle i survives at the interface at all times $t_s \leq t < t_{n+s}$, subsequently detaching exactly at t_{n+s}. We plot our data in the main panel of Fig. 6.6 as symbols, at the indicated values of λ.

Already by visual inspection it is clear that the typical lifetime of water molecules at the interface increases by lowering λ. Interestingly, we also find that two different mechanisms seem to concur at the relaxation on different time scales. Our data can be represented at all hydrations by a modified exponential, $C_1(t) \propto e^{-(t/\tau_s)^{\beta_s}}$ at short times, crossing-over to a power-law behaviour, $C_1(t) \propto t^{-\alpha_s}$, at longer times. Note that the cross-over point depends on λ. The fitting curves are shown as solid and dashed lines in Fig. 6.6.

In our understanding, the faster process is associated to the exchange mechanism of water molecules which detach from the interface and transit in higher-order hydration layers, on a (well-defined) typical time scale $\tau_s(\lambda)$. Indeed, the functional form used is suggested by an analogy with the decay of a subset (population) of a given system, characterised by some particular feature. Similarly to the case of radioactive decay, for instance, if the probability to disintegrate (or to detach from the interface in our case) is uniform, then $C_1(t) \approx e^{-t/\tau_s}$. In contrast, if the probability to detach is not a constant, then $C_1(t)$ can relax both faster or slower than a simple exponential. The mildest deviation from the pure exponential is $C_1(t) \approx e^{-(t/\tau_s)^{\beta_s}}$, with the exponent β_s quantifying the degree of the deviation: for $\beta_s < 1$ (stretched) the decay is slower than exponential, faster for $\beta_s > 1$ (compressed). In more extreme cases, scale free power-law behaviour have also been observed [64, 65].

Our analysis suggests that τ_s increases from 60 to 22000 ps as the hydration λ decreases from 32 to 1 (see Fig. 6.8), meaning that the exchange mechanism at the interface is activated by hydration. Also, we have found that β_s varies from 0.6 at $\lambda = 1$ to 0.8 at $\lambda = 32$ (inset of Fig. 6.6). These observations therefore seem to demonstrate that hydration controls both typical time-scale and statistical features of the postulated exchange mechanism. In addition, the self-similar behaviour observed at longer times clearly is the echo of the power-law tails of the static distribution functions of the $\{p_{i,n}\}$ of Fig. 6.5. It is natural to expect that this relaxation stems from trapping at the interface of water molecules on extremely extended time scales. This would also directly allow to identify interfaces as the main source of water sub-diffusion, rationalising this mechanism in terms of a CTRW approach.

It is not possible, however, to associate a well-defined time scale to this dynamics in terms of Eq. (6.4). Indeed, in order to highlight the dynamics most controlled by the interface, beyond the exchange process quantified above, one should lift the excessive constraint of water molecules *uninterruptedly* bounded to the interface during the time window t_n implicit in that definition. We therefore define the time
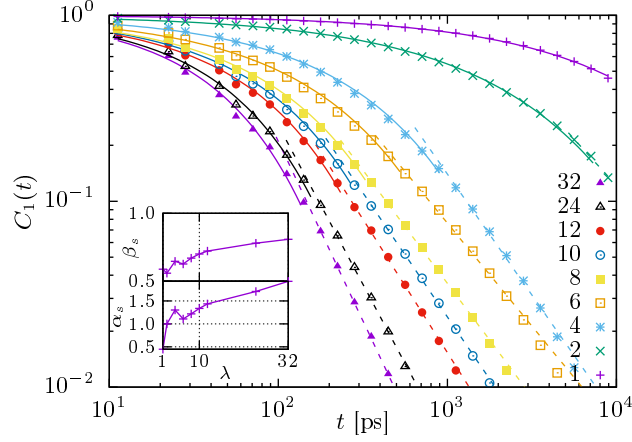
Figure 6.6: *Main panel:* Survival-time correlation functions of water at the interface, $C_1(t)$, computed via Eq. (6.4), at the indicated values of λ. *Insets:* λ-dependence of the two fitting parameters β_s and α_s, obtained by representing the data with a modified exponential decay at short-times and a long-time power-law. The rationale for the fits shown as solid lines in the main panel is discussed in details in the main text.

autocorrelation function of $\{p_{i,n}\}$,

$$C_2(t_n) = \frac{\left\langle \sum_{s=0}^{N_s-1-n} p_{i,s+n}p_{i,s} \right\rangle_i}{\left\langle \sum_{s=0}^{N_s-1} p_{i,s}^2 \right\rangle_i}. \qquad (6.5)$$

At variance with the case of Eq. (6.4), with this definition water molecules that are at the interface at times t_s and t_{s+n} contribute to $C_2(t_n)$, notwithstanding their faith between t_s and t_{s+n}, and at t_{s+n+1}. This function therefore still selects molecules that detach from the interface, but also those that return to the interface, at some later time after leaving. We expect, in general, that this dynamics takes place on time scales comparable to or longer than τ_s. We plot our data as symbols in Fig. 6.7, at the indicated values of λ.

The data show a two-relaxation pattern, that we describe as,

$$C_2(t) = c\,e^{-(t/\tau_i)^{\beta_i}} + (1-c)\,e^{-(t/\tau_\infty)^{\beta_\infty}}, \qquad (6.6)$$

and plot as solid lines in the same figure. We consider here two points. First, the initial decay of $C_2(t)$ takes place on a quite large range of time scales τ_i, ranging from $\simeq 100$ ps at $\lambda = 32$ to $\simeq 2$ ns at $\lambda = 1$. This quantifies dynamics at the interface, as we will see below. Second, the functions exhibit an abrupt singular
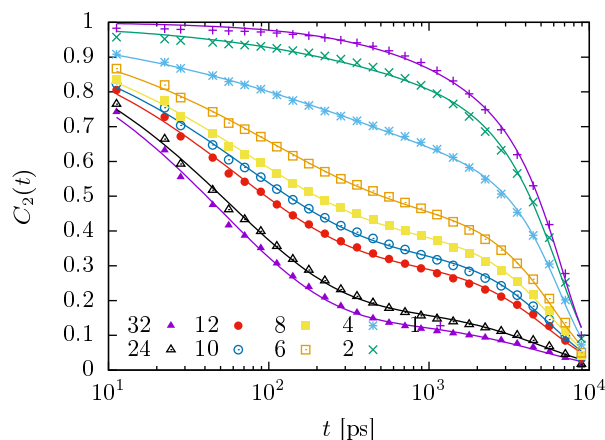
Figure 6.7: Time autocorrelation functions of $\{p_{i,n}\}$ (symbols), computed via Eq. (6.5), at the indicated values of λ. The continuous lines are the results of the fits to our data according to Eq. (6.6). A comprehensive discussion of these results is provided in the main text.

behaviour as t approaches the total time window of our simulation, τ_{max}, and this cutoff is more pronounced at lower hydrations. We indicate this limit time scale as τ_∞, which characterises molecules that are permanently attached to the interface on the time scale of our simulation.

6.6 Discussion

We now describe the implications of the data reported in the previous Section, and provide a consistent unique picture of our observations. From the analysis above, we have been able to extract five time-scales relevant for the confined dynamics of the water molecules. In particular, τ_D and τ_{SD} are associated to the relaxation of the intermediate scattering function, τ_s characterises the survival-time correlation function $C_1(t)$, τ_i and τ_∞ have been determined from the binary presence autocorrelation function $C_2(t)$. We plot all data as a function of the hydration level λ in the top panel of Fig. 6.8.

We see that the long-time component of the autocorrelation of the binary presence, τ_∞, is λ-independent, and of the order of the total simulation time. We associate this time-scale to the water molecules that stay in the interfacial layer for times that are compatible with the duration of the entire simulation run. As already anticipated, this is an artificial feature which originates from arbitrarily fixing a bound from above on the available observation time. As a consequence,
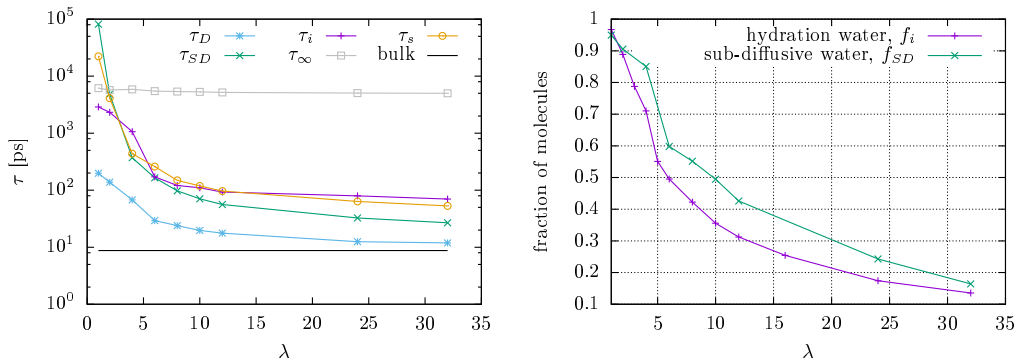
Figure 6.8: *Left:* λ-dependence of the relevant time-scales associated to the dynamics of the confined water molecules: τ_D and $\tau_S D$ are associated to the relaxation of the intermediate scattering function, τ_s characterises the survival-time correlation function, $C_1(t)$, τ_i and τ_∞ have been determined from the binary presence autocorrelation function, $C_2(t)$. A comprehensive discussion of these data is included in the main text. *Right:* Static fraction of water molecules residing at the interface, f_i, together with the dynamic fraction of sub-diffusive molecules, f_{SD}. The two data-sets coincides at low hydration. This point, together with the discrepancy at high-λ are described in details in the main text.

all dynamics on time scales larger than τ_∞ cannot be probed in equilibrium in our simulation.

Interestingly, the time-scales τ_i of the short-time component of $C_2(t)$ and τ_s of the initial decay of $C_1(t)$ are, at variance, strongly reduced as the water content increases. We can associate these relaxations to an exchange mechanism between the interfacial region and the rest of the aqueous domains, which is activated by the increase of the hydration. This idea is strongly supported by a surprising observation: τ_i and τ_s are very similar, especially at low-λ, to the time scale τ_{SD} that we extracted from the $F_s(q^*,t)$, and associated with the sub-diffusive fraction of water molecules. These therefore seem to be those pertaining to the population with a dynamics of primary interface-dominated character.

An other observation additionally strengthen our picture. In Fig. 6.8 (right) we show two quantities: the *static* fraction over the total number of water molecules lying at the interface, f_i, which we obtain by simply counting the number of molecules comprised in the hydration layer; and the *dynamic* fraction of sub-diffusive particles, f_{SD}, obtained from Eq. (6.3). The two data sets exhibit very similar variation on the whole hydration range, and the two curves actually coincide at the lowest hydration ranges, $\lambda \leq 2$. At higher hydration levels, f_{SD} is close to, although always higher than, f_i. We infer from the similarities of the typical time scales and
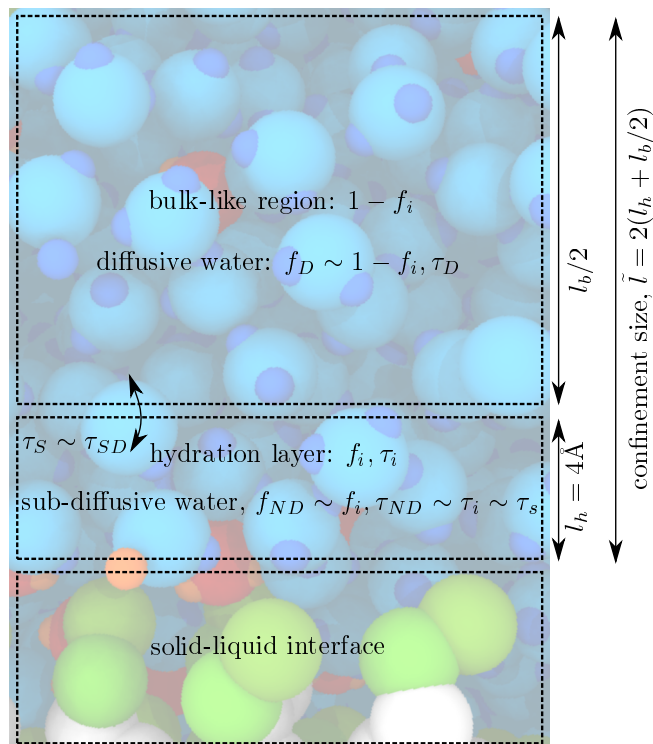
82

Figure 6.9: Schematic overview of the interplay between the structure of the surfactant phase and the transport properties of the confined water molecules. This sketch complements the detailed discussion contained in the main text.

associated fractions (over the total number) that interfacial and sub-diffusive populations coincide, or at least that the sub-diffusive population is a superset of the interfacial one.

We propose a schematic overview of our discussion in Fig. 6.9, where we partition into three main areas the surfactant phase environment, with both the confining matrix and the complementary space available for transport in the ionic channel, of typical size $\tilde{l}$: *i)* the solid-like interface (bottom), which comprises the surfactant hydrophilic heads; *ii)* the hydration layer (centre), that covers the interface and comprises all water molecules within $r_c = 4$ Å from the the nearest surfactant head; and *iii)* the bulk region (top) consisting of all remaining water molecules and extending over a typical length scale l_b, which depends on λ. Obviously, $\tilde{l} = 2(l_h + l_b/2)$.

The hydration layer is characterised by the fraction of molecules it comprises, f_i, together with the characteristic time of their interface-dominated dynamics, τ_i.
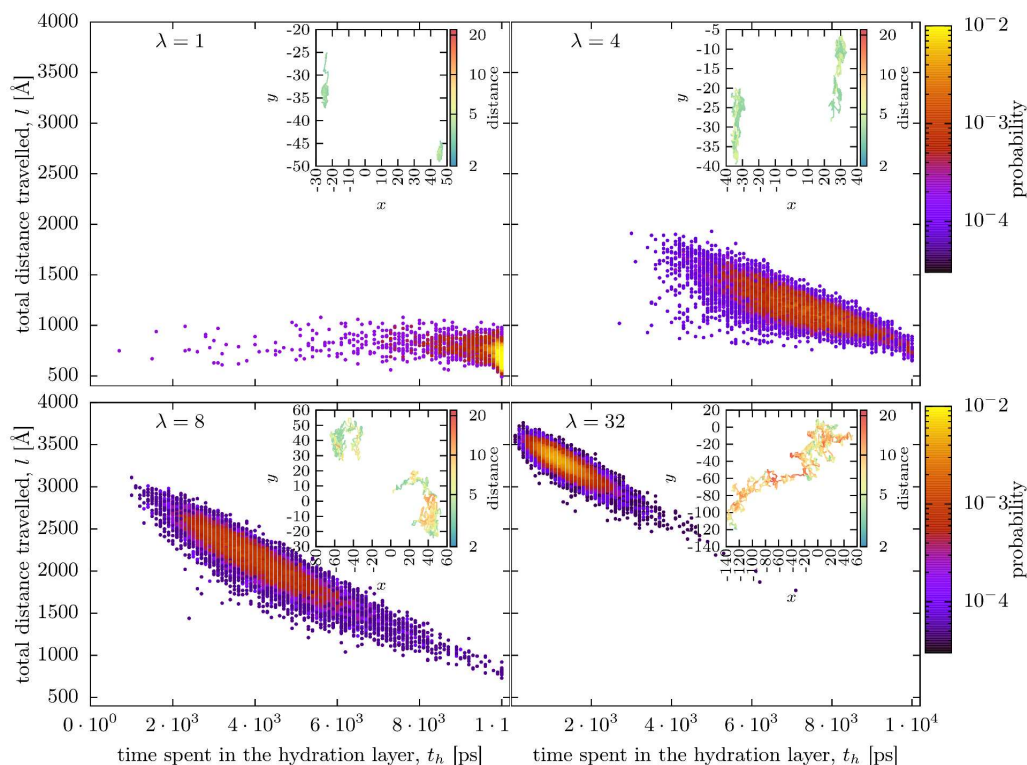
Figure 6.10: Joint probability distribution of the total displacement, l, of water molecules on the entire time scale of the run, $\tau_{\max}$, and the total time, t_h, they have spent (even discontinuously) in the hydration layer of a surfactant head, on the same time window. The probability is represented as colour maps, for the indicated values of λ: yellow indicates high probability, indigo lower. In the insets we show the projection on the xy-plane of the trajectory followed by two molecules chosen at random at the corresponding λ, with the distance to the nearest surfactant head indicated by the displayed colour code.

The fraction of water at the interface coincides at low-λ (and has a very large overlap at high-λ) with the fraction of sub-diffusive water ($f_i \approx f_{SD}$), and one finds $\tau_i \approx \tau_{SD}$. The molecules at the boundary with the region extending beyond the first hydration shell and comprising the remaining fraction, $1 - f_i \approx f_D$, participate to the exchange process with the molecules pertaining to the bulk-like reservoir. This takes place on a time scale τ_s, which also correlates to the sub-diffusive time scale of the intermediate scattering function, with $\tau_s \approx \tau_{SD}$.

The sub-diffusive character of the mean-squared displacements (Fig. 6.2) also finds a clear rationalisation in this picture. $\langle r^2(t) \rangle$ grasps an average dynamics,

which results from a λ-dependent interplay of interface-dominated and bulk-like behaviour. The source of the observed sub-diffusion is trapping of water molecules at the interface, with a power-law distribution of trapping times, as demonstrated in Fig. 6.6. This breaks the validity of the central limit theorem in a fashion reminiscent of a continuous time random walk, immediately providing a rigorous justification of the observed non-linearity of $\langle r^2(t) \rangle$ at long times. Also note that in general $f_i \leq f_{SD}$, and at high hydrations (above $\lambda = 6$) τ_s and τ_i are slightly larger than τ_{SD}. This indicates that water molecules exiting the hydration shell retain a certain degree of sub-diffusivity, with this anomalous character progressively disappearing when moving away from the interface.

To further clarify this point, we have quantified the correlation between the total displacement, $l_i = \sum_{n=1}^{N_s-1} |\mathbf{r_i}(t_n) - \mathbf{r_i}(t_n - 1)|$, of water molecule i on the entire time scale of the run ($\tau_{\max} \simeq 10$ ns) and the total time, t_i^h, it has spent (even discontinuously) in the hydration layer of a surfactant head, on the same time window. In Fig. 6.10 we show the joint probability distributions of these two quantities as colour maps, for the indicated values of λ; yellow indicates high probability, indigo lower. We observe a clear trend as the hydration increases.

At very low water content ($\lambda = 1$), almost all water molecules remain in the hydration layer for most of the duration of the simulation run ($t_h \approx \tau_{\max}$), and the total distance travelled does not strongly depend on the time spent at the interface, fluctuating around $l \approx 750$ Å. In the inset we show the projection on the xy-plane of the trajectory followed by two molecules chosen at random, with the distance from the nearest surfactant head indicated by the displayed colour code. The motion is clearly very constrained (probably bi-dimensional) in both cases, with a very limited portion of space explored. For $\lambda = 4$ and 8, however, the probability to observe very high values of t_h progressively decreases, while the distribution of t_h becomes wider. This effect is accompanied by longer l travelled at shorter t_h, with a degree of variation increasing with λ, as confirmed by the data in the insets. At $\lambda = 32$, eventually, the probability accumulates in the high-l/low-t_h region, indicating that practically all molecules transit between the interface and the bulk-like region (the trajectory of one molecule is shown in the inset, and clearly shows segments of high-speed travel far from the interface, and "sticky" regions that trap the molecule).

The conclusion arising from the above arguments is that the picture based on two well-identified dynamical population, that fully accounts for the behaviour in the low-λ regime, must be modified at high water content, where we observe an increasing rate of the exchange mechanism and of the number of molecules participating to it. Indeed, it is not possible to account for the complex distributions of Fig. 6.10 in terms of an average τ_i only, and one should rather consider a λ-dependent set of populations, characterised by a distribution of τ_i (τ_{ND}).
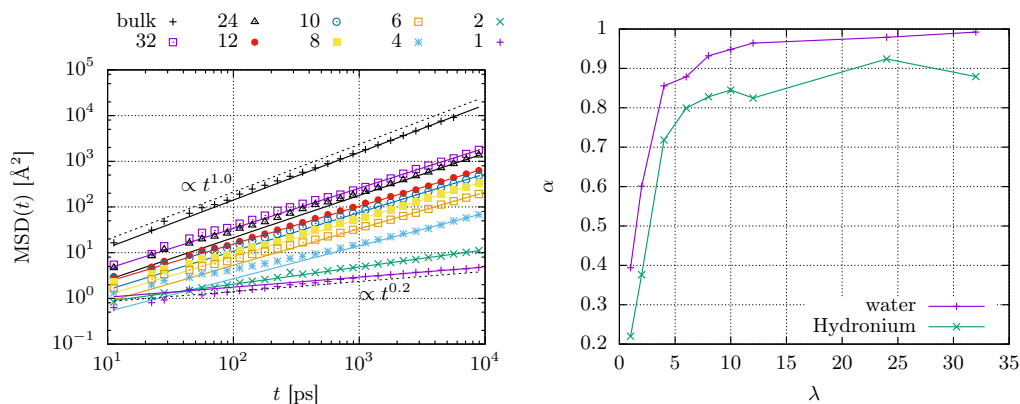
Figure 6.11: Mean squared displacement of hydronium ions. For comparison, the mean-squared displacement of bulk SPC/E water is also shown. Symbols indicate data points, and lines indicate the power-law fits, with the two labels indicating the exponents of the bulk water and most confined cases. On the right, we show the variation of the exponent as a function of the hydration. For reference, we also show the same data for water.

6.7 The case of the hydronium ions

We will now see that similar arguments can be developed for the case of the hydronium ions. Obviously, our model can only address the issue of vehicular transport because it lacks the quantum description necessary to the treatment of Grotthuss-type transport (see section 2.2). We already established from the analysis of figure 6.1 that the dynamics of the hydronium ions are always significantly slower. In the following, we give the details of our analysis of the transport of hydronium ions.

6.7.1 Evidence of subdiffusive behaviour of hydronium ions

We computed the mean-squared displacement of hydronium ions over the 10 nanoseconds long trajectories, which we show in figure 6.11 along with the associated values of the exponent obtained from the power-law fit of the MSD. For comparison, we also reported the values of the exponent for the water molecules that we obtained above. As can be seen from figure 6.11, the case of hydronium ions is very similar to that of water molecules: the transport is clearly subdiffusive, and the subdiffusive degree increases with the extent of confinement. The values of the exponents are always smaller than those of the exponent associated to the water molecules (see 6.11). This suggests that the subdiffusive behaviour is more pronounced in the case of hydronium ions.
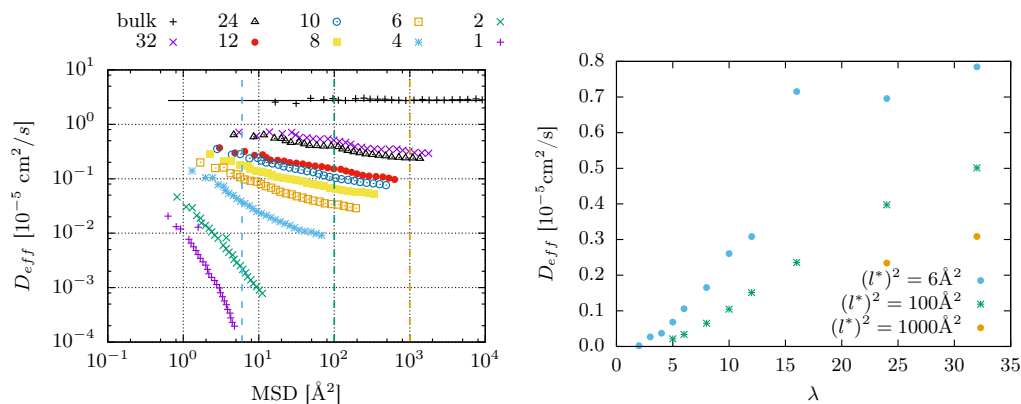
Figure 6.12: Effective diffusion coefficients of hydronium ions. For comparison, the effective diffusion coefficient of bulk SPC/E water is also shown. Data is presented as a function of the mean squared displacement.

In figure 6.12 (left), we show the MSD-dependent effective diffusion coefficient, D_{eff} (see equation 1.10). This data show that hydronium ions are also sub-diffusive, and that the sub-diffusive character progressively disappears as the hydration is increased. Similarly to the case of water, the effective diffusion coefficient is smaller when larger displacements are considered, due to the subdiffusive nature of hydronium transport. On the right panel of figure 6.12, we show the values of the effective diffusion coefficient corresponding to the (squared) displacements of 6,100 and 1000 $Å^2$. Note that because the transport of hydronium is slower than that of water, the value $MSD = 1000$ $Å^2$ is only observable at the highest hydration values. Once again, it is clear that the measurement length-scale significantly affects the value of the effective diffusion coefficient.

An observation is in order at this point: in the case of water, we were able to associate the values of the diffusion coefficient at 6 and 1000 $Å^2$ to experimental values obtained by QENS and NMR, respectively. We saw in chapter 3 that QENS experiments on ionomer membranes are able to discern between two populations of protons. In this case, part of the signal was attributed to the motion of hydronium ions (see figure 3.7 and [109]). It is important to note that we are able to discern two populations of protons because the characteristic time- and length-scales associated with these two populations are well separated in the QENS spectrum. In the case of NMR measurements, such distinction is not possible, and therefore NMR data represents an average of all protons, be they from water molecules or hydronium ions.

Unfortunately, the QENS analysis was not reproduced for surfactants, therefore we can not directly compare our values of the effective diffusion coefficient of hy-
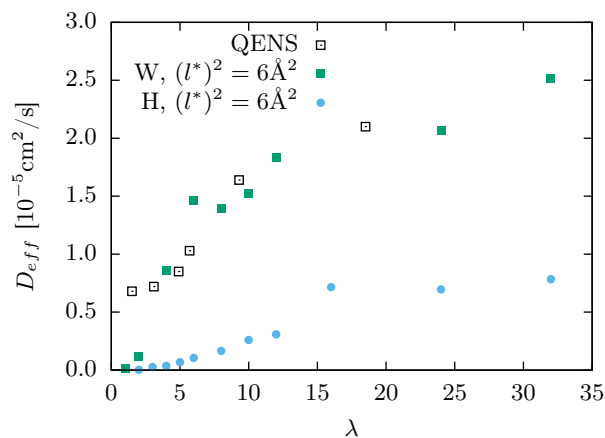
Figure 6.13: Effective diffusion coefficients of water and hydronium ions at a cutoff distance of 6Å^2. For comparison, the corresponding experimental values are also represented.

dronium with the experimental values. In figure 6.13, we report the experimental diffusion coefficient associated to water molecules in surfactants, together with our numerical values for the water and hydronium ions. We remark that at this scale, the effective diffusion coefficient of hydronium ions follows a similar trend as that of water. In contrast, its value is roughly five times smaller for the hydronium than in the case of water.

Following the same method that we developed for the case of water molecules (see above), we have computed the self intermediate scattering function for the hydronium ions for a value of $q = 0.7$ Å^{-1}. We show the result in figure 6.14 (top left), along with the fits which we performed as in the case of water. In the same figure, we show the exponent of the sub-diffusive fraction of water molecules (top right), the populations of diffusive and subdiffusive hydronium ions and water molecules (bottom left), and the characteristic times associated to these populations (bottom right).

We observe that the situation is close to that of water molecules: there exist two dynamical populations, whose characteristic times differ roughly by one order of magnitude. In addition, we observe that the diffusive (sub-diffusive) populations of water and hydronium are very close in the lamellar phase ($lambda \leq 5$), where almost all fluid particles are at the interface. Beyond this hydration ($\lambda \geq 6$), we saw (see chapter 5) that the hydration layer is filled, and additional molecules are placed in the "bulk-like" region. From this critical point, the fraction of sub-diffusive hydronium is significantly larger than that of subdiffusive water. Also, the fraction
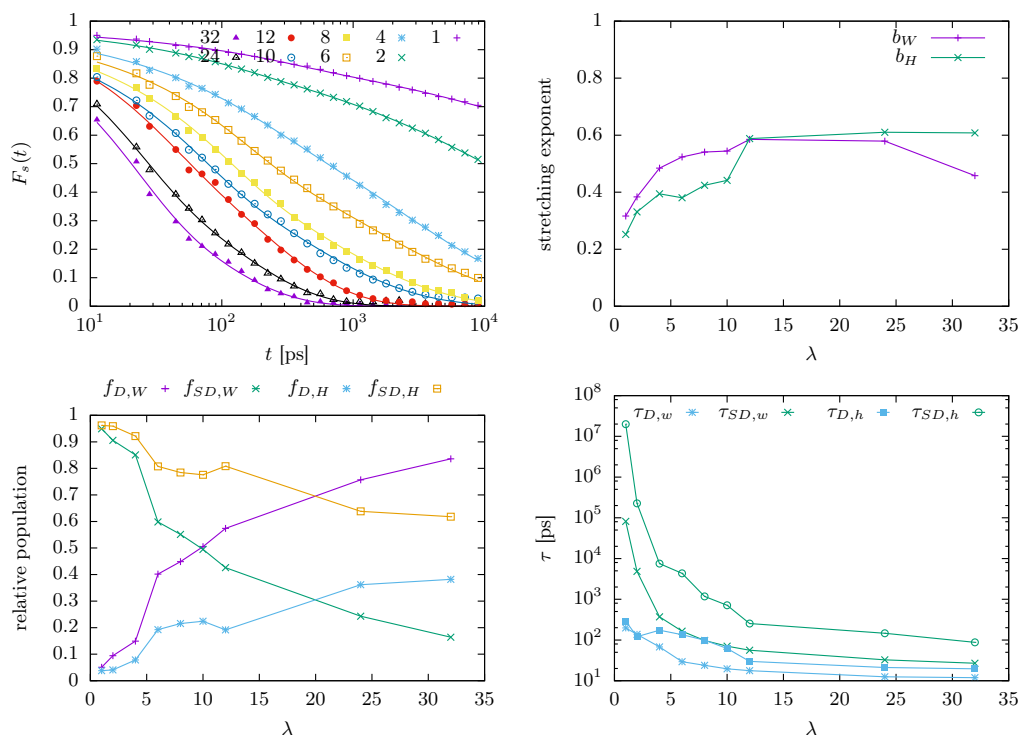
Figure 6.14: Top left:Self intermediate scattering function of the hydronium ions. Top right: Stretching exponent of the sub-diffusive contribution to F_s for water and hydronium ions. Bottom left: Relative populations of diffusive and sub-diffusive hydronium ions and water molecules. Bottom right: Characteristic times associated to the dynamics of the diffusive and sub-diffusive hydronium and water populations.

of subdiffusive hydronium is always greater than that of diffusive hydronium, while for water the diffusive fraction is dominant from $\lambda = 10$. Moreover, the time-scales are slower in the case of the hydronium (consistently with our analysis of figure 6.1). We attribute these differences to the additional charge carried by hydronium ions. Our hypothesis is that due to the Coulomb attraction between hydronium ions and the ionic head groups of the surfactants, the hydronium ions are trapped for significantly longer periods of time at the interface, which leads to a more pronounced subdiffusive character.

To support this hypothesis, we will now analyse the interfacial population of hydronium and the associated time-scales

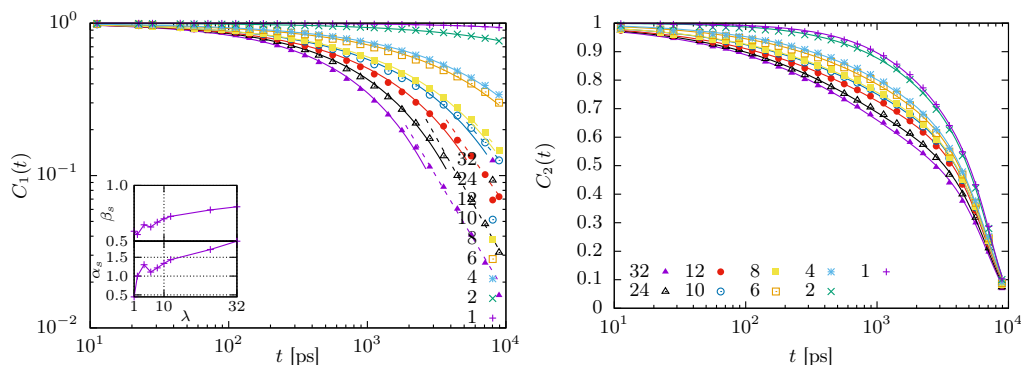Figure 6.15: *Left, Main panel:* Survival-time correlation functions of hydronium ions at the interface, $C_1(t)$, computed via Eq. (6.4), at the indicated values of λ. *Insets:* λ-dependence of the two fitting parameters β_s and α_s, obtained by representing the data with a modified exponential decay at short-times and a long-time power-law. The rationale for the fits shown as solid lines in the main panel is discussed in details in the main text. *Right:* Time autocorrelation functions of $\{p_{i,n}\}$ (symbols) for the hydronium ions, computed via Eq. (6.5), at the indicated values of λ. The continuous lines are the results of the fits to our data according to Eq. (6.6).

6.7.2 The interfacial population and its associated time-scales

Following a similar methodology as for the case of water, we computed the survival time correlation function of hydronium ions at the interface. We present our results in figure 6.15 (left), together with the results of the fits of the initial exponential decay and of the asymptotic power-law behaviour, which we performed similarly to the case of water. We remark that the initial exponential regime persists for more extended periods of time compared to what we observed for water. We also computed the time autocorrelation function of the binary presence function, which we show in figure 6.15 (right), along with the resulting fits which we conducted as we did for water. As in the case of the survival-time correlation function, the main features are shifted toward longer times, and the separation between the two characteristic regimes that we observed in the case of water are not obvious in this case. Overall, these data support the above hypothesis, where the additional Coulomb attraction between hydronium ions and the confining matrix result in more extended trapping times (of the order of $100\times$ the trapping time of water at low hydration, and $10\times$ at high hydration), which enhances the subdiffusion for the hydronium. This observation is compatible with the conclusion of the study of mobility of water in the vicinity of hydrophilic and hydrophobic domains in the
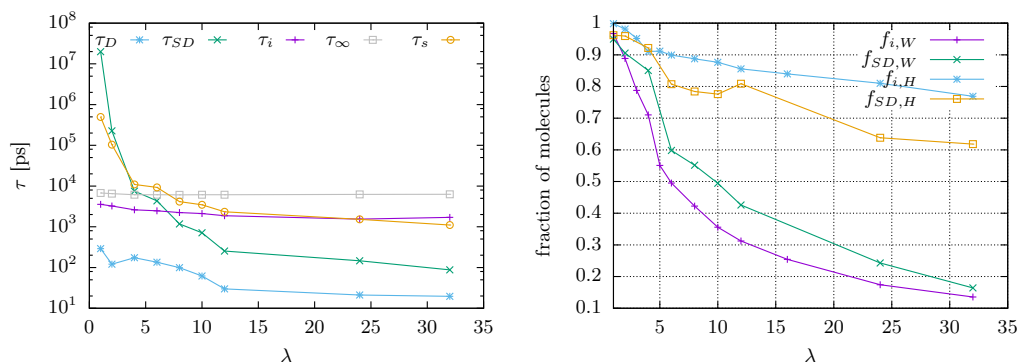
Figure 6.16: Left:Summary of the characteristic time-scales associated to hydronium ions. Right: Comparison between the populations diffusive and interfacial populations of hydronium ions.

Nafion ionomer [168], that found that the nature of the interaction between the confining matrix and the fluid significantly influences the transport properties. In particular, strong attractive forces reduces the mobility of the fluid, while strong repulsive (hydrophobic) interaction enhances mobility of the fluid [168].

In figure 6.16 (left), we summarise all the characteristic times associated with hydronium ions. Similarly to figure 6.8, we observe that the time scales associated to the dynamical populations are well separated, with the sub-diffusive population being much slower than the diffusive one. The time scales associated to the interfacial hydronium populations follow the behaviour of that of the sub-diffusive populations, as was the case with interfacial water molecules. We recall that while the overall behaviour of water and hydronium ions is similar, the characteristic time scales associated to the dynamics of hydronium are always longer than those associated with water.

In figure 6.16 (right), we show a comparative summary of the interfacial and sub-diffusive populations of water and hydronium ions. As in the case of water, there is a clear correlation between the interfacial and sub-diffusive populations of hydronium ions. However, note that the fraction of interfacial hydronium ions is higher than that of sub-diffusive hydronium ions, in contrast with our findings for water molecules. We attribute this difference to the enhanced interaction between the hydronium and the charged interface.

Overall, as in the case of water, the analysis of the transport properties and of the dynamics of the interfacial population of hydronium ions suggest that these two populations strongly overlap. The fraction of interfacial/subdiffusive hydronium population is however higher than that of water. We attribute this more pronounced subdiffusive behaviour to the additional Coulombic attraction between

the positively charged hydronium ions and the negatively charged surfactant heads.

6.8 Conclusions on the dynamics in hydrated surfactant systems

In this chapter, we have followed numerically the dynamics of water molecules and hydronium ions constrained in self-organised ionic surfactant phases. By varying the water content, we have considered an extended range of soft mobile confining environments, characterised by variable confining scales and topological properties of the generated hydrophilic/hydrophobic interfaces. These two features contribute in a highly non-trivial fashion to transport of the adsorbed fluid, that we have managed to characterise in terms of a space-dependent dynamical behaviour.

More in details, we have demonstrated that both the observed sub-diffusive character of the average mean-squared displacements, which is increased by decreasing the length scale of the confinement, and the details of the relaxation of the intermediate scattering function, can be rationalised in terms of two dynamical populations. The first is predominantly interface-dominated, with a marked non-diffusive behaviour, the second has a bulk-like character. The average dynamical behaviour of the adsorbed fluid is primarily determined by the exchange mechanism between the two dynamical groups, whose precise features depend on the water content. This simple picture allows for a complete quantitative characterisation of dynamics at low-λ, while at high-λ we have proposed that an entire λ-dependent set of populations must be considered to obtain the same accuracy.

We have show that the sub-diffusive behaviour of hydronium is more pronounced than that of water, which we explained by the following argument. Due to the charge of the ions, more ions are within the first hydration shell of the surfactant heads (as seen from the fraction of interfacial/sub-diffusive hydronium), and the trapping times are longer (as shown with the slow-decaying interfacial correlation functions). This reinforces the sub-diffusivity of ions (as seen from the exponents of the self intermediate scattering function for example). Also, the fraction of sub-diffusive hydronium ions is always dominant, while from $\lambda = 10$ the majority of water molecules belong to the "diffusive" population. It is important to recall that our model can only address the issue of the vehicular transport of protons, and therefore that no conclusion can be drawn with respect to the structural component of proton transport from our simulations.

Chapter 7

Perspectives: From surfactants to polymers

We saw in the previous chapters how our model of ionic surfactants and water can be used to clarify in a very general fashion the behaviour of water confined in soft materials. As already mentioned, we designed this model to be modular, the idea being that it should be possible to up-scale this basic model to study more complex systems. In particular, we can build on our model of surfactants to produce a model of ionic polymers, with physical properties close to that of ionomers: a highly hydrophobic backbone decorated with hydrophobic side chains terminated by hydrophilic acid groups. This allows us to observe the effect of the tortuosity introduced by the addition of the polymer backbone.

7.1 Aims

The existing literature has already established that hydrated ionomers are inherently disordered (see the chapter 3 dedicated to the literature about ionomers). In addition, the nanostructure of these materials is known to swell upon hydration, which also alters the tortuosity and connectivity of ionic domains. Recall that the interest for these materials in fuel cells applications stems from their ability to transport protons between the electrodes. Knowledge of the transport properties is crucial, and in particular the issue of the *nature* of the transport processes is key. As we saw (see chapter 3), most experimental studies assume diffusive transport. However, based on results of infrared studies, some work point out the non-Fickian behaviour of water in Nafion [169].

At the best of our knowledge, no numerical study tackled the problem of the nature of the vehicular transport processes in hydrated ionomers. Instead, we saw

that existing studies rely on the assumption of diffusive vehicular transport . In this work we will use our model to clarify this particular area.

In the following, we expose the procedure we use to model the polymer. We will then present our study about the nature of transport processes in hydrated ionomers. We will also present results concerning the structural and dynamical properties of our model of polymer membranes doped with surfactants.

7.2   Model of ionomers

We wrote a general code that can generate the topology of ionomers with arbitrary side-chain spacing and length as well as arbitrary polymer length. We can also generate mixtures of polymers, surfactants and water to study the effect of doping on the structure and dynamics of the system. The backbone and side chains of the polymers are made of CF_2 beads, as is that of the surfactants. We attribute a distinct atom type to the CF_2 beads of surfactants, backbone, and side-chains, which we denote by the suffixes CF_{2BB}, CF_{2S} and CF_{2SC}, respectively. We employ a similar classification scheme for the S and O_3 beads of the surfactants and side-chains. This allows us to easily distinguish between each atom type during analysis, and to adjust the properties of each atom type independently. In the following, we have chosen to adopt the same force field for every CF_2, O_3, and S beads, for simplicity. The polymers are generated randomly according to a self avoiding walk, so as to reduce the initial excess of Van Der Waals energy in the system.

As for the case of surfactants and water, the hydration is adjustable via the λ parameter. Because we now introduce materials of different equivalent weights, the hydration λ is not necessary the best indicator of the amount of water in the system. Indeed, at the same hydration, the volume and mass fractions of water a in a material of low equivalent weight will be higher than those in materials of high equivalent weights. For this reason, we also characterise our samples with the fraction of water mass (see equation 7.2 for more details).

7.3   Simulation protocol

We generated polymers with $\Delta = 14$ CF_2 monomers between each side-chains, and $N_{SC} = 100$ side-chains per polymer. This spacing between side-chains results in an equivalent weight of 1080 g/eq, a value that is close to the commonly studied Nafion 212 which equivalent weight is 1100 g/eq. The side chains are modelled with $(CF_2)_6 SO_3^-$ surfactants, grafted on every 14th backbone monomers.

We dope the polymers with $(CF_2)_8 SO_3^-$ surfactants, of equivalent weight ~ 500 g/eq. We generated configurations with doping ratios of $x = 0, 0.7$, and 2.1 surfactants per side-chain. This allows us to study the two limit cases mentioned above
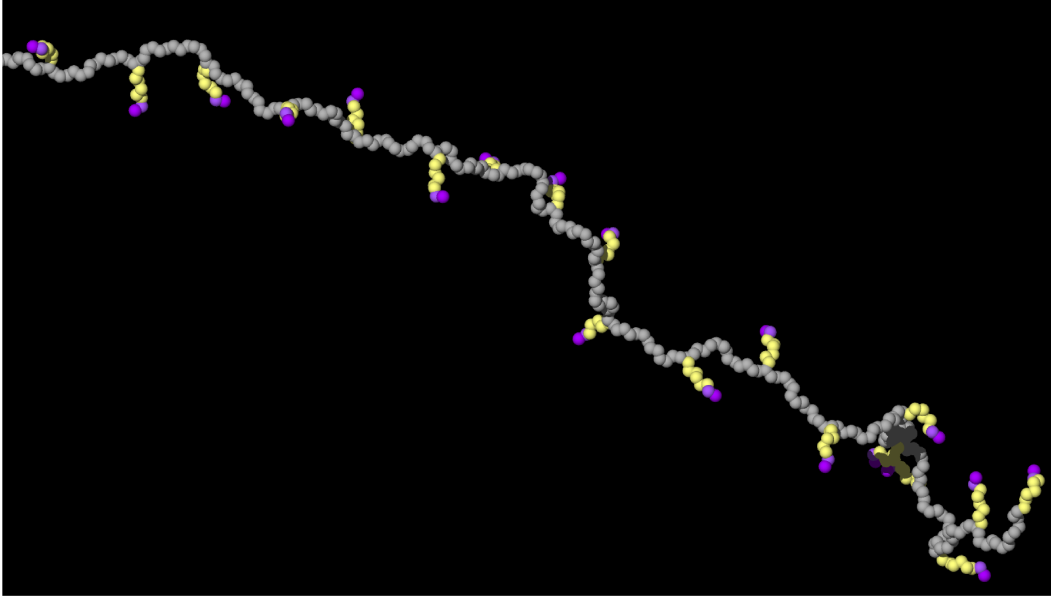
Figure 7.1: Portion of a single polymer chain. The backbone is shown in grey, with the side chains heads shown in purple and side chains tails shown in yellow.

(surfactant- and polymer-dominated), as well as an intermediate configuration. We initialised the simulations at water contents in a range similar to our study of hydrated surfactants (see chapter 5).

Comparison between experiments on surfactants and PFSA materials shows that the relevant variable is the average water channel size in the more confined states, and the water volume or mass fraction at higher water contents[119]. However, we have no way of determining *a priori* the size of water channels, and due to the high computational cost of equilibration it was impossible to proceed by trial and error.

The water mass ratio c is defined as:

$$c = \frac{(1+x)(\lambda M_{\mathrm{H_2O}} + M_{\mathrm{H_3O^+}})}{(1+x)(\lambda M_{\mathrm{H_2O}} + M_{\mathrm{H_3O^+}}) + M_{SC} + x \cdot M_S + \Delta \cdot M_{\mathrm{CF_2}}}, \qquad (7.1)$$

where M_α refers to the mass of an object α. The hydration level λ is defined as:

$$\lambda = \frac{c}{1-c} \frac{M_{SC} + x \cdot M_S + \Delta \cdot M_{\mathrm{CF_2}}}{(1+x)M_{\mathrm{H_2O}}} + \frac{M_{\mathrm{H_3O^+}}}{M_{\mathrm{H_2O}}}. \qquad (7.2)$$

We used this formula to determine the parameters of the sample. We summarise these parameters in table 7.1.

water mass ratio c	Doping $x = N_S/N_{SC}$			surfactant water mass ratio c	λ
	0	0.7	2.1		
0.06	2.82	1.95	1.38	0.07	1
0.09	4.93	3.57	2.70	0.11	2
0.16	10.4	7.81	6.12	0.17	4
0.24	17.9	13.6	10.8	0.22	6
0.36	32.7	25.0	20.0	0.27	8
				0.31	10
				0.35	12
				0.41	16
				0.51	24
				0.58	32

Table 7.1: Left: Parameters used for generating the initial condition of the simulations: to achieve similar volume-fractions of water across all doping parameters, we generated the samples at equal water mass ratios using equation 7.2. Right: For reference, we add recall the hydrations of the surfactant samples which we studied in chapter 5, along with the associated values of the water mass ratio.

We used simulation parameters similar to those used for the surfactant-water mixtures (see the previous chapter). The first task is too remove the excess Van der Waals energy. To do so, we perform a series of 100 runs of 100 femtosecond each, with the maximum displacement of an atom in a femtosecond capped at 1Å. Between each run, we re-sample the velocities from a 350 K Maxwell-Boltzmann distribution.

The next step is to allow for long-range reordering of the atoms. We remarked that due to the additional geometrical constraints imposed by the addition of the polymer backbone, the self assembly process is slower than in the case of surfactant-water mixtures. For this reason, we perform a 1 ns run in the 350 K NPT ensemble to accelerate the re-arrangement process, followed by a 10ns run in the 300K NPT ensemble, and at the end of this procedure we observe that all thermodynamical quantities are roughly constant. We re-use the final configuration for another NPT run, and we save the coordinates of atoms every 10 ps for later analysis.

7.4   The ionomer

In figure 7.2 we show typical snapshots of the equilibrated simulation boxes. We remark that these system phase separate, and that increasing the hydration increases the size and the connectivity of ionic domains. However, contrary to the case of
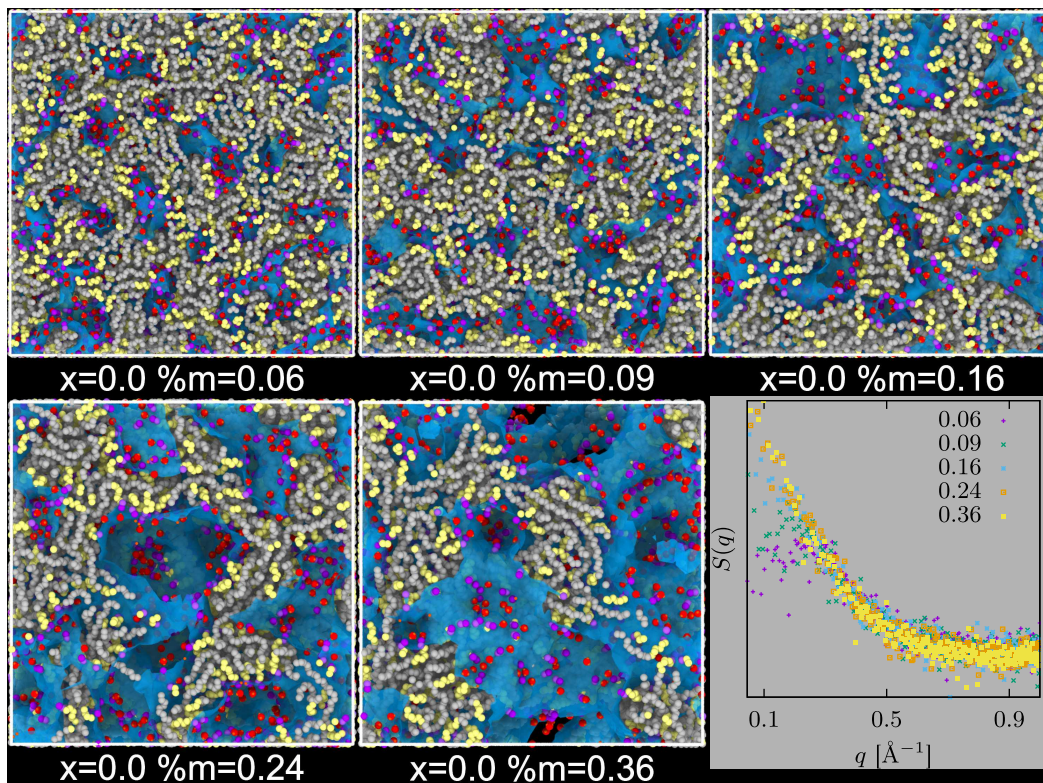
Figure 7.2: Snapshots of the equilibrated systems of hydrated ionomers that we generated. On the bottom right, we show the neutron static structure factor computed from these samples.

hydrated surfactants, a high degree of spatial disorder remains even at low hydration levels. This is consistent with experiments and previously reported results of numerical simulations [88].

As a result of the more disordered nanostructure, the features of the static structure factor (figure 7.2) are not well defined, therefore we will not use these in our analysis. Instead, we will characterise the structure using the width of the ionic domains l, computed from the distribution of distances of water molecules from the nearest hydrophilic site. In figure 7.3 we show the width of the fluid channel l both as a function of the hydration λ and as a function of the water mass ratio c. Interestingly, l is similar in both systems as a function of the hydration, but when considering equivalent water mass ratios c the ionic channels are wider in the polymers than in the surfactant. Moreover, we do not observe abrupt changes in width of fluid channels in the case of the polymer, which indicates that there is
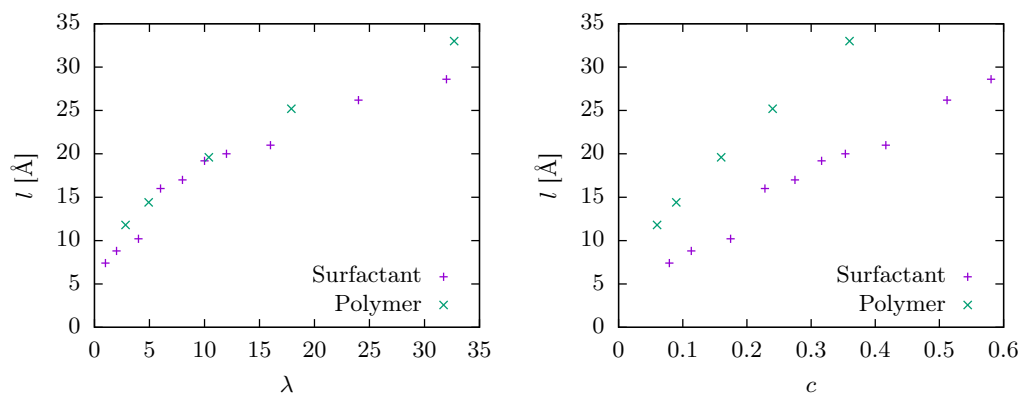
Figure 7.3: Width of the fluid channels l, measured as in chapter 5 from the distribution of distances of water molecules from the nearest hydrophilic site. Left: l is shown as a function of the hydration λ. Right: l is shown as a function of the water mass ratio c.

no sudden phase transition as in the case of the surfactants. Instead, these data support a model of smooth swelling of a disordered media.

In short, as in previous numerical and experimental studies, we observe that hydrated polymer samples are highly disordered. At comparable hydration levels, the width of the ionic channels in the polymer is similar to that in the surfactants. This supports the idea that surfactants are a good model system for the more complicated polymer samples. We will now focus on expliciting the nature of the transport process in these systems.

7.4.1   Nature of the transport processes in hydrated ionomers

We reproduced the analysis of the mean squared displacement that we introduced in the chapter about our simulations on hydrated ionic surfactants. In figure 7.4, we show the mean squared displacement of water molecules (top left) and hydronium ions (top right) in hydrated ionomers, along the the power-law fits to the data. Similarly to the case of hydrated ionic surfactants, we observe that the mean squared displacements are increasingly sub-linear as the hydration is decreased. We also note that the mean squared displacements tend to deviate from the power-law behaviour at short times (under 1 ns). In figure 7.4 (bottom), we show the associated effective diffusion coefficients of water (left), and hydronium (right). As in the case of hydrated surfactants, these coefficients decrease when the measurement distance is increased, due to subdiffusion. Also, the effective diffusion coefficients of hydronium ions are roughly 10 times larger than those of water molecules.

In figure 7.5, we show the exponents of the power laws, as extracted from the fits to the data. Interestingly, we observe that at comparable hydration λ, the exponents for water and hydronium ions are similar in the case of polymer phases, while in the case of surfactant phases the hydronium ions were always more sub-diffusive than water molecules. We suspect this could be attributed to the lower density of charges at the interface, which could reduce the affinity, and therefore the trapping times, of the hydronium ions with the interface. An interesting crossover appears between the low- and the high-water content limit. In the interface-dominated lamellar phase ($\lambda < 6$), the exponents are similar in the λ representation (see figure 7.5, left). In the bulk-dominated high hydration regime ($c > 0.2$), the exponent for the polymer is very similar to that of water in the surfactant phase at similar water mass ratio (see figure 7.5, right). A similar observation can be made when comparing the effective diffusion coefficients (for example, we have represented the values for water, $D_{eff}(MSD = 10 \text{ Å}^2)$ in figure 7.6). From figure 7.6, we find that $D_{eff}(\lambda)$ takes similar values in the polymers and the surfactants for $\lambda \leq 5$, and $D_{eff}(c)$ takes similar values in the polymers and the surfactants for $c \leq 0.2$. These similarities highlight two regimes. A first regime at low hydration ($\lambda < 6$), where interfacial effects dominate due to confinement. A second regime at $c > 0.2$ where the water content is so high that the fraction of hydration molecules is marginal, such that the details of the geometry of the interface have no influence on the transport properties. This is coherent with recent experimental findings in ionomers and surfactant [119]. In this study, QENS and PFG-NMR experiments highlighted the importance of the hydration variable.

7.5 More perspectives: ionomers doped with ionic surfactants

7.5.1 Effect of doping on structure

As an additional perspective, we have prepared several samples by doping polymers with varying amounts of surfactants. By varying the amount of surfactant added to the polymer, one can smoothly transition between the two limited cases of (i) the well ordered and controlled case of hydrated surfactant mixtures, and (ii) the disordered hydrated polymer mixtures. In short, doping the polymer with surfactants provides a way to modify the density of charges and the tortuosity of the resulting assemblies.

One open question on the matter is: "Where do surfactants go?". There are essentially two hypothesis concerning the answer to that question, (i) the surfactant mix with the polymer and sit between the side chains, and (ii) the surfactant and polymers are separate, with the surfactant forming lamellar defects in the polymer.
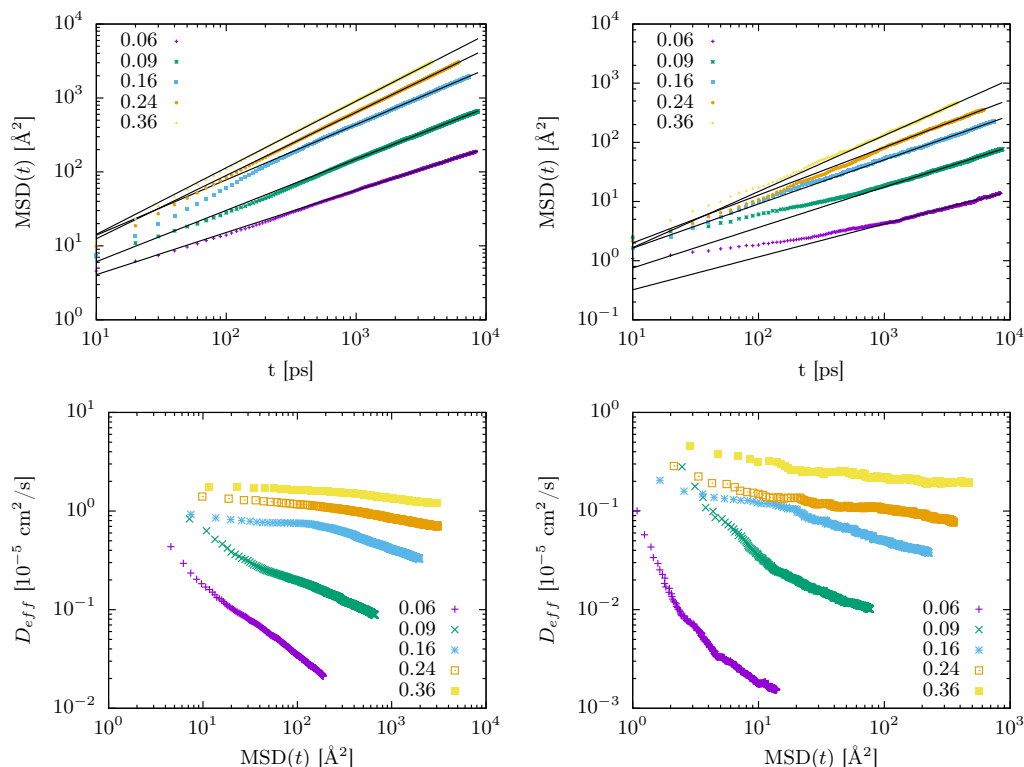
Figure 7.4: Mean squared displacement of water molecules (top left) and hydronium ions (top right) in hydrated ionomers. The points represent our data, and the lines represent the power-law fits to the data. We also show the corresponding effective diffusion coefficients of water molecules (bottom left) and hydronium ions (bottom right).

The importance of this question once again comes from the need of a model to analyse experimental data.

We have rendered the state of each configuration in the ovito visualisation software [170], and we present a few samples in figure 7.7. From visual inspection, it is clear that the vast majority of surfactants sit at the interface with the polymer backbone. Moreover, we remark that for lower water contents, the structure of the samples is locally lamellar.

In figure 7.8 we present the width of fluid channels for all our systems of polymers, as well as for the systems of surfactants. Interestingly, at low hydration ($\lambda \leq 6$) we observe very similar values across the samples. This is expected because within this hydration range all systems exhibit some degree of locally lamellar or-
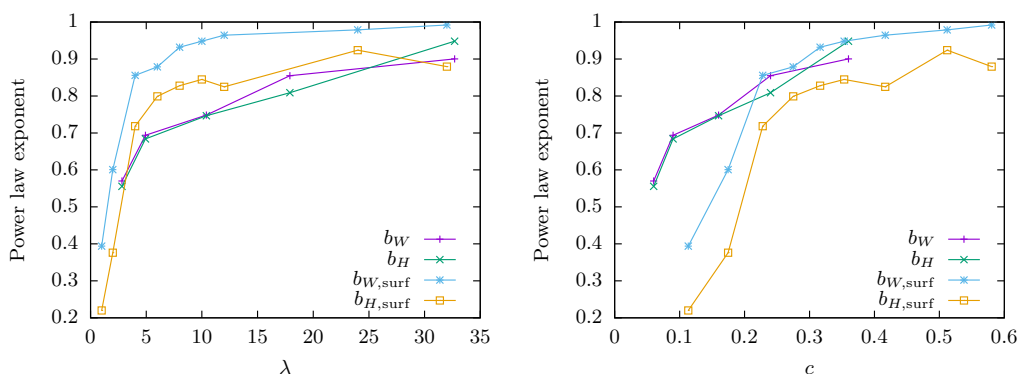
Figure 7.5: Power-law exponents resulting from the power-law fits to the mean squared displacement shown in figure 7.4. For comparison, we also represent the exponents obtained in a similar fashion for the systems of hydrated surfactants. Left: data shown as a function of the hydration λ. Right: data shown as a function of the water mass ratio c.
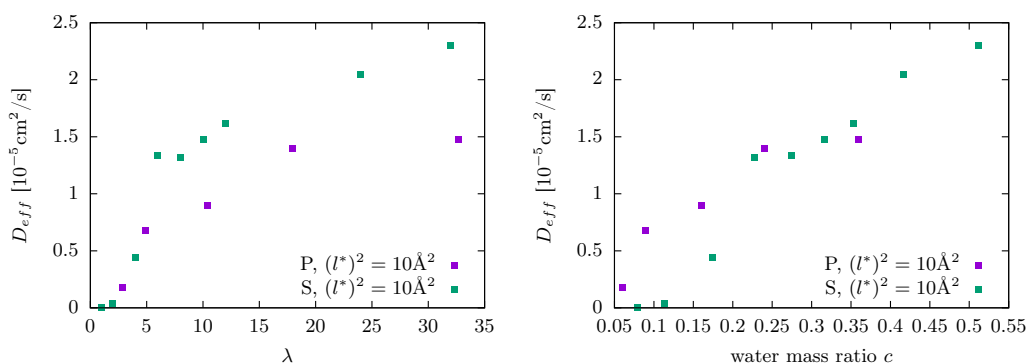
Figure 7.6: Effective diffusion coefficients of water molecules confined in assemblies of surfactants ("S" in the legend) and polymer ("P" in the legend), as a function of the hydration λ (left), and the ratio of water mass to total mass (right).

der. We also observe that for similar water mass ratio, the doped samples exhibit channel widths that are closer to pure surfactant samples. This is also expected: as we increase the doping, the sample becomes more and more like a pure surfactant-water mixture, where the lamellar structure is almost ideal and the width of the fluid channel is minimal.

The effect of doping the polymer with surfactants on the structure of the system can be quantified by computing the pair correlation function of backbone atoms

Figure 7.7:

Snapshots of the equilibrated systems, sorted by doping level x and hydration λ. The hydration is set so that the water/polymer volume ratio is constant for all samples. Surfactants atoms are shown in the same colours as in previous chapters, and the polymer is colour coded as in figure 7.1. Water atoms are hidden for clarity, and the blue surface represents the solid-liquid interface. We have enlarged the two lowest hydrations to highlight the structuring effect of doping. At these two hydrations, the tortuosity decreases and the connectivity increases as the doping is increased.

Figure 7.8: The width of the fluid channel computed for all available systems from the distribution of distances between water molecules and the nearest surfactant or side-chain head. Left: channel width as a function of the hydration λ. Right: channel width as a function of the water mass fraction $\%m$.

g_{BB}. We plot this function of figure 7.9. We can make a few comments on this figure. First, the position of peaks is not altered either by the doping nor by the water volume fraction. Second, the intensity of the peaks is always larger for stronger doping levels. This indicates a higher degree of spacial ordering, which is consistent with the hypothesis of surfactants favouring the formation of locally lamellar arrangements.

Figure 7.9: The pair correlation function of polymer backbone atoms, $gr_{BB}(r)$ computed for all available systems. The plot are grouped by water volume fraction c (low to high from top to bottom).

Chapter 8

Conclusion

In this thesis we have managed to provide, to the best of our knowledge, the first comprehensive picture of the dynamics of water molecules in soft confining environments, ranging from the case of extremely tight ch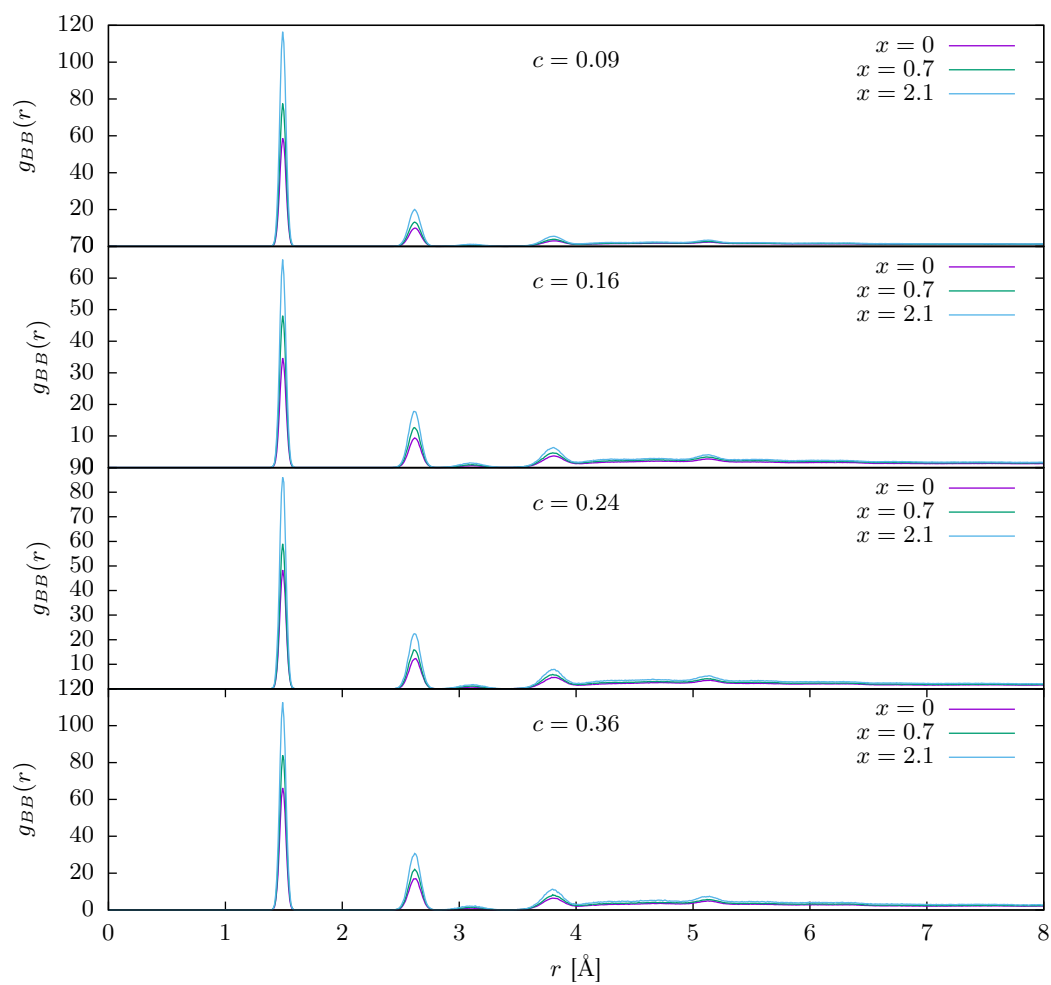annels, to that where the interface is in contact with an infinite reservoir of bulk water. These two limits cover, we believe, most part of the typical situations encountered in hydrated natural and synthesised materials.

We started from developing a model of ionic surfactants that allowed us to study the structure of neat model phases, and the dynamical behaviour of water and ions in these confining geometries. We then demonstrated how to extend this model to that of an ionic polymer and blends of polymers and surfactants. These systems can for instance be used to investigate the effect of tortuosity and charge density on the structure of the assemblies and on the transport properties of the absorbed water and ions. We considered ionic surfactants as model systems for their simplicity and potential for extension to more complex confining geometries. Because the interactions that we included in the simulation are generic, our description of the structure and transport properties, as well as the behaviour of water and ions at the interface can be transferred to other systems. Our model could, we believe, play for soft materials a critical paradigmatic role similar to that of carbon nanotubes for confinement in rigid ordered matrices.

Overall, we found that the interfaces are the key regions where both the structure and transport properties are determined. We demonstrated that to properly characterise the transport of water and ions in soft confining media, one has to include the possibility of sub-diffusive behaviour, especially when a significant fraction of the fluid is in the vicinity of the interface. We also found that this more careful analysis allows us to properly integrate our simulation results with experimental measurements, where probing different time- and length-scales leads to different values for the diffusion coefficients.

We also remark that to be able to perform simulations on the extended length- and time-scales presented in this work, we had to compromise on the level of detail included in the model. For example, our model cannot be used as is to study structural transport of protons. We are however convinced that this minimalist approach allowed us to describe in simpler terms, but still accurately, the essential physics of these systems. One may ask, what differences exist between our coarse grained model and an all-atoms description. Beyond the higher computational efficiency of the coarse grained model, our opinion is that in terms of the interactions, the effective potential as seen by a fluid molecule in the vicinity of an all-atoms surfactant assembly should be extremely similar to the one experienced by a water molecule near a coarse-grained matrix. As a matter of fact, we believe that further coarse-graining should not affect the main outcomes of our simulations.

Also, the length of the trajectories is limited by available computer time and storage capacity. While longer trajectories would of course be preferred, we chose to produce trajectories of reasonable length for multiple systems. This trade off allowed us to explore a wider region of the phase diagram, in great details. Note that only trajectories extending for at least one or two additional decades in time would be able to substantially improve our analysis, as most phenomena described in this thesis are extremely slow (for instance, correlation functions that decay as power laws).

Our initial idea was to investigate the dynamics of the fluid layer by layer. We expected to be able to extract transport properties as a function of the distance from the interface. However, we quickly realised that fluid particles traverse multiple layers during the simulation, and that while the residence time in the interfacial layer can be extremely long at low hydration, this is not the case in layers further from the interface or at high hydration. As a result, it is impossible to produce (for example) a layer-by-layer mean squared displacement that spans a long enough time scale to be exploitable. For this reason, we explored the possibility of separating average quantities like the self intermediate scattering function into multiple populations.

We also remark that while the dynamics of the different species are well separated in time, it would be interesting to investigate the case of a completely immobile (frozen) matrix to make direct contact with the case of solid boundaries.

Regarding the perspectives of this model, there are multiple gray areas that could be investigated. For instance, we have presented doping as a way to decrease the equivalent weight of the materials. Similar changes in the equivalent weight could also be obtained by shortening the length of the side chains or decreasing their spacing along the backbone. An issue would then be to determine the difference between doped materials and materials with modified topology, at the same equivalent weight. Our model could also be adapted to study other energy related materials: for instance, it is possible to replace the hydronium ions with lithium
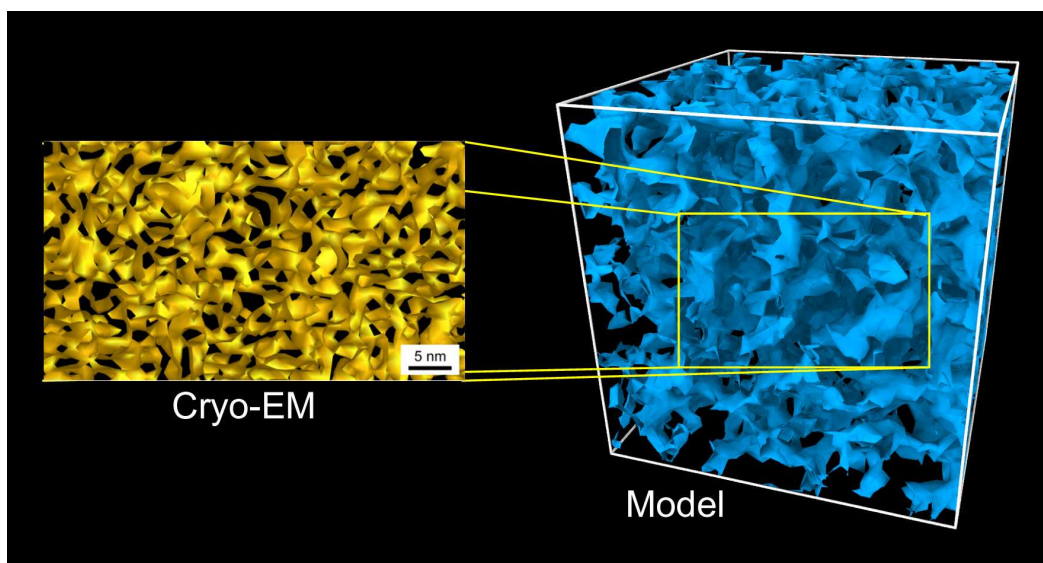
Figure 8.1: Future modelisation efforts should strive to integrate new experimental data sources. For instance, on the left we have the contour of the ionic domains from cryo-EM measurements [85], that could directly be compared to that generated from the simulation, and used to drive the simulation toward more realistic structures. (On the right, an example generated from on of our samples of hydrated polymer).

ions. In addition, tuning the properties of the backbone to match these of non-PFSA polymers (hydrocarbon or block polymers for instance) is also possible.

Moreover, we believe that future studies should focus on integrating the results of experiments to the simulation. Indeed, we feel that this approach would result in more realistic and efficient models than integrating, for instance, the quantum description of protons. For example, cryo-electron tomography recently became a viable technique to the determination of the nanostructure of hydrated ionomers in real space. Structural studies should focus on integrating the results of both traditional scattering techniques and novel approaches such as cryo-electron tomography into simulations. For instance, one could imagine a space-filling algorithm able to position water molecules, ions, and polymers to match the density field obtained by tomography. This should allow to optimise the model with respect to cryo-EM data (see figure 8.1) and the obtained configuration could then be used to study transport in extremely realistic morphologies.

Bibliography

[1] Jean-Philippe Bouchaud and Marc Potters. *Theory of financial risk and derivative pricing: from statistical physics to risk management.* Cambridge university press, 2003.

[2] Pierre-Gilles De Gennes. *Scaling concepts in polymer physics.* Cornell university press, 1979.

[3] Ralf Metzler and Joseph Klafter. The random walk's guide to anomalous diffusion: a fractional dynamics approach. *Physics reports*, 339(1):1–77, 2000.

[4] Ralf Metzler, Jae-Hyung Jeon, Andrey G Cherstvy, and Eli Barkai. Anomalous diffusion models and their properties: non-stationarity, non-ergodicity, and ageing at the centenary of single particle tracking. *Physical Chemistry Chemical Physics*, 16(44):24128–24164, 2014.

[5] Mike P Allen and Dominic J Tildesley. *Computer simulation of liquids.* Oxford university press, 1989.

[6] John F Brandts. The thermodynamics of protein denaturation. ii. a model of reversible denaturation and interpretations regarding the stability of chymotrypsinogen. *Journal of the American Chemical Society*, 86(20):4302–4314, 1964.

[7] Biman Bagchi. Water dynamics in the hydration layer around proteins and micelles. *Chemical Reviews*, 105(9):3197–3219, 2005.

[8] Eric Westhof. Water: an integral part of nucleic acid structure. *Annual review of biophysics and biophysical chemistry*, 17(1):125–144, 1988.

[9] Robert W Howarth, Anthony Ingraffea, and Terry Engelder. Natural gas: Should fracking stop? *Nature*, 477(7364):271–275, 2011.

[10] Charles L Ake, Kittane Mayura, Henry Huebner, Gerald R Bratton, and Timothy D Phillips. Development of porous clay-based composites for the

sorption of lead from water. *Journal of Toxicology and Environmental Health Part A*, 63(6):459–475, 2001.

[11] L Rubatat, G Gebel, and O Diat. Fibrillar structure of nafion: Matching fourier and real space studies of corresponding films and solutions. *Macromolecules*, 37(20):7772–7783, 2004.

[12] David S Eisenberg and Walter Kauzmann. *The structure and properties of water*, volume 123. Clarendon Press Oxford, 1969.

[13] Osamu Mishima and H Eugene Stanley. The relationship between liquid, supercooled and glassy water. *Nature*, 396(6709):329–335, 1998.

[14] E Sanz, C Vega, JLF Abascal, and LG MacDowell. Phase diagram of water from computer simulation. *Physical review letters*, 92(25):255701, 2004.

[15] John Russo, Flavio Romano, and Hajime Tanaka. New metastable form of ice and its role in the homogeneous crystallization of water. *Nature materials*, 13(7):733–739, 2014.

[16] Ralf Ludwig. Water: from clusters to the bulk. *Angewandte Chemie International Edition*, 40(10):1808–1827, 2001.

[17] Paulo A Netz, Francis W Starr, Marcia C Barbosa, and H Eugene Stanley. Relation between structural and dynamical anomalies in supercooled water. *Physica A: Statistical Mechanics and its Applications*, 314(1):470–476, 2002.

[18] Iwao Ohmine and Hideki Tanaka. Fluctuation, relaxations, and hydration in liquid water. hydrogen-bond rearrangement dynamics. *Chemical reviews*, 93(7):2545–2566, 1993.

[19] Alenka Luzar and David Chandler. Hydrogen-bond kinetics in liquid water. *Nature*, 379(6560):55–57, 1996.

[20] CJ Fecko, JD Eaves, JJ Loparo, A Tokmakoff, and PL Geissler. Ultrafast hydrogen-bond dynamics in the infrared spectroscopy of water. *Science*, 301(5640):1698–1702, 2003.

[21] GE Walrafen. Raman spectral studies of water structure. *The Journal of Chemical Physics*, 40(11):3249–3256, 1964.

[22] John C Dore and José Teixeira. *Hydrogen-bonded liquids*, volume 329. Springer Science & Business Media, 2012.

[23] John C Dore. Structural studies of water and other hydrogenbonded liquids by neutron diffraction. *Journal of molecular structure*, 250(2):193–211, 1991.

[24] R. Car and M. Parrinello. Unified approach for molecular dynamics and density-functional theory. *Phys. Rev. Lett.*, 55:2471–2474, Nov 1985.

[25] Hee-Seung Lee and Mark E Tuckerman. Structure of liquid water at ambient temperature from ab initio molecular dynamics performed in the complete basis set limit. *The Journal of chemical physics*, 125(15):154507, 2006.

[26] Francesco Paesani and Gregory A Voth. The properties of water: Insights from quantum simulations. *The Journal of Physical Chemistry B*, 113(17):5702–5719, 2009.

[27] Ph Wernet, D Nordlund, Uwe Bergmann, M Cavalleri, M Odelius, H Ogasawara, LÅ Näslund, TK Hirsch, Lars Ojamäe, P Glatzel, et al. The structure of the first coordination shell in liquid water. *Science*, 304(5673):995–999, 2004.

[28] William L Jorgensen, Jayaraman Chandrasekhar, Jeffry D Madura, Roger W Impey, and Michael L Klein. Comparison of simple potential functions for simulating liquid water. *The Journal of chemical physics*, 79(2):926–935, 1983.

[29] Christian D Berweger, Wilfred F van Gunsteren, and Florian Müller-Plathe. Force field parametrization by weak coupling. re-engineering spc water. *Chemical physics letters*, 232(5):429–436, 1995.

[30] HJC Berendsen, JR Grigera, and TP Straatsma. The missing term in effective pair potentials. *Journal of Physical Chemistry*, 91(24):6269–6271, 1987.

[31] Pekka Mark and Lennart Nilsson. Structure and dynamics of the tip3p, spc, and spc/e water models at 298 k. *The Journal of Physical Chemistry A*, 105(43):9954–9960, 2001.

[32] J Martı. Analysis of the hydrogen bonding and vibrational spectra of supercritical model water by molecular dynamics simulations. *The Journal of chemical physics*, 110(14):6876–6886, 1999.

[33] R Kumar, JR Schmidt, and JL Skinner. Hydrogen bonding definitions and dynamics in liquid water. *The Journal of chemical physics*, 126(20):204107, 2007.

[34] Alenka Luzar and David Chandler. Effect of environment on hydrogen bond dynamics in liquid water. *Physical review letters*, 76(6):928, 1996.

[35] HFMC Martiniano and N Galamba. Insights on hydrogen-bond lifetimes in liquid and supercooled water. *The Journal of Physical Chemistry B*, 117(50):16188–16195, 2013.

[36] J Teixeira and M-C Bellissent-Funel. Dynamics of water studied by neutron scattering. *Journal of Physics: Condensed Matter*, 2(S):SA105, 1990.

[37] Johan Qvist, Helmut Schober, and Bertil Halle. Structural dynamics of super-cooled water from quasielastic neutron scattering and molecular simulations. *The Journal of chemical physics*, 134(14):144508, 2011.

[38] Mark E Tuckerman, Dominik Marx, and Michele Parrinello. The nature and transport mechanism of hydrated hydroxide ions in aqueous solution. *Nature*, 417(6892):925–929, 2002.

[39] CJT De Grotthuss. *Mémoire sur la décomposition de l'eau: et des corps qu'elle tient en dissolution à l'aide de l'électricité galvanique.* 1805.

[40] Dominik Marx, Mark E Tuckerman, Jürg Hutter, and Michele Parrinello. The nature of the hydrated excess proton in water. *Nature*, 397(6720):601–604, 1999.

[41] Roger G Schmidt and Jürgen Brickmann. Molecular dynamics simulation of the proton transport in water. *Berichte der Bunsengesellschaft für physikalische Chemie*, 101(12):1816–1827, 1997.

[42] Shina CL Kamerlin and Arieh Warshel. The empirical valence bond model: theory and applications. *Wiley Interdisciplinary Reviews: Computational Molecular Science*, 1(1):30–45, 2011.

[43] Udo W Schmitt and Gregory A Voth. Quantum properties of the excess proton in liquid water. *Israel Journal of Chemistry*, 39(3-4):483–492, 1999.

[44] Ka Lum, David Chandler, and John D Weeks. Hydrophobicity at small and large length scales. *The Journal of Physical Chemistry B*, 103(22):4570–4577, 1999.

[45] David Chandler. Interfaces and the driving force of hydrophobic assembly. *Nature*, 437(7059):640–647, 2005.

[46] Bert L de Groot and Helmut Grubmüller. Water permeation across biological membranes: mechanism and dynamics of aquaporin-1 and glpf. *Science*, 294(5550):2353–2357, 2001.

[47] Bharat Baruah, Jennifer M Roden, Myles Sedgwick, N Mariano Correa, Debbie C Crans, and Nancy E Levinger. When is water not water? exploring water confined in large reverse micelles using a highly charged inorganic molecular probe. *Journal of the American Chemical Society*, 128(39):12758–12765, 2006.

[48] Gerhard Hummer, Jayendran C Rasaiah, and Jerzy P Noworyta. Water conduction through the hydrophobic channel of a carbon nanotube. *Nature*, 414(6860):188–190, 2001.

[49] Jeffrey K Clark II and Stephen J Paddison. Ab initio molecular dynamics simulations of water and an excess proton in water confined in carbon nanotubes. *Physical Chemistry Chemical Physics*, 16(33):17756–17769, 2014.

[50] Bradley F Habenicht, Stephen J Paddison, and Mark E Tuckerman. The effects of the hydrophobic environment on proton mobility in perfluorosulfonic acid systems: an ab initio molecular dynamics study. *Journal of Materials Chemistry*, 20(30):6342–6351, 2010.

[51] MC Gordillo and J Martı. Hydrogen bond structure of liquid water confined in nanotubes. *Chemical Physics Letters*, 329(5):341–345, 2000.

[52] Alexander I Kolesnikov, Jean-Marc Zanotti, Chun-Keung Loong, Pappannan Thiyagarajan, Alexander P Moravsky, Raouf O Loutfy, and Christian J Burnham. Anomalously soft dynamics of water in a nanotube: a revelation of nanoscale confinement. *Physical review letters*, 93(3):035503, 2004.

[53] Yingchun Liu, Qi Wang, Tao Wu, and Li Zhang. Fluid structure and transport properties of water inside carbon nanotubes. *The Journal of chemical physics*, 123(23):234701, 2005.

[54] Amrit Kalra, Shekhar Garde, and Gerhard Hummer. Osmotic water transport through carbon nanotube membranes. *Proceedings of the National Academy of Sciences*, 100(18):10175–10180, 2003.

[55] Mainak Majumder, Nitin Chopra, Rodney Andrews, and Bruce J Hinds. Nanoscale hydrodynamics: enhanced flow in carbon nanotubes. *Nature*, 438(7064):44–44, 2005.

[56] Sony Joseph and NR Aluru. Why are carbon nanotubes fast transporters of water? *Nano letters*, 8(2):452–458, 2008.

[57] Christoph Dellago, Mor M Naor, and Gerhard Hummer. Proton transport through water-filled carbon nanotubes. *Physical review letters*, 90(10):105902, 2003.

[58] Zhen Cao, Yuxing Peng, Tianying Yan, Shu Li, Ailin Li, and Gregory A Voth. Mechanism of fast proton transport along one-dimensional water chains confined in carbon nanotubes. *Journal of the American Chemical Society*, 132(33):11395–11397, 2010.

[59] Nicolas Giovambattista, Peter J Rossky, and Pablo G Debenedetti. Phase transitions induced by nanoconfinement in liquid water. *Physical review letters*, 102(5):050603, 2009.

[60] MA Ricci, F Bruni, P Gallo, M Rovere, and AK Soper. Water in confined geometries: experiments and simulations. *Journal of Physics: Condensed Matter*, 12(8A):A345, 2000.

[61] M Rovere and P Gallo. Effects of confinement on static and dynamical properties of water. *The European Physical Journal E: Soft Matter and Biological Physics*, 12(1):77–81, 2003.

[62] Guillaume Stirnemann, Fabio Sterpone, and Damien Laage. Dynamics of water in concentrated solutions of amphiphiles: key roles of local structure and aggregation. *The Journal of Physical Chemistry B*, 115(12):3254–3262, 2011.

[63] P-O Westlund. Line shape analysis of nmr powder spectra of 2h2o in lipid bilayer systems. *The Journal of Physical Chemistry B*, 104(25):6059–6064, 2000.

[64] Eiji Yamamoto, Takuma Akimoto, Yoshinori Hirano, Masato Yasui, and Kenji Yasuoka. Power-law trapping of water molecules on the lipid-membrane surface induces water retardation. *Physical Review E*, 87(5):052715, 2013.

[65] Eiji Yamamoto, Takuma Akimoto, Masato Yasui, and Kenji Yasuoka. Origin of subdiffusion of water molecules on cell membrane surfaces. *Scientific reports*, 4, 2014.

[66] Caterina Arcangeli, Anna Rita Bizzarri, and Salvatore Cannistraro. Role of interfacial water in the molecular dynamics-simulated dynamical transition of plastocyanin. *Chemical physics letters*, 291(1):7–14, 1998.

[67] Claudia Rocchi, Anna Rita Bizzarri, and Salvatore Cannistraro. Water dynamical anomalies evidenced by molecular-dynamics simulations at the solvent-protein interface. *Physical Review E*, 57(3):3315, 1998.

[68] Anna Rita Bizzarri, Alessandro Paciaroni, and Salvatore Cannistraro. Glasslike dynamical behavior of the plastocyanin hydration water. *Physical Review E*, 62(3):3991, 2000.

[69] Anna Rita Bizzarri and Salvatore Cannistraro. Molecular dynamics of water at the protein-solvent interface. *The Journal of Physical Chemistry B*, 106(26):6617–6633, 2002.

[70] Francesco Pizzitutti, Massimo Marchi, Fabio Sterpone, and Peter J Rossky. How protein surfaces induce anomalous dynamics of hydration water. *The Journal of Physical Chemistry B*, 111(26):7584–7590, 2007.

[71] Carlo Manzo, Juan A Torreno-Pina, Pietro Massignan, Gerald J Lapeyre Jr, Maciej Lewenstein, and Maria F Garcia Parajo. Weak ergodicity breaking of receptor motion in living cells stemming from random diffusivity. *Physical Review X*, 5(1):011021, 2015.

[72] Takuma Akimoto, Eiji Yamamoto, Kenji Yasuoka, Yoshinori Hirano, and Masato Yasui. Non-gaussian fluctuations resulting from power-law trapping in a lipid bilayer. *Physical review letters*, 107(17):178103, 2011.

[73] Longhe Zhang, Nicole R Brostowitz, Kevin A Cavicchi, and RA Weiss. Perspective: ionomer research and applications. *Macromolecular Reaction Engineering*, 8(2):81–99, 2014.

[74] TD Gierke, GE Munn, and FCd Wilson. The morphology in nafion perfluorinated membrane products, as determined by wide-and small-angle x-ray studies. *Journal of Polymer Science: Polymer Physics Edition*, 19(11):1687–1704, 1981.

[75] PJ James, JA Elliott, TJ McMaster, JM Newton, AMS Elliott, S Hanna, and MJ Miles. Hydration of nafion® studied by afm and x-ray scattering. *Journal of materials science*, 35(20):5111–5119, 2000.

[76] Laurent Rubatat, Anne Laure Rollet, Gérard Gebel, and Olivier Diat. Evidence of elongated polymeric aggregates in nafion. *Macromolecules*, 35(10):4050–4055, 2002.

[77] Scott A Eastman, Sangcheol Kim, Kirt A Page, Brandon W Rowe, Shuhui Kang, Christopher L Soles, and Kevin G Yager. Effect of confinement on structure, water solubility, and water transport in nafion thin films. *Macromolecules*, 45(19):7920–7930, 2012.

[78] Anne-Laure Rollet, Gérard Gebel, Jean-Pierre Simonin, and Pierre Turq. A sans determination of the influence of external conditions on the nanostructure of nafion membrane. *Journal of Polymer Science Part B: Polymer Physics*, 39(5):548–558, 2001.

[79] Anne-Laure Rollet, Olivier Diat, and Gerard Gebel. A new insight into nafion structure. *The Journal of Physical Chemistry B*, 106(12):3033–3036, 2002.

[80] Joseph A Dura, Vivek S Murthi, Michael Hartman, Sushil K Satija, and Charles F Majkrzak. Multilamellar interface structures in nafion. *Macromolecules*, 42(13):4769–4774, 2009.

[81] Klaus Schmidt-Rohr and Qiang Chen. Parallel cylindrical water nanochannels in nafion fuel-cell membranes. *Nature materials*, 7(1):75–83, 2008.

[82] G Gebel and O Diat. Neutron and x-ray scattering: Suitable tools for studying ionomer membranes. *Fuel Cells*, 5(2):261–276, 2005.

[83] James A Elliott and Stephen J Paddison. Modelling of morphology and proton transport in pfsa membranes. *Physical chemistry chemical physics*, 9(21):2602–2618, 2007.

[84] Klaus-Dieter Kreuer and Giuseppe Portale. A critical revision of the nano-morphology of proton conducting ionomers and polyelectrolytes for fuel cell applications. *Advanced Functional Materials*, 23(43):5390–5397, 2013.

[85] Frances I Allen, Luis R Comolli, Ahmet Kusoglu, Miguel A Modestino, Andrew M Minor, and Adam Z Weber. Morphology of hydrated as-cast nafion revealed through cryo electron tomography. *ACS Macro Letters*, 4(1):1–5, 2014.

[86] Stephen J Paddison and James A Elliott. On the consequences of side chain flexibility and backbone conformation on hydration and proton dissociation in perfluorosulfonic acid membranes. *Physical Chemistry Chemical Physics*, 8(18):2193–2203, 2006.

[87] Arun Venkatnathan, Ram Devanathan, and Michel Dupuis. Atomistic simulations of hydrated nafion and temperature effects on hydronium ion mobility. *The Journal of Physical Chemistry B*, 111(25):7234–7244, 2007.

[88] James A Elliott, Dongsheng Wu, Stephen J Paddison, and Robert B Moore. A unified morphological description of nafion membranes from saxs and mesoscale simulations. *Soft Matter*, 7(15):6820–6827, 2011.

[89] Stephen J Paddison and Thomas A Zawodzinski Jr. Molecular modeling of the pendant chain in nafion®. *Solid State Ionics*, 113:333–340, 1998.

[90] SJ Paddison. The modeling of molecular structure and ion transport in sulfonic acid based ionomer membranes. *Journal of New Materials for Electrochemical Systems*, 4(4):197–208, 2001.

116

[91] Stephen J Paddison and James A Elliott. Molecular modeling of the short-side-chain perfluorosulfonic acid membrane. *The Journal of Physical Chemistry A*, 109(33):7583–7593, 2005.

[92] Iordan H Hristov, Stephen J Paddison, and Reginald Paul. Molecular modeling of proton transport in the short-side-chain perfluorosulfonic acid ionomer. *The Journal of Physical Chemistry B*, 112(10):2937–2949, 2008.

[93] Shingo Urata, Jun Irisawa, Akira Takada, Wataru Shinoda, Seiji Tsuzuki, and Masuhiro Mikami. Molecular dynamics simulation of swollen membrane of perfluorinated ionomer. *The Journal of Physical Chemistry B*, 109(9):4269–4278, 2005.

[94] Ram Devanathan, Arun Venkatnathan, and Michel Dupuis. Atomistic simulation of nafion membrane: I. effect of hydration on membrane nanostructure. *The Journal of Physical Chemistry B*, 111(28):8069–8079, 2007.

[95] Pavel V Komarov, Pavel G Khalatur, and Alexei R Khokhlov. Large-scale atomistic and quantum-mechanical simulations of a nafion membrane: Morphology, proton solvation and charge transport. *Beilstein journal of nanotechnology*, 4(1):567–587, 2013.

[96] James T Wescott, Yue Qi, Lalitha Subramanian, and T Weston Capehart. Mesoscale simulation of morphology in hydrated perfluorosulfonic acid membranes. *The Journal of chemical physics*, 124(13):134702, 2006.

[97] James A Elliott, Alice M S Elliott, Graham E Cooley, et al. Atomistic simulation and molecular dynamics of model systems for perfluorinated ionomer membranes. *Physical Chemistry Chemical Physics*, 1(20):4855–4863, 1999.

[98] Aleksey Vishnyakov and Alexander V Neimark. Molecular dynamics simulation of microstructure and molecular mobilities in swollen nafion membranes. *The Journal of Physical Chemistry B*, 105(39):9586–9594, 2001.

[99] Seung Soon Jang, Valeria Molinero, Tahir Çağın, and William A Goddard III. Effect of monomeric sequence on nanophase-segregated structure and water transport in nafion 117. *Prepr. Pap.-Am. Chem. Soc., Div. Fuel Chem*, 48(2):510, 2003.

[100] PV Komarov, IN Veselov, PP Chu, PG Khalatur, and AR Khokhlov. Atomistic and mesoscale simulation of polymer electrolyte membranes based on sulfonated poly (ether ether ketone). *Chemical Physics Letters*, 487(4):291–296, 2010.

[101] Anurag Prakash Sunda and Arun Venkatnathan. Molecular dynamics simulations of side chain pendants of perfluorosulfonic acid polymer electrolyte membranes. *Journal of Materials Chemistry A*, 1(3):557–569, 2013.

[102] Elshad Allahyarov and Philip L Taylor. Role of electrostatic forces in cluster formation in a dry ionomer. *The Journal of chemical physics*, 127(15):154901, 2007.

[103] Elshad Allahyarov and Philip L Taylor. Simulation study of the correlation between structure and conductivity in stretched nafion. *The Journal of Physical Chemistry B*, 113(3):610–617, 2008.

[104] Elshad Allahyarov, Philip L Taylor, and Hartmut Löwen. Simulation study of field-induced morphological changes in a proton-conducting ionomer. *Physical Review E*, 81(3):031805, 2010.

[105] Elshad Allahyarov, Philip L Taylor, and Hartmut Löwen. A simulation study of field-induced proton-conduction pathways in dry ionomers. *Journal of Physics: Condensed Matter*, 23(23):234105, 2011.

[106] Thomas A Zawodzinski Jr, Michal Neeman, Laurel O Sillerud, and Shimshon Gottesfeld. Determination of water diffusion coefficients in perfluorosulfonate ionomeric membranes. *The Journal of Physical Chemistry*, 95(15):6040–6044, 1991.

[107] Ferdinand Volino, Jean-Christophe Perrin, and Sandrine Lyonnard. Gaussian model for localized translational motion: application to incoherent neutron scattering. *The Journal of Physical Chemistry B*, 110(23):11217–11223, 2006.

[108] Jean-Christophe Perrin, Sandrine Lyonnard, Armel Guillermo, and Pierre Levitz. Water dynamics in ionomer membranes by field-cycling nmr relaxometry. *The Journal of Physical Chemistry B*, 110(11):5439–5444, 2006.

[109] Jean-Christophe Perrin, Sandrine Lyonnard, and Ferdinand Volino. Quasielastic neutron scattering study of water dynamics in hydrated nafion membranes. *The Journal of Physical Chemistry C*, 111(8):3393–3404, 2007.

[110] Quentin Berrod. *Relation structure-transport dans des membranes et matériaux modèles pour pile à combustible.* PhD thesis, Université de Grenoble, 2013.

[111] Michael Eikerling, Stephen J Paddison, Lawrence R Pratt, and Thomas A Zawodzinski. Defect structure for proton transport in a triflic acid monohydrate solid. *Chemical Physics Letters*, 368(1):108–114, 2003.

[112] Robin L Hayes, Stephen J Paddison, and Mark E Tuckerman. Proton transport in triflic acid hydrates studied via path integral car- parrinello molecular dynamics. *The Journal of Physical Chemistry B*, 113(52):16574–16589, 2009.

[113] Robin L Hayes, Stephen J Paddison, and Mark E Tuckerman. Proton transport in triflic acid pentahydrate studied via ab initio path integral molecular dynamics. *The Journal of Physical Chemistry A*, 115(23):6112–6124, 2011.

[114] Matt K Petersen and Gregory A Voth. Characterization of the solvation and transport of the hydrated proton in the perfluorosulfonic acid membrane nafion. *The Journal of Physical Chemistry B*, 110(37):18594–18600, 2006.

[115] Supaporn Dokmaisrijan and Eckhard Spohr. Md simulations of proton transport along a model nafion surface decorated with sulfonate groups. *Journal of molecular liquids*, 129(1):92–100, 2006.

[116] E Spohr, P Commer, and AA Kornyshev. Enhancing proton mobility in polymer electrolyte membranes: lessons from molecular dynamics simulations. *The Journal of Physical Chemistry B*, 106(41):10560–10569, 2002.

[117] Shengting Cui, Junwu Liu, Myvizhi Esai Selvan, David J Keffer, Brian J Edwards, and William V Steele. A molecular dynamics study of a nafion polyelectrolyte membrane and the aqueous phase structure for proton transport. *The Journal of Physical Chemistry B*, 111(9):2208–2218, 2007.

[118] Ram Devanathan, Arun Venkatnathan, and Michel Dupuis. Atomistic simulation of nafion membrane. 2. dynamics of water molecules and hydronium ions. *The Journal of Physical Chemistry B*, 111(45):13006–13013, 2007.

[119] Quentin Berrod, Sandrine Lyonnard, Armel Guillermo, Jacques Ollivier, Bernhard Frick, and Gérard Gébel. Qens investigation of proton confined motions in hydrated perfluorinated sulfonic membranes and self-assembled surfactants. In *EPJ Web of Conferences*, volume 83, page 02002. EDP Sciences, 2015.

[120] S Lyonnard, Q Berrod, B-A Brüning, G Gebel, A Guillermo, H Ftouni, J Ollivier, and B Frick. Perfluorinated surfactants as model charged systems for understanding the effect of confinement on proton transport and water mobility in fuel cell membranes. a study by qens. *The European Physical Journal Special Topics*, 189(1):205–216, 2010.

[121] Simona Dalla Bernardina, Jean-Blaise Brubach, Quentin Berrod, Armel Guillermo, Patrick Judeinstein, Pascale Roy, and Sandrine Lyonnard. Mechanism of ionization, hydration, and intermolecular h-bonding in proton con-

ducting nanostructured ionomers. *The Journal of Physical Chemistry C*, 118(44):25468–25479, 2014.

[122] RG Larson. Self-assembly of surfactant liquid crystalline phases by monte carlo simulation. *The Journal of chemical physics*, 91(4):2479–2488, 1989.

[123] Wataru Shinoda, Russell DeVane, and Michael L Klein. Coarse-grained force field for ionic surfactants. *Soft Matter*, 7(13):6178–6186, 2011.

[124] Shigeyuki Komura and Hiroya Kodama. Two-order-parameter model for an oil-water-surfactant system. *Physical Review E*, 55(2):1722, 1997.

[125] RG Larson. Monte carlo lattice simulation of amphiphilic systems in two and three dimensions. *The Journal of chemical physics*, 89(3):1642–1650, 1988.

[126] Aniket Bhattacharya and SD Mahanti. Self-assembly of ionic surfactants and formation of mesostructures. *Journal of Physics: Condensed Matter*, 13(7):1413, 2001.

[127] B Smit, PAJ Hilbers, and K Esselink. Computer simulations of surfactant self assembly. *International Journal of Modern Physics C*, 4(02):393–400, 1993.

[128] friedrich K Von Gottberg, Kenneth A Smith, and T Alan Hatton. Stochastic dynamics simulation of surfactant self-assembly. *The Journal of chemical physics*, 106(23):9850–9857, 1997.

[129] Wataru Shinoda, Russell DeVane, and Michael L Klein. Coarse-grained molecular modeling of non-ionic surfactant self-assembly. *Soft Matter*, 4(12):2454–2462, 2008.

[130] Miguel Jorge. Molecular dynamics simulation of self-assembly of n-decyltrimethylammonium bromide micelles. *Langmuir*, 24(11):5714–5725, 2008.

[131] J Rodriguez, D Laria, E Guardia, and J Marti. Dynamics of water nanodroplets and aqueous protons in non-ionic reverse micelles. *Physical Chemistry Chemical Physics*, 11(10):1484–1490, 2009.

[132] Jingfei Chen and Jingcheng Hao. Molecular dynamics simulation of cetyltrimethylammonium bromide and sodium octyl sulfate mixtures: aggregate shape and local surfactant distribution. *Physical Chemistry Chemical Physics*, 15(15):5563–5571, 2013.

[133] Howe-Siang Tan, Ivan R Piletic, and MD Fayer. Orientational dynamics of water confined on a nanometer length scale in reverse micelles. *The Journal of chemical physics*, 122(17):174501, 2005.

120

[134] G Gompper and Stefan Klein. Ginzburg-landau theory of aqueous surfactant solutions. *Journal de Physique II*, 2(9):1725–1744, 1992.

[135] Maxim Belushkin and Gerhard Gompper. Twist grain boundaries in cubic surfactant phases. *The Journal of chemical physics*, 130(13):134712, 2009.

[136] O Theissen, G Gompper, and DM Kroll. Lattice-boltzmann model of amphiphilic systems. *EPL (Europhysics Letters)*, 42(4):419, 1998.

[137] Thomas Ihle and Daniel M Kroll. Stochastic rotation dynamics. i. formalism, galilean invariance, and green-kubo relations. *Physical Review E*, 67(6):066705, 2003.

[138] Robert D Groot. Electrostatic interactions in dissipative particle dynamicssimulation of polyelectrolytes and anionic surfactants. *The Journal of chemical physics*, 118(24):11265–11277, 2003.

[139] Live Rekvig, Marieke Kranenburg, Jocelyne Vreede, Bjørn Hafskjold, and Berend Smit. Investigation of surfactant efficiency using dissipative particle dynamics. *Langmuir*, 19(20):8195–8205, 2003.

[140] Simon Jury, Peter Bladon, Mike Cates, Sujata Krishna, Maarten Hagen, Noel Ruddock, and Patrick Warren. Simulation of amphiphilic mesophases using dissipative particle dynamics. *Phys. Chem. Chem. Phys.*, 1(9):2051–2056, 1999.

[141] Jean-Paul Ryckaert, Giovanni Ciccotti, and Herman JC Berendsen. Numerical integration of the cartesian equations of motion of a system with constraints: molecular dynamics of n-alkanes. *Journal of Computational Physics*, 23(3):327–341, 1977.

[142] Dirk Zahn, Bernd Schilling, and Stefan M Kast. Enhancement of the wolf damped coulomb potential: Static, dynamic, and dielectric properties of liquid water from molecular simulation. *The Journal of Physical Chemistry B*, 106(41):10725–10732, 2002.

[143] Tom Darden, Darrin York, and Lee Pedersen. Particle mesh ewald: An n log (n) method for ewald sums in large systems. *The Journal of chemical physics*, 98(12):10089–10092, 1993.

[144] D Wolf, P Keblinski, SR Phillpot, and J Eggebrecht. Exact method for the simulation of coulombic systems by spherically truncated, pairwise r- 1 summation. *The Journal of chemical physics*, 110(17):8254–8282, 1999.

[145] Christopher J Fennell and J Daniel Gezelter. Is the ewald summation still necessary? pairwise alternatives to the accepted standard for long-range electrostatics. *The Journal of chemical physics*, 124(23):234104, 2006.

[146] Jesper S Hansen, Thomas B Schrøder, and Jeppe C Dyre. Simplistic coulomb forces in molecular dynamics: Comparing the wolf and shifted-force approximations. *The Journal of Physical Chemistry B*, 116(19):5738–5743, 2012.

[147] Jocelyn M Rodgers and John D Weeks. Interplay of local hydrogen-bonding and long-ranged dipolar forces in simulations of confined water. *Proceedings of the National Academy of Sciences*, 105(49):19136–19141, 2008.

[148] P Gallo, M Rovere, and E Spohr. Supercooled confined water and the mode coupling crossover temperature. *Physical review letters*, 85(20):4317, 2000.

[149] Steve Plimpton, Paul Crozier, and Aidan Thompson. Lammps-large-scale atomic/molecular massively parallel simulator. *Sandia National Laboratories*, 18, 2007.

[150] Francis W Starr, Marie-Claire Bellissent-Funel, and H Eugene Stanley. Structure of supercooled and glassy water under pressure. *Physical Review E*, 60(1):1084, 1999.

[151] P Gallo, M Rovere, MA Ricci, C Hartnig, and E Spohr. Evidence of glassy behaviour of water molecules in confined states. *Philosophical Magazine B*, 79(11-12):1923–1930, 1999.

[152] P Gallo, M Rovere, and E Spohr. Glass transition and layering effects in confined water: a computer simulation study. *The Journal of Chemical Physics*, 113(24):11324–11335, 2000.

[153] P Gallo, M Rovere, MA Ricci, C Hartnig, and E Spohr. Non-exponential kinetic behaviour of confined water. *EPL (Europhysics Letters)*, 49(2):183, 2000.

[154] R Jay Mashl, Sony Joseph, NR Aluru, and Eric Jakobsson. Anomalously immobilized water: a new water phase induced by confinement in nanotubes. *Nano Letters*, 3(5):589–592, 2003.

[155] I Kusaka, Z-G Wang, and JH Seinfeld. Binary nucleation of sulfuric acid-water: Monte carlo simulation. *The Journal of chemical physics*, 108(16):6829–6848, 1998.

[156] Samuel Hanot, Sandrine Lyonnard, and Stefano Mossa. Water confined in self-assembled ionic surfactant nano-structures. *Soft matter*, 11(12):2469–2478, 2015.

[157] Seung Soon Jang, Valeria Molinero, Tahir Cagin, and William A Goddard. Nanophase-segregation and transport in nafion 117 from molecular dynamics simulations: effect of monomeric sequence. *The Journal of Physical Chemistry B*, 108(10):3149–3157, 2004.

[158] Mike P Allen, Dominic J Tildesley, et al. Computer simulation of liquids. 1987.

[159] Stephen C Harvey, Robert K-Z Tan, and Thomas E Cheatham. The flying ice cube: velocity rescaling in molecular dynamics leads to violation of energy equipartition. *Journal of Computational Chemistry*, 19(7):726–740, 1998.

[160] Robert G Laughlin. *The aqueous phase behavior of surfactants*, volume 6. Academic Press London, 1994.

[161] Erik Kissa. *Fluorinated surfactants and repellents*, volume 97. CRC Press, 2001.

[162] Rakhi Sood, Cristina Iojoiu, Eliane Espuche, Fabrice Gouanve, Gerard Gebel, Hakima Mendil-Jakani, Sandrine Lyonnard, and Jacques Jestin. Proton conducting ionic liquid doped nafion membranes: nano-structuration, transport properties and water sorption. *The Journal of Physical Chemistry C*, 116(46):24413–24423, 2012.

[163] Fei Lu, Xinpei Gao, Shuting Xie, Nan Sun, and Liqiang Zheng. Chemical modification of nafion membranes by protic ionic liquids: the key role of ionomer–cation interactions. *Soft matter*, 10(39):7819–7825, 2014.

[164] Adam P. Willard and David Chandler. The molecular structure of the interface between water and a hydrophobic substrate is liquid-vapor like. *arXiv:1407.4365 [cond-mat.soft]*, 2014.

[165] David Chandler and Patrick Varilly. Lectures on molecular-and nano-scale fluctuations in water. *arXiv preprint arXiv:1101.2235*, 2011.

[166] Kärger Hahn, J Kärger, and V Kukla. Single-file diffusion observation. *Physical review letters*, 76(15):2762, 1996.

[167] Quentin Berrod, Sandrine Lyonnard, Armel Guillermo, Jacques Ollivier, Bernhard Frick, Abdelatif Manseri, Bruno Améduri, and Gérard Gébel. Nanostructure and transport properties of proton conducting self-assembled

perfluorinated surfactants: a bottom-up approach towards pfsa fuel cell membranes. *Macromolecules*, in press.

[168] Jinsuk Song, Oc Hee Han, and Songi Han. Nanometer-scale water-and proton-diffusion heterogeneities across water channels in polymer electrolyte membranes. *Angewandte Chemie International Edition*, 54(12):3615–3620, 2015.

[169] Daniel T Hallinan Jr, Maria Grazia De Angelis, Marco Giacinti Baschetti, Giulio C Sarti, and Yossef A Elabd. Non-fickian diffusion of water in nafion. *Macromolecules*, 43(10):4667–4678, 2010.

[170] Alexander Stukowski. Visualization and analysis of atomistic simulation data with ovito–the open visualization tool. *Modelling and Simulation in Materials Science and Engineering*, 18(1):015012, 2010.

L'eau est partout et joue un rôle déterminant dans une multitude de processus. Cependant, on la trouve souvent au sein de minuscules cellules, pores, ou canaux. En de tels cas, les proprietés "macroscopiques" de l'eau sont modifiées par les restrictions spatiales et les interactions entre les molcules d'eau et le matériau confinant. Elucider les propriétés de l'eau en confinement est crucial, et une comprhension générale peut seulement être obtenue à travers l'utilisation de modèles. Alors que l'eau confinée dans des matériaux durs tels que les nanotubes de carbone est bien documentée, nous n'avons pas trouvé de modèle général pour l'étude de l'eau confinée a des matériaux mous, et ce en dépit de décénies de recherches sur de nombreux modèles spécifiques à une biomolécule ou un polymère en particulier. Dans cette thèse, nous présentons un modèle numérique d'eau confinée dans des géométries molles, générées par auto-assemblage. Nous comprenons la manière dont les interactions réciproques entre l'eau et la matrice confinante déterminent la structure des assemblages et les propriétés de transport de l'eau. Nous avons choisi un modèle de surfactant ioniques, matériaux très versatiles qui sont capables de s'auto-assembler en diverses géométries confinantes.

Nous nous concentrons sur l'effet des interfaces sur la formation de la nanostructure et sur les propriétés de transport à l'échelle de la nanoseconde. Nous nous distan cons de l'approche traditionnelle au problème du transport de l'eau dans des nanomatériaux. Nous montrons que l'hypothèse habituelle du transport diffusif est invalide car la matrice confinante piège les molécules d'eau à l'interface. Nous proposons de remplacer cette hypothèse par celle du transport sous-diffusif, et nous mettons en évidence le rôle de l'échelle de taille et des propriétés topologiques du confinement. Nous montrons que cette approche explique des résultats expérimentaux pour léau confinée dans des matériaux de synthèse, et qu'elle est compatible avec les développements récents liés à l'eau biologique.

Water is omnipresent and plays a decisive role in a myriad of processes. However, it is often found hidden in tiny cells, pores, or channels. In such cases, the usual "bulk" features of water are modified by the limited available space and the interactions of individual molecules with the confining material. Elucidating the properties of water in such confined states is critical and general understanding can only be achieved through models. While water confined in model hard materials such as carbon nanotubes is well documented, we found that there exist no general model to study water confined in soft materials, although this has been an active research topic for decades and despite the numerous models specific to one biomolecule or polymer that have been developed. In this thesis, we present a numerical model of water confined in soft self-assembled environments, and we provide an understanding of how the interplay between water and the confining matrix affects the structure of the assemblies and transport properties of water. Our model confining matrix is composed of ionic surfactants. This versatile model is able to self-assemble to a wide variety of confining geometries.

We focus on the role of interfaces in shaping the nanometer scale structure, and nanosecond scale transport properties. This work is a departure from the traditional approach to the problem of transport of water confined in soft nanomaterials. We show that the usual hypothesis of diffusive water transport does not hold due to trapping of molecules at the interface with the confining matrix. Instead, we support a picture where transport is sub-diffusive, and we highlight the role of the length-scale of the confinement and of its topological features. We find that this rationale explains experimental results for water confined in synthetic materials, and that it is compatible with recent advances in the understanding of biological water.